INFN LABORATORI NAZIONALI DI FRASCATI
SIS – Pubblicazioni

LNF-06/32 (Thesis)
December 12, 2006

Università degli Studi di Roma
Tor Vergata
Facoltà di Ingegneria

Corso di Laurea in Modelli e Sistemi

Tesi di Laurea

SIMULATION OF THE THERMO–OPTICAL PROPERTIES OF THE LARES AND LAGEOS SATELLITES FOR A PRECISE MEASUREMENT OF THE LENSE–THIRRING EFFECT IN GENERAL RELATIVITY

Studente:
Arianna Bosco
Università di Tor Vergata

Relatore:
Prof. Giovanni Bellettini
Università di Tor Vergata

Co–Relatore:
Ing. Giovanni Delle Monache
Laboratori Nazionali di Frascati dell’INFN

Anno Accademico 2004¬2005

Zwei Dinge sind unendlich:
Das Universum und die menschliche Dummheit.
Aber bei dem Universum bin ich mir noch nicht ganz sicher.

(Due cose sono infinite: l'universo e la stupidità umana.
Ma sull' universo non sono poi così sicuro).

A.Einstein

Contents

Chapter 1

Introduction

Motivation for this work and original contribution

This thesis is an experimental work on the thermo-optical characterization of a prototype of the LARES Earth satellite, designed for a precision test of General Relativity (GR, 1916): the measurement of the Lense-Thirring effect (1918) or "frame dragging", as Einstein used to call it. This is the precession of the satellite orbit due to the rotation of the central attracting body, Earth, which drags the space-time around with it. This effect is different from GR phenomena like the precession of Mercury's orbit around the Sun or the deflection of the path of photons passing nearby the Sun, which are due to the presence of a large static mass, which curves the space-time. On the contrary, the Earth angular momentum generates additional space-time curvature and "drags" around nearby gyroscopes (spins) and satellite orbits (orbital angular momenta). If the angular momentum of Earth (J_{Earth}) would be zero, than no frame dragging would be observed. The Lense-Thirring rate for the node orbital element, Ω, is:

$$\dot{\Omega} = \frac{2\, G\, J_{Earth}}{c^2\, a^3\, (1\, -\, e^2)^{3/2}}, \tag{1.1}$$

(where G is the gravitational constant, a and e are the orbit semi-major axis and eccentricity; the node is the intersection of the Earth's equatorial plane with the satellite's orbit).

The amount of this precession is tiny: ~ 2 meters per year (33 milliarcsec/year) for the semi-major axis of 12000 Km of the LAGEOS satellites. This value is more than a factor of ten smaller than the precession of Mercury's perihelion, which is 430 milliarcsec/year. The Lense-Thirring effect is formally (i.e. mathematically) similar to the precession induced by a central sphere of rotating electric charge on a discrete dipole moment or on the dipole moment of a closed electric current loop. For this reason, it is also referred to as "gravitomagnetism".

The candidate started her work right at the beginning of the Research and Development (R&D) performed by the LARES group of the Laboratori Nazionali di Frascati dell'INFN (INFN-LNF). LARES is a modern, second generation satellite, which was proposed to INFN by an international Collaboration at the end of 2004 and is expected to be launched in early 2008. This R&D program includes:

(i) the full plan of tests, the study of an improved satellite design and of two different launch options;

(ii) the design of the basic "3×3" prototype and the complete simulation of its thermo-optical properties using a specialized software of aerospace engineering, deployed by several space agencies and aerospace engineering companies;

(iii) the construction of the "3×3" prototype and its mechanical assembly;

(iii) the preparation of the Thermal Vacuum Test (TVT) chamber (vacuum at 77 Kelvin), equipped with Solar simulator and Earth infrared simulator, to reproduce and study the space environment;

(v) the optical and geometrical characterization of the "3×3" prototype with techniques of ground-based metrology.

While the candidate participated to all the phases of this R&D program, her original contribution was the design, the simulation of the prototype and its thermo-optical characterization. In particular, she devoted her 6-months work at LNF to the study of the time behavior of the thermal relaxation time of the LARES optical sensors in space, both in orbital conditions and in the TVT and climatic chamber at LNF. The position of these sensors, the Cuber Corner Reflectors (CCRs), is tracked ("ranged") by means of pulsed lasers on Earth and then used to measure the satellite orbit with a cm-level precision. The simple and precise geometry of LARES allows the most effective determination of its center of mass during its revolution around Earth.

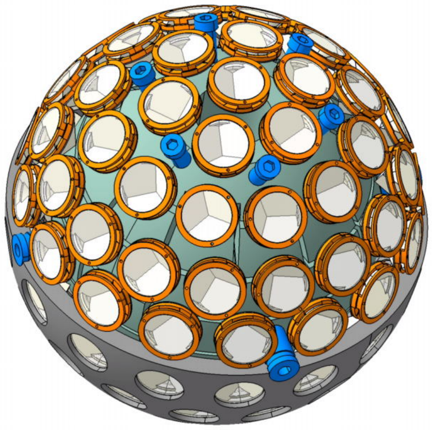

Figure 1.1: LARES satellite, new design.

Over typical times of a few years, the precession of the orbit of LARES can be determined accurately enough to measure the Lense-Thirring effect. However, this requires the knowledge of the deviation of the Earth geo-potential from the pure $1/r$ law and knowledge of the tiny, but relentless, perturbations of the orbit due to the Sun radiation pressure and to the infrared thermal radiation emitted by Earth. Only if these two contributions are subtracted from the raw precession rate, the Lense-Thirring effect can be extracted with success. The geo-potential is nowadays mapped with unprecedented detail by other on-going space missions. The thermal perturbations ("thrusts") are experimentally not well-known. This thesis work is the first attempt to directly model and estimate the thermal relaxation time of the CCRs when exposed to Sun and Earth. This is a key ingredient in order to subtract the effect of thermal thrusts and to be able to measure Einstein's frame dragging with 1% precision.

Finally, another important application of LARES, its ancestors, LAGEOS and LAGEOS II, and similar “laser-ranged” satellites, is in the field of Satellite Geodesy. The fine perturbations of their orbits allow the accurate determination of transient variations of the time and space (re-)distributions of masses on the Earth crust. This is relevant in view of the observations of precursor phenomena of extreme meteorological events, like El Nino and the anomalous melting of the polar ice caps.

The Lense-Thirring effect was first observed in 1998, 80 years after its prediction, using one NASA satellite (LAGEOS, 1976) and one ASI satellite (LAGEOS II, 1992), by the same Collaboration which is now proposing LARES to INFN, together with INFN-LNF, INFN-Lecce and the “Scuola di Ingegneria Aerospaziale” of the University of Rome I, “La Sapienza”. It is quite exciting that in 2005, during the Centennial of Einstein’s ”‘Annus Mirabilis”’ and the World Year of Physics, an experiment on the Lense-Thirring effect is in preparation to test this prediction of General Relativity at the level of 1% accuracy.

Chapter 2

The LARES experiment

2.1 Measurement of Lense-Thirring effect

Einstein's general theory of relativity predicts the occurrence of peculiar phenomena in the vicinity of a spinning body, caused by its rotation. When a clock that co-rotates very slowly around a spinning body returns to its starting point, it finds itself advanced relative to a clock kept there at rest (with respect to a distant star). Indeed, synchronization of clocks all around a closed path near a spinning body is not possible, and light co-rotating around a spinning body will take less time to return to a fixed point than light rotating in the opposite direction. Similarly, the orbital period of a particle co-rotating around a spinning body would be longer than the orbital period of a particle counter-rotating on the same orbit. Furthermore, an orbiting particle around a spinning body will have its orbital plane "dragged" around the spinning body in the same sense of the rotation of the body, and small gyroscopes that determine the axes of local, freely falling, inertial frame, will rotate with respect to "distant stars" because of the rotation of the body. This phenomenon, called "frame dragging", is also known as Lense-Thirring (LT) effect. In GR, all these phenomena are the result of the rotation of the central mass [5]. Until now two different methods have been planned to measure the Lense-Thirring effect according to the effect it has on gyroscopes and on orbital angular momentum.

Gravity Probe B (GP-B) was developed by NASA and Stanford University and launched on April 20, 2004 after a few decades of planning (the total cost was several hundred million US$). It contains four, almost perfectly spherical, spinning gyroscopes suspended in a vacuum. Indeed according to Newtonian physics, a perfect gyroscope, which experiences no external forces will not drift. In GP-B this would mean that once a gyroscope is spinning in alignment with the guide star, it would stay aligned with that star forever. GP-B has been built to measure two distinct effects of general relativity. The first, the geodesic effect, should cause the spin axis orientation of a gyroscope, cycling the Earth in a polar orbit, to change by a tiny angle of 6.6 arcsec (0.0018 degrees) in a year, relative to a distant guide star. The second effect, the LT, should cause the gyroscope axis to change orientation in the plane of Earth's rotation (orthogonal to the orbit plane) by a minuscule angle of 0.041 arcsec (0.000011 degrees) in a year. Conceptually the GP-B experiment is quite simple. An optical telescope faithfully points to its guide star, 6th-magnitude IM Pegasi. Initially the gyroscopes' spin axes are aligned through the bore side of the telescope to this guide star. A set of superconducting readout systems detect minute changes in each gyroscope's spin axis orientation. Changes in the spin axis alignment of the gyroscopes are a direct measurement of the geodetic and/or frame dragging effects of general relativity. GP-B gyroscopes limit any drift resulting from electrical and mechanical imperfection or forces acting on them. The GP-B instrument is designed to measure changes in gyroscopes spin axes orientation to better than 0.5 milliarcsec over a one year period [6].

LAGEOS (Laser Geodynamics Satellite), developed by NASA, was launched in 1976 with a Delta-2 rocket, while LAGEOS II, built by ASI (see fig. 2.1), was launched in 1992 with the Space Shuttle.

LAGEOS is a passive satellite. It carries no electronic equipment or moving parts. Mounted on the spherical satellite are 426 corner cube reflectors (CCR) that give LAGEOS its golf ball-appearance. The CCR carried by LAGEOS are three-dimensional prism that have the property to reflect light back to its source almost regardless of the angle the light is received by the satellite. The aim of the two LAGEOS satellite is to measure the "frame dragging" which should cause for a satellite with an orbital semi-major axis of 12000 km, like LAGEOS, a tiny shift of its node of about 33 mas in a year,

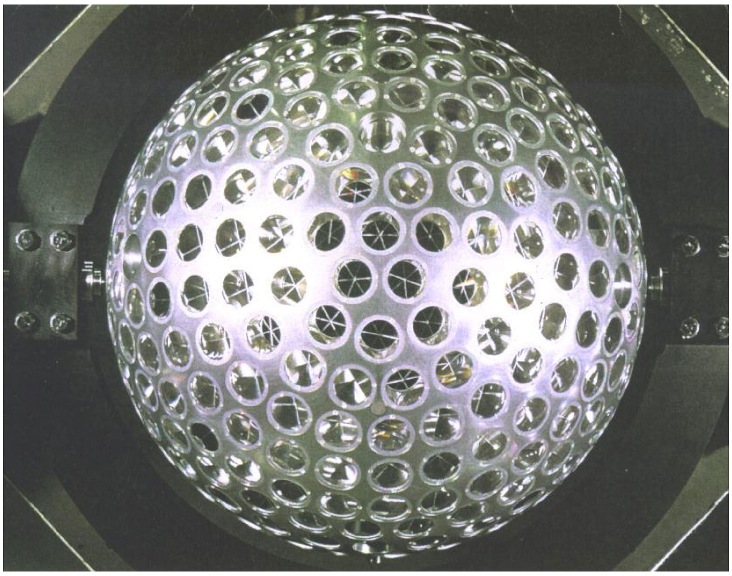

Figure 2.1: The LAGEOS II satellite, built in Italy in the 1990's.

that is nearly 1.9 m a year. Using the technique of laser ranging with CCR to send back the short laser pulses (see par. 2.3), it is possible to measure distances to a point of the moon with a precision of few centimetres, and distances to a small artificial satellite with a precision of a few millimetres. Furthermore, the instantaneous position of the two satellites can be measured with a precision of few millimetres and their orbits, with semi-major axes of 12270 km for LAGEOS and 12210 km for LAGEOS II, can be predicted, over 15-day periods, with a root mean-square-error of a few centimetres. The LT effect has been measured for the first time in 1998 and the value obtained was in agreement with general relativity, with an error much larger than the laser ranging resolution, arising from:

(i) the deviation of the geo-potential from the perfect 1/r behavior;

(ii) the following non gravitational perturbations (NGPs): the thermal thrusts (TTs) due to solar radiation pressure, the Earth albedo and the Earth infrared radiation.

In year 2004 the preliminary 2002 EGM from GRACE data and a re-analysis of 11 years of LAGEOS and LAGEOS II data, see fig 2.2, allowed a decrease of the LT uncertainty to 10% (including also underestimated and unknown sources of error). This is to be compared to the uncertainty of the 1998 result, based on older geo-potential models, which is generally considered to be in the range 20-40%.

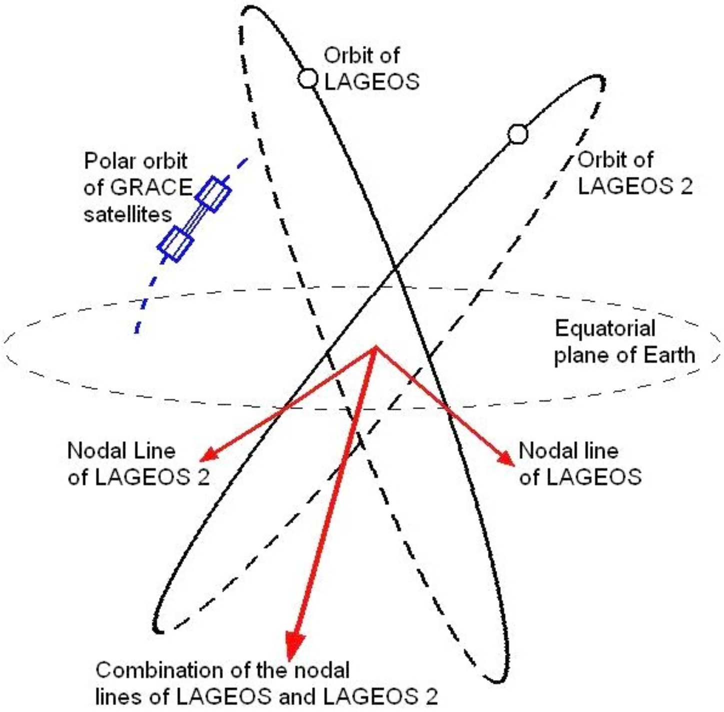

Figure 2.2: The two LAGEOS and the two GRACE satellites.

2.2 The measurement technique

The satellite laser ranging (SLR) experiments, like LAGEOS, carry on board numerous CCRs which are used for tracking (ranging) their position along their orbits. CCRs are special mirrors which always reflect an incoming light beam back in the direction it came from; fig 2.3.

The satellite ranging is achieved by shining from Earth multiple laser beams (each associated with a telescope for aiming at the satellite) managed

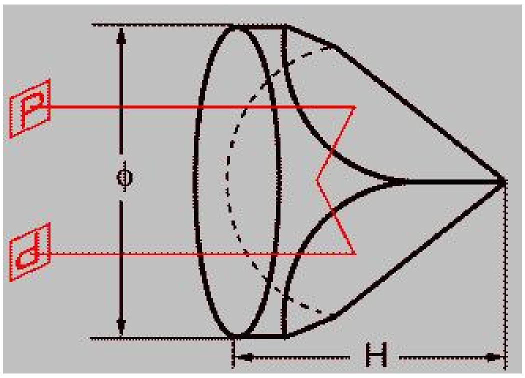

Figure 2.3: Total internal reflection [8].

by the International Laser Ranging Service (ILRS). The reflected laser beam is also observed with a telescope, providing a measurement of the round trip distance between Earth and the satellite. A number of ranging experiments during the past three decades have provided important geodesy measurements, including the Earth Gravity Model (EGM) and its time variations.

The ancestor of the SLR technique was the Lunar Ranging Retro Reflector (LRRR) experiment deployed by the Apollo 11, 14 and 15 mission to the moon (a similar device was on board of the Soviet Union Lunakhod 2). This is the only Apollo experiment that is still returning data from the moon. The laser beam has a 7 km diameter when it reaches the moon and about 20 km back to the Earth. The moon distance has been determined with an accuracy of 3 cm (the average distance is 384400 km). The LRRR experiment improved the knowledge of :

(i) the Moon's orbit;

(ii) the rate at which the Moon is receding from the Earth (currently 3.8 cm in a year);

(iii) variations in the rotation of the Moon;

(iv) changes of the Earth's rotation rate;

(v) the precession of the Earth spin axis (nutation).

In addition, the LRRR data have been used to measure the De Sitter or geodetic precession predicted by GR to an accuracy of 0.35%. This shift arises from the effect of the gravitational fields on the velocity of an orbiting gyroscope.

The data collected from LAGEOS and LAGEOS II with the laser ranging technique need to be processed. First, the orbit position and speed {x, y, z, $\dot{x}$, $\dot{y}$,$\dot{z}$} as function of time is determined. This task is accomplished using a software called GEODYN II, developed at NASA Goddard Space Flight Center in the past 30 years. The software allows fitting the range data with a suitable set of models, accounting for the various forces acting on the satellite, together with all the information useful to a correct data processing (such as a model for atmospheric delay of laser pulses). During the fitting procedure, it is usually necessary to estimate a number of parameters, in order to achieve the best accuracy possible. The process of extracting the set {state vectors, other parameters} is called data reduction. This is done by GEODYN for each arc (and analysis period), employing a numerical integration of the orbit and consequent adjusting of related parameters. The complexity inherent in the accurate description of satellite's orbit requires use of numerical models to take into account the following physics contributions:

(i) Gravitational perturbations (geo-potential, tides, De Sitter effect);

(ii) Non gravitational perturbations;

(iii) Reference frame;

(iv) Observation conditions and corrections.

Each of the previous points specializes into a number of separate models and parameter specifications.

2.3 The Geo-potential

SLR has been until recently the most important tracking data type for the mapping of the terrestrial gravity field with space techniques. SLR data are not only of high quality and unambiguous nature, they are also highly sensitive to any change in the location of mass of Earth and orientation of the terrestrial figure axis, as well as the positions and motions of the tracking sites. These unique attributes make SRL the clear choice for system that provides the reference frame information within the gravity model solutions. The recent increase of interest in the climate change processes on Earth has highlighted the unique contribution of SRL targets, and in particular of the two LAGEOS' in that area: the determination of tiny variations in the very-very low multipoles of terrestrial gravity field. These variations are directly related to mass redistribution in the terrestrial system (land, oceans, atmosphere). The international geophysical community has identified that as one of the present research areas of utmost importance. The media coverage of the worldwide devastation caused by El Nino underlined its importance to all and resulted in an unprecedented increase in public awareness for the problem as well as the efforts to better understand it and forecast it in the future. To better accomplish that, the international community is continuously striving to improve both the space segment as well as the ground segment of systems observing global climate change. Some of the most important "weapons" are the recently launched dedicated gravity mapping CHAMP and GRACE. They have already delivered new global models for gravitational field of Earth with unprecedented accuracy. Grace in particular, is now delivering multiple models covering monthly periods with half wavelength of about 250 km. This therefore has in part launched the era of temporal gravity monitoring at a previously unheard-of spatio-temporal resolution.

2.3.1 Other perturbations and error budget

We consider now additional gravity-related perturbations that affect the orbit of LAGEOS satellites and we quote the errors estimated in [7] for 11 years of LAGEOS and LAGEOS II.

The first one is another GR effect called "De-Sitter" effect or "geodetic precession". It produces a shift on a gyroscope that has been measured to an accuracy of about 0.35% using the Moon's orbit (LRRR experiment). This shift arises from the effect of the gravitational field on the velocity of an orbiting gyroscope. However, the De Sitter effect, which amounts to about 17 milliarcsec per year on the nodes of LAGEOS satellites, is today measured with 0.7% accuracy. Thus, the final error is about 0.4% of the Lense-Thirring effect.

Another source of error in measuring the LAGEOS orbit are the tides and the geo-potential errors. The error budget due to these perturbations is about 2% of the Lense-Thirring effect [7].

Finally, we consider random and stochastic errors and measurement errors. These include stochastic errors such as seasonal variations of the Earth gravity field, thermal drag (thrusts) and observation errors (both systematic and statistic). The budget for this class of uncertainties is about 2% of the Lense-Thirring effect [7].

2.4 Non gravitational perturbations

Among the various perturbative forces acting on a LAGEOS-like satellite, a crucial role is played by the effect of non gravitational perturbations (NGPs). These perturbations are generally characterised by complex and subtle long term effects in the satellite orbital elements, with periodicity which depends on the ascending node longitude, Ω, on the argument of perigee, ω, on the Sun longitude, λ as well as on their combinations. NGPs are proportional to the *area-to-mass* ratio of the orbiting body. That is why the LAGEOS satellites are characterised by a very small value of this ratio. To calculate the numerical value of the NGP, the Gauss perturbative equations on the satellite node and perigee have been used:

$$\dot{\Omega} = \frac{W}{H \sin I}\, r \sin(\omega + f) \tag{2.1}$$

$$\dot{\omega} = \frac{\sqrt{1-e^2}}{nae}\left[-R\cos f + T\left(\sin f + \frac{1}{\sqrt{1-e^2}}\sin u\right)\right] - \dot{\Omega}\cos I \tag{2.2}$$

where r represents the satellite distance from the Earth, H the orbital angular momentum, per unit reduced mass, of the two body problem, R , T and W are the Gauss perturbative accelerations in the radial, transverse (in the orbital plane and positive sense) and normal (out-of-the-orbital-plane, perpendicular to the other two) directions. Finally, *f, u, e, I, n,* and a are the true anomaly, the eccentricity anomaly, the eccentricity, the inclination, the mean motion and the semimajor axis of the satellite orbit [10].

2.4.1 Visible radiation effect: direct solar radiation pressure

For LAGEOS-type satellites, the largest non-gravitational force is due to the direct solar radiation pressure. By direct we mean the net acceleration resulting from the interaction (refraction, diffusion and absorption) of the incoming sunlight with each element of the satellite. Equation 2.3 gives the magnitude of the corresponding acceleration on a spherical and passive satellite:

$$\vec{a}_{\odot} = -C_R \frac{A\Phi_{\odot}}{mc} (\frac{D_{\odot}}{R_{\odot}})^2 \hat{s} \tag{2.3}$$

with ŝ the sun unit vector direction. $a_{\odot} = 3.6 \cdot 10^{-9} m/s^2$, where $A/m = 6.95 \cdot 10^{-4} m^2/kg$ is the area-to-mass ratio, c is the velocity of light , C_R is the dimensionless radiation coefficient ($\cong 1.12$), and $\Phi_{\odot}$ is the radiative flux (approximately the *solar constant* $\cong 1.38 \cdot 10^3 Watt/m^2$). The last squared term is due to the modulation coming from the eccentricity of Earth orbit around the Sun, where $D_{\odot}$ represents the Earth-Sun average distance while $R_{\odot}$ is the instantaneous Earth-Sun distance.[10]

2.4.2 Visible radiation effects: Earth albedo

By Earth albedo we mean the radiation pressure from Earth-reflected sunlight. Compared to the case of direct radiation pressure, modeling this force is more difficult and complicated. At LAGEOS altitudes the average flux from Earth is about 1/15 of the direct solar flux. The intensity and the direction of the albedo force are complex functions of position and time, since the local optical behavior of the Earth's surface and atmosphere is highly variable, related both to surface composition and to meteorological and seasonal effects. Equation 2.4 gives a simplified albedo formula useful to determine the periodicities of the albedo perturbations on the orbital elements:

$$\vec{a}_{al} = (a_r\hat{r} \, - a_s\hat{s})\,\Theta(f) \tag{2.4}$$

where a_r and a_s are the components of the acceleration in the radial and the Sun directions, while $\Theta(f)$ represents the so called albedo-shadow function [10].

2.4.3 Thermal thrust effects

Thermal thrust (TT) results from an anisotropic emission of thermal radiation by the satellite surface: on LAGEOS, this arises from a non-uniform temperature distribution over the surface. During the first years after launch, the LAGEOS spin period was short compared to the thermal heating and cooling time constants for its surface components, so the surface temperatures did not change appreciably over the spin period. The result is that any TT component perpendicular to the spin axis averages to zero over the spin period; only the thrust component along the spin axis is significant. The axial thrust depends on the temperature difference between the two surface hemispheres centered on each end of the spin axis; we will refer to these two hemispheres as 'north' and 'south'. The temperature difference arises from unequal heating of the hemispheres when the spin axis is not perpendicular to the heating source directions; the heat sources are solar radiation and infrared radiation emitted by the Earth. We are particularly interested in time variations with the orbit period in the temperature difference since the resulting axial thrust variations give secular changes to the orbit semi-major axis, inclination and node position [9].

The Solar-Yarkovsky effect

The Solar-Yarkovsky effect arises from the non-uniform absorption of the incoming visible solar radiation. In the assumption of a rapidly spinning satellite equation 2.5 gives the perturbation acceleration due to this thermal effect under this approximation:

$$\vec{a}_{YS} = -A_{YS}\Gamma(\zeta)\,cos(\xi)\hat{S} \tag{2.5}$$

where A_{YS} is the magnitude of the perturbing acceleration when the satellite is in full sun light, ξ represent the angle between the sun direction and the spin axis direction $\hat{S}$, finally Γ represents the so-called physical shadow-function which depends on the satellite longitude, ζ, measured from the orbital ascending node. The purpose of the Γ function is to model the decay of the incoming visible solar radiation when the satellite enters the Earth's shadow, as well as the growth of this flux, and consequently of the perturbative acceleration, when the satellite exits from the shadow. This means that the shadow-function is related to the satellite thermal relaxation time: in particular to the inertia of the CCRs [10].

The Earth-Yarkovsky or Rubincam effect

Consider the heating of the spacecraft north hemisphere by earth-infrared radiation as the spacecraft moves along the side AB of its orbit as shown in Figure 2.4.

Because of thermal relaxation time, the hemisphere is not warmest at orbit position A when the spin axis points mostly directly toward the earth, but rather at a later time when the satellite is at position B. The maximum TT occurs at this position; this maximum has a non-radial component that always points in the backward direction, that is, the thrust always has a drag (deceleration) component here. The north hemisphere then cools through radiation to space and the heating process repeats for the south hemisphere as the spacecraft moves along the arc CD; the maximum TT occurs at D and gives again a drag component. This periodic heating and cooling each hemisphere gives rise to the periodic 'Earth-Yarkovsky' or Rubincam effect [9]. The orbit position of the maximum TT is described by the so-called "thermal lag" angle, θ, whose expected value for LAGEOS is 55^o. The value of θ is related to the time thermal relaxation time of the CCRs (expected value $\approx$ 2000 sec) and to the satellite orbital period, 13300 sec. One of the main goals of this thesis is to directly model the CCR thermal relaxation time with a full blown simulation of the thermo-optical properties of the CCR, housed in the LAGEOS-type aluminum cavity, when exposed to the appropriate radiation sources (all available in SINDA-Fluint). The results

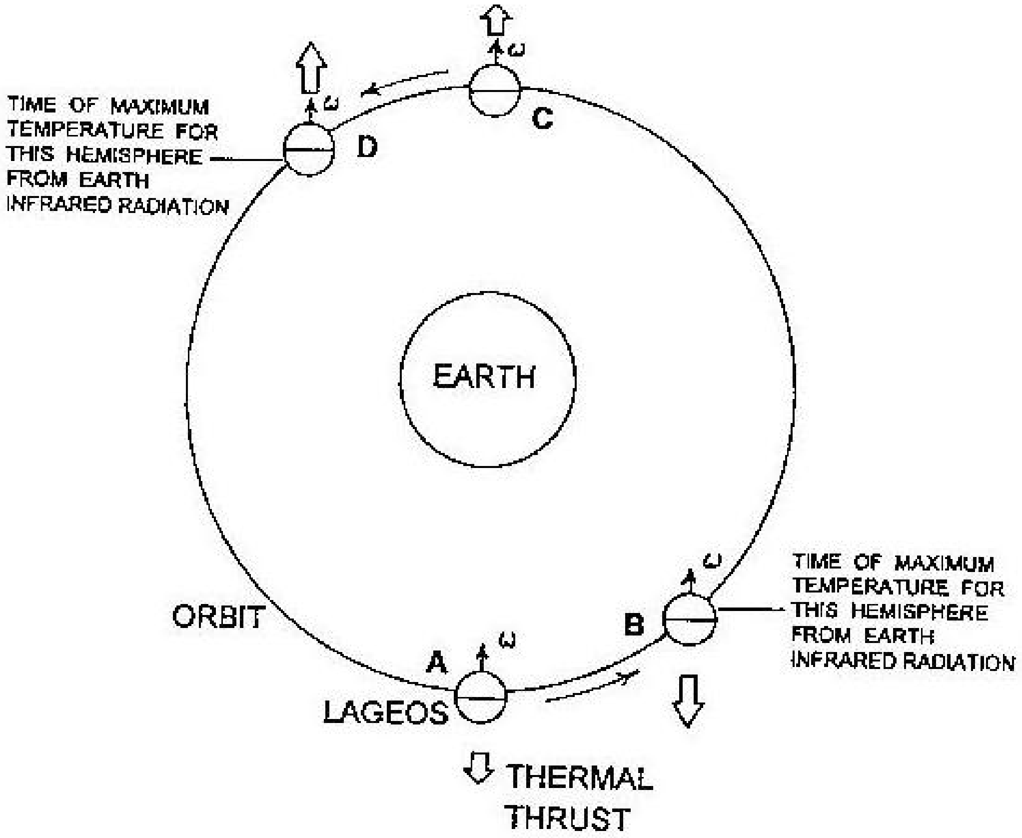

Figure 2.4: The Earth-Yarkovsky or Rubincam effect.

from this simulation will then be compared to the direct measurements taken with the LNF TVT and climatic facility.
Equation 2.6 gives the Rubincam perturbative acceleration:

$$\vec{a}_{EY} = A_{EY} cos(\psi)\hat{S} \tag{2.6}$$

where $\hat{S}$ represents the satellite spin unit vector, ψ is the angle between the satellite spin unit vector and the delayed unit position vector of the satellite.

The asymmetric reflectivity effect

The asymmetric effect is due to a small discrepancy in the effective reflectivities of the two hemispheres of the LAGEOS satellite. Indeed, in the case of the older LAGEOS, a small difference in the specular albedos of the two hemispheres,of about 1.5 %, produces a regular pattern of alternating peaks and troughs, of comparable magnitude, that reproduces many of the observed and unexplained along-track oscillations.

2.4.4 LAGEOS structure and calculation of TTs

The LAGEOS *spacecraft structure* is the sphere formed from two separate aluminum hemispherical pieces which meet at LAGEOS equatorial plane. The hemispheres surround a cylindrical beryllium-copper core with little space between components; this gives a spacecraft interior filled with solid material to minimize the *area-to-mass* ratio. The core cylindrical axis is coincident with the polar axis. Each hemisphere contains 213 CCRs embedded in the surface.

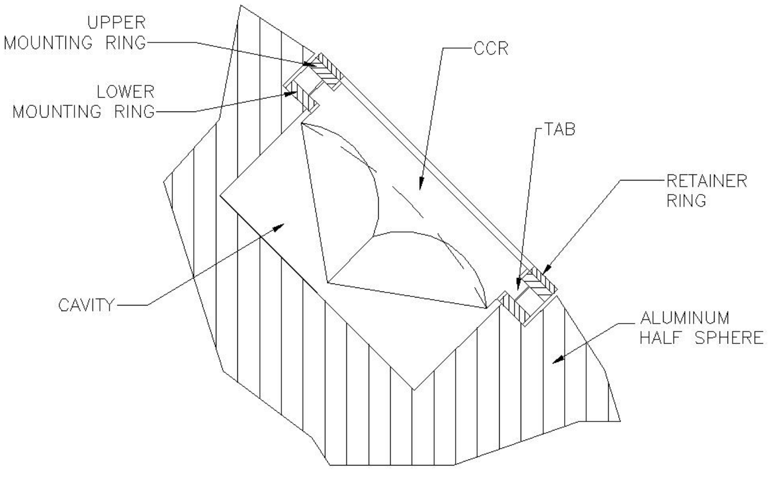

Figure 2.5: CCR assembly.

We consider the 426 CCRs in the space craft as made of fused silica even through four are made of germanium. Each CCR is held by ring assembly within a cylindrical cavity bored radially into the hemisphere. Two mounting rings machined from clear, transparent KEL-F fluoroplastic encircle the CCR. An aluminum retainer ring on the top of the upper mounting rings cover the open space between the cavity wall and the CCR and shields the plastic mounting rings from direct outside radiation, see fig.2.5. Three Al machined screws pass through holes in all the three rings to press the ring assembly against the Al shoulder of the cavity.

We now discuss the steady-state solution, presented by Slabinsky [9], for the LAGEOS I temperature and TTs. We assume a circular orbit and a spherical earth with a cylindrical shadow for simplicity.

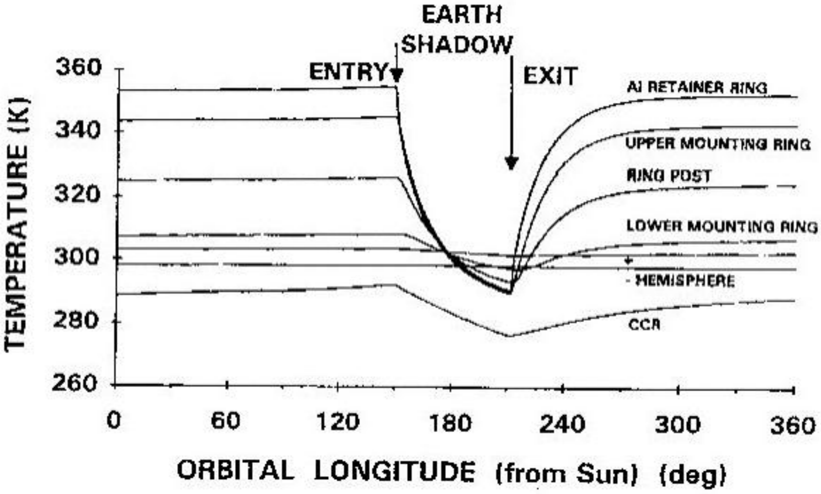

Figure 2.6: Temperature variation for LAGEOS components at sunlit pole [9].

Figures 2.6 and 2.7 show the steady-state temperature variation around an orbit that intersects the earth shadow. The first one shows that surface elements which are directly heated by the sun have a marked temperature drop following the interruption of solar heating when the satellite enters the Earth's shadow; these components show a marked temperature rise when the satellite leaves the shadow. The second one shows that polar CCR has a slight temperature variation with the orbit period as that CCR alternates between being heated by Earth infrared radiations it faces the Earth for half an orbit period, and than cooling as that region faces away from the Earth.

The sunlit Al retainer ring in Figure shows the largest temperature variation following shadow entry and egress because of its small heat capacity. The aluminum hemispheres show very little temperature variation around

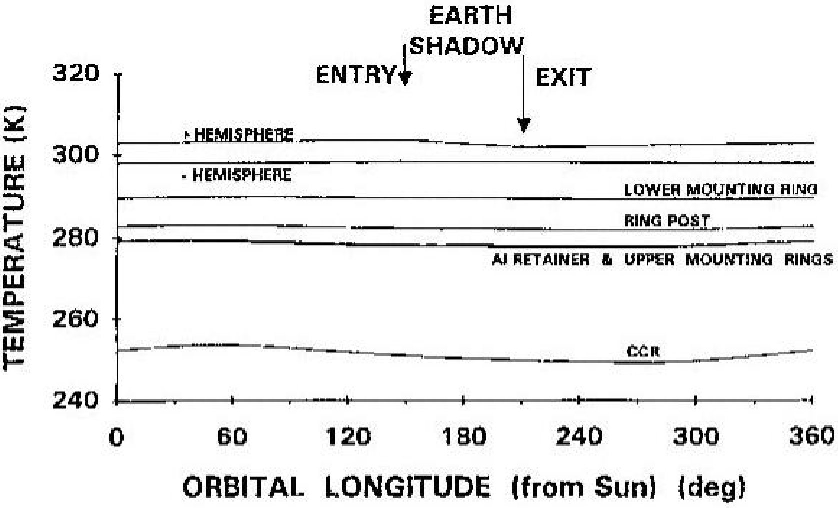

Figure 2.7: Temperature variation for LAGEOS components at dark pole the; the spin axis points toward sun and lies in the orbit plane [9].

the orbit because of their very large heat capacity.

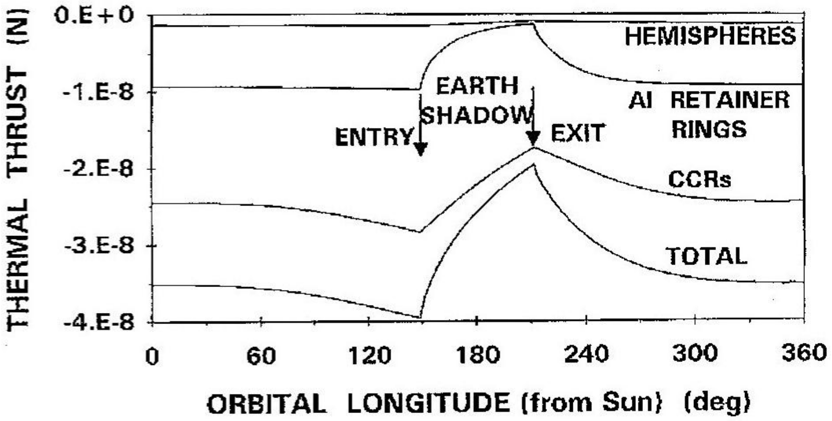

Figure 2.8: Thermal thrust due to the elements considered in figure 2.6 and 2.7; the spin axis points toward the sun and lies in the orbit plane [9].

Figure 2.8 shows the resulting net axial force on LAGEOS contributed by the different surface components. The CCRs make the largest contribution because of their high infrared emittance and the large difference in CCR temperature between hemispheres; because of their thermal isolation, the sunlit CCRs attain a much higher temperature than the CCRs near the rotation pole facing away from the sun. The Al retainer rings, whose coverage of the outer LAGEOS surface is one-half that of the CCRs, contribute only one third as much to the net axial surface force because of their low emittance results in less thermal radiation than is emitted by the CCRs.

The aluminum hemispheres contribute very little to the net force because the two hemispheres show a temperature difference of only 5 K with a resulting nearly equal thermal thrust on each hemispheres. Since the two thrusts are oppositely directed along the spin axis, the two thrusts nearly cancel.

2.4.5 Estimates of the error budget

The contributions of the previously computed NGPs to the final error budget have been analyzed in the following two cases: i) the sum of the nodes of LAGEOS and LARES, and ii) the nodes of LAGEOS satellites together with that of LARES, see equations 2.7 and 2.8:

$$\dot{\Omega}^{LAGEOS} + \dot{\Omega}^{LARES} = 61.7\mu_{LT} \tag{2.7}$$

$$\dot{\Omega}^{LAGEOS} + k_1\dot{\Omega}^{LAGEOSII} + k_2\dot{\Omega}^{LARES} = 61.5\nu_{LT} \tag{2.8}$$

with $k_1 = 0.003$ and $K_2 = 0.99$. Notice the small contribution of the LAGEOS II nodal rate to the relativistic measurement in the equation 2.8. This means that the final NGP error budget would be approximately the same for the two proposed combinations. Table 2.1 summarizes the contribution of each NGP to the error budget in the measurement of the LT effect for a time span of 7 years, relative to the Rubincam effect, taken as reference since it is the largest [10].

The error due to the Rubincam effect has been recently estimated in a published analysis of about 11 years of LAGEOS and LAGEOS II data [7] to be 2%.

We focus now on our main goal, that is reducing the error in the measurement of the LT to less than 1%, in relation to the error budget reported above.

Perturbation	**Error**
Direct solar radiation	0.13%
Earth albedo	0.22%
Solar Yarkovsky	0.16%
Earth Yarkovsky	2%
Asymmetric reflectivity	0.0014%

Table 2.1: Non-gravitational perturbations: error budget.

The thermal thrust effects on the node of the satellite have a very long period amplitude of the order of 2 milliarcsec/year, whose uncertainty is dominated by the uncertainty on the value of the CCR thermal relaxation time, τ_{CCR}. This is defined as the time needed for the CCR to reach about 2/3 of ΔT, the difference between the initial and asymptotic temperature ($1/e$ for a pure exponential behavior). τ_{CCR} has never been measured before. Its computed values in the literature span between 2000 sec and 7000 sec, i.e. an uncertainty of about 250%. However, the orbital thermal thrust effects are periodical and, as such, are averaged out over very long periods to the level of 90%. Ths is, the residual uncertainty is 25% = 250% × 0.1. Since the long period nodal perturbation of the thermal thrusts are **linearly proportional to** τ, corresponding to a very long period amplitude of the effect of the order of 2 milliarcsec/year, we have a relative uncertainty on the measurement of the LT effect of the order of 1% or 2% only from the thermal relaxation time ! The new simulation made with Thermal Desktop and the use of the TVT and climatic chamber at LNF allow thermometry with an uncertainty of a fraction of 1 K. This translates into a measurement of τ_{CCR} with an error of 2%, under the Sun illumination and 6% under Earth IR radiation (see 3.7).

2.5 LARES, a new generation satellite

With its 30 centimeter diameter, 100 kg weight and 102 CCR placed on the aluminum outer surface, LARES is a new generation satellite for a measurement of the Lense-Thirring effect within an error $\leq 1\%$.

Conservative approach In order to make such a precise measure, two different approach have been developed.
Following this idea, LARES has the same structure of the two LAGEOS satellites and the improvement in the measurement will be achieved by an accurate characterization of the spacecraft before the launch. The thermo-optical and the mechanical properties as well as their variation in space along the years will be input to Thermal Desktop, a specialized thermal software for satellites, and, ultimately also inserted into GEODYN to reduce associated errors. The main goal of this work is to suppress, when possible, or to accurately estimate TTs on the LARES satellite.

Innovative approach In order to suppress a large part of the TTs acting on the external surface of the satellite, a different mounting of the CCRs can be adopted; see fig. 2.9. In LAGEOS the aluminum retainer rings are fixed to the half sphere by means of three screws. Due to the poor thermal contact the retainer rings can be considered thermally insulated from the rest of the spacecraft. As a consequence, we find a 70 K difference between the rings in the "day" and "night" regions corresponding to the satellite being eclipsed or not by the Earth.

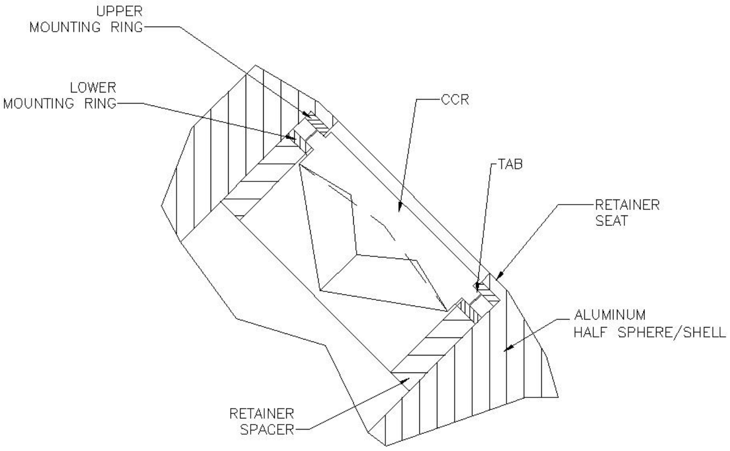

Figure 2.9: CCR cavity in the innovative approach.

In the innovative approach the CCR is inserted in its housing from the inside part of the spacecraft. Upper and lower mounting rings geometry can be maintained identical to LAGEOS. A retainer spacer fixes the assembly from the back part of the CCR. With this solution the TTs due to the LAGEOS retainer rings are completely null, since now the retainer element (a retainer seat) is mechanically machined from the spacecraft structure itself [11].

In addition to the different configuration of the satellite also the same analysis of the conservative approach will be done to be able to describe and simulate the forces experienced by LARES.

Chapter 3

Thermal simulations and planned experimental tests

3.1 Importance of the knowledge of the temperature distribution

Laser ranging shows that LAGEOS experiences an non-gravitational along-track acceleration with large fluctuations; this acceleration has a mean of about -3.4 pm/s^2, where the minus sign denotes a drag acceleration. This corresponds to a decrease in the semi-major axis of the orbit at a mean rate of 0.4 m/yr. We note that this force may actually vary around the orbit and also give acceleration components not tangent to the orbit, thereby producing secular perturbations to the other orbital elements.

The drag force required for this perturbation is much larger than predicted by the atmospheric density measured at lower altitudes and extrapolates to the LAGEOS 5900 km altitudes, an altitude with no other measurements of drag effects.

The most plausible mechanism to explain this drag phenomenon is the thermal trust due to the re-radiation of the absorbed earth-infrared radiation by the CCRs [9].

To address this issue we need an analysis that gives the temperature of each CCR and its mounting rings and allows for the poor conductivity across the equatorial joint between the two structural hemispheres in finding their temperatures. This is done both by means of software simulation (Sinda-Fluint) and by constructing a prototype of the satellite and testing it into the LNF TV and climatic chamber.

3.2 Planned thermal tests

The experimental tests on a single CCR and on the 3x3 matrix prototype aim to reproduce as realistically as possible the space and launch conditions through a TVT chamber, a solar simulator, an infrared Earth simulator and a vibration test. The IR camera and discrete temperature probes will measure temperatures and IR spectra emitted by CCRs and retainer rings under the different configurations. The data thus obtained will be inserted in SINDA-Fluint and used in a numerical integration for an evaluation of the expected TTs. Ultimately, the tests will be repeated on a full scale prototype, possibly with some spin.

A detailed characterization of the thermal behavior of the CCRs includes the estimate of different parameters:

(i) τ_{CCR}, the time needed by the CCR to reach 1/e of ΔT, the difference of the initial and the asymptotic temperature, when exposed to the Sun or the Earth IR radiation. This definition assumes the following exponential behavior:

$$T_{CCR}(t) = P1 + \ P2 \times e^{-t/P3}, \tag{3.1}$$

where P1 = T(∞), P2 = T(0) - T(∞), P3 = τ_{CCR};

(ii) τ_{RR}, the time needed by the retainer ring to reach 1/e of ΔT, the difference of the initial and the asymptotic temperature, when exposed to the Sun or the Earth IR radiation (see eq. 3.1). Note that the thermal relaxation time of the aluminum shell is irrelevant since its temperature and TT gradients have a negligible magnitude.

(iii) T(∞), the asymptotic temperature of the CCR;

(iv) evaluation of the IR emitted from the front of the CCRs;

(v) vibration test and re-measurement of all the above to investigate the effect of the launch on the satellite.

To achieve the above goal, we foresee two sets of measurements of T and of IR emission of the CCR and its assembly components.

1) Steady state (equilibrium) condition. We will get from the RadCad-SINDA simulation and the Slabinski calculation (see [9]) the expected temperature of the prototype in three basic geometric configurations:

    a) sun-facing;
    b) space-facing;
    c) 45^o to sun exposure.

    Then we will set the prototype base at the temperature calculated in each of these configurations and measure the temperature of the CCRs and the difference in kelvin between the CCRs and the aluminum shell.

2) Start at the three previous equilibrium temperatures and track the temperature evolution with time, turning on and off the solar simulator. Additional runs will be performed with small offsets in starting temperatures.

The RadCad-SINDA model will be tuned as necessary (and as possible) to reach a satisfactory agreement between simulation results and experimental data.

The required accuracy for this measurement campaign is 0.3 K for the IR camera (the LNF model has a 0.1 K accuracy) and a *calibrated* intensity of the solar simulator of a few % (again, achieved thanks to the available IR camera).

These tests will be crucial for LARES and will provide for the first time an experimental measurement of physical quantities directly related to the TTs experienced LAGEOS and LAGEOS II.

The climatic facility will also be used to characterize the proposed innovative satellite configuration (see par.2.5) without the aluminum retainer ring.

τ_{RR} will be compared to $\tau_{RetainerSeat}$ to demonstrate the decrease of the overall thermal thrusts by about 1/3. Everybody in the LARES Collaboration agrees that this would be a significant improvement and must be done.

3.2.1 Matrix design

The model of the 3×3 aluminum matrix has been built trying to reproduce as much as possible the geometrical arrangement of the CCRs on LAGEOS. The matrix surface is 153.6×153.6 mm^2 with a height of 50 mm. This thickness have been chosen to minimize the power of the thermo-cooler needed to stabilize the temperature of the aluminum. The distance from the center of one reflector to the nearest one, 51.2 mm, is the average value of the distances on LAGEOS. The orientation of adjacent CCRs (and their assembly components) are rotated by 26^o as on LAGEOS.

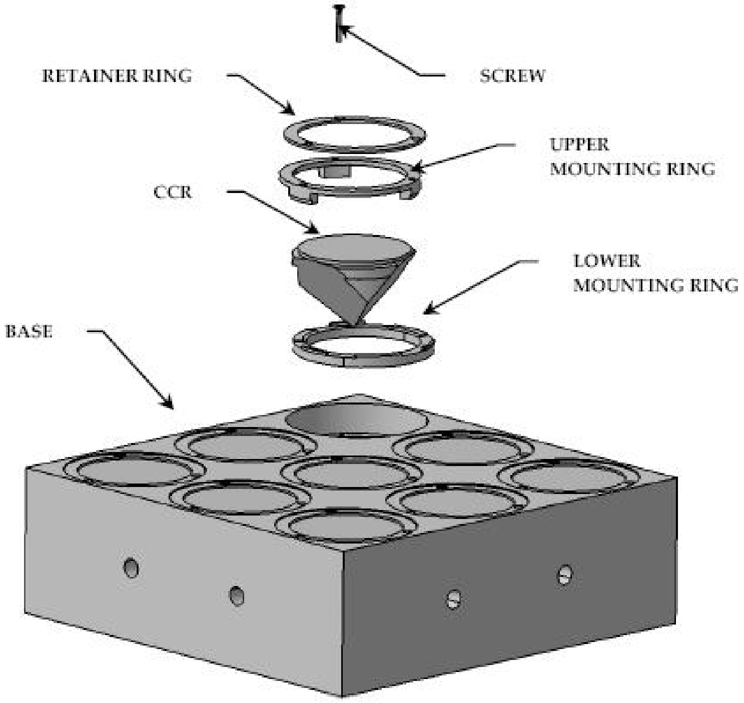

Figure 3.1: The 3×3 matrix.

As figure 3.1 shows, the CCR is held in its location by different mounting elements. Starting from the top there is an aluminum retainer ring with three holes for the screws. For the simulation we have simply modeled a ring of aluminum and we have insert a contact resistance between three nodes of its external surface and the circular base of the aluminum site. Since data for calculation of thermal resistance between the base and the screws are not available we consider this value equal to the conductance between screw head and retainer ring from [14]. Since we used nodes belonging to the aluminum ring to behave as screws, no thermal resistance between them and the ring can be modeled.

Going down in picture 3.1 we have the upper mounting ring. a KEL-F ring with three posts. Posts and ring have been simulated separately considering a conductance of 1 between their surfaces in contact.

The lower mounting ring is also made of KEL-F and and has thermal exchanges both with the posts of the upper ring and the base of the matrix.

Since the CCR is fit floating between the two KEL F rings properly shaped it can be considered thermally isolated from the rest of the assembly so table 3.1 reports only the values of conductance between the interfaces of the rings, the screws and the aluminum base [14].

first element	**second element**	**Conductance [W/K]**
Al Base	Screws	Unknow
Screws head	Retainer ring	0.16
Retainer ring	Upper mounting ring	0.46
Upper mounting ring	Lower mounting ring	0.44
Lower mounting ring	Base	0.46

Table 3.1: Thermal conductance.

3.2.2 Matrix hardware prototype

Once the matrix prototype was built (fig 3.2), different measurements were made on it in order to test the accuracy of the geometry. Figure 3.3 shows the two instrument used for that purpose: the 3D measurement machine with its mobile arm and the theodolite on the right.

Figure 3.2: The 3×3 matrix.

27 point on the aluminum support have been measured with the ruby tip of the mobile arm and elaborated by a specific software to obtain the average plane that is to say the plane that minimizes the average distance of each test point from it. The same work was repeated for the aluminum rings and the CCRs; for each element three points have been considered. Table 3.2 shows the average distance of the point from the plane and the maximum distance detected.

Plane of	average deviation (mm)	max deviation (mm)
Aluminum base support	0.002	0.007
Aluminum retainer rings	0.0053	0.237
CCRs	0.036	0.142

Table 3.2: Results from the 3D measurement machine.

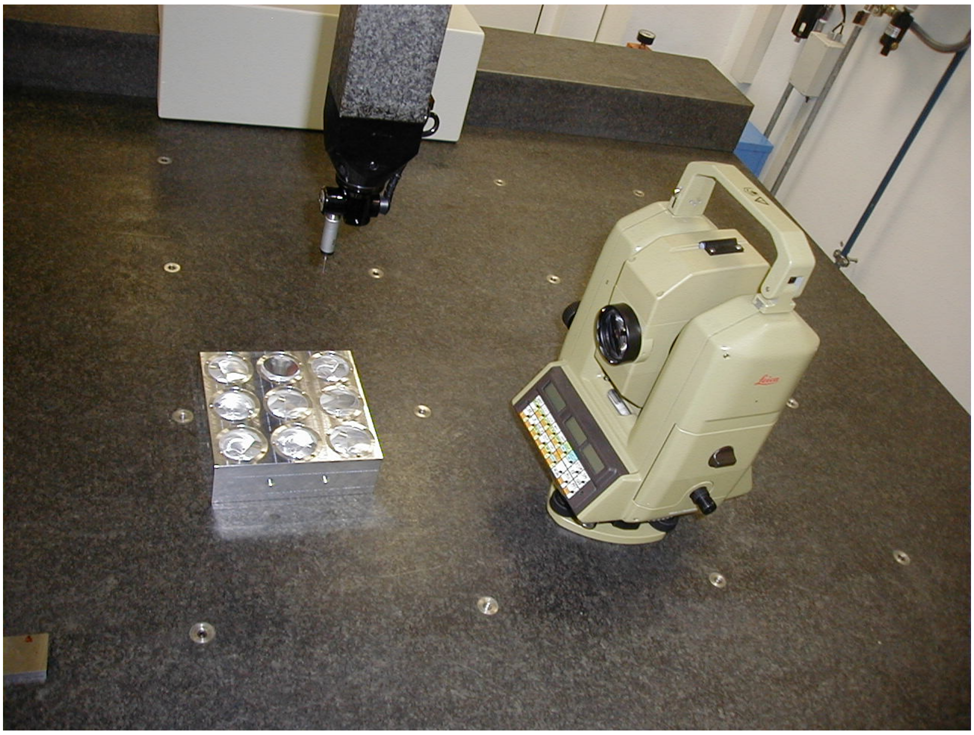

Figure 3.3: The 3D measurement machine and the theodolite

The results of table 3.2 confirm a good planarity of the aluminum support while a larger error on the plane of the CCRs and aluminum rings has to be attributed to a non-optimal tightening of the screws.

For a second type of measurement, the matrix was put on a vertical position on a leveled granite plane, and a theodolite with an embedded distance-meter was used to measure the horizontal distance between itself and each CCR. This measurement is based on the same light retro-reflection feature exploited by the ILRS lasers on Earth for any CCR in space. In table 3.3 we find the values obtained in millimeters; the position of the number in the table reflects the position of the CCR in the matrix as seen from the theodolite, whose measurement accuracy is 0.1 mm.

As expected the CCRs belonging to the same column have almost the same distance from the theodolite and the difference between the columns is due to growing of the distance moving away from the perpendicular to the matrix surface.

1832.4	1831.8	1832.7
1832.5	1831.8	1832.8
1832.4	1832.0	1832.8

Table 3.3: Results from theodolite measurements

3.3 The LNF Space Climatic Facility

The long term goal of the LARES R&D at LNF is to tune the simulation to reproduce the thermal behavior of a single CCR (and its assembly components) as measured with the climatic chamber. This will be repeated for a prototype made by a 3×3 matrix of CCRs. Experimental measurements will be done using a Sun simulator and an Earth infrared simulator. These will be turned on alternatively or simultaneously. The Sun and Earth radiation will be varied according to the known uncertainties and expected seasonal variations. After a satisfactory tuning of the software model, this will be used to predict the thermal behavior of the full satellite along its orbit, under the combined heat inputs of the Sun and the Earth. The combination of the TVT and climatic chamber plus the dedicated thermal simulation and CAD modelization software (described in the following sections) are the “LNF Space Climatic Facility” for low and medium Earth orbits. The construction of the CTF started in 2005.

3.4 The thermo-vacuum and climatic test chamber

In April 2005, the LARES LNF group started building a thermo-vacuum chamber using an existing dismissed cryostat designed to work with helium at 4.4 K. The cryostat is about 1 meter diameter and 2 meter length and is quite flexible due to many input/output ports and to its modular structure. To reach the temperature of 77 K needed for our tests, an absorptive copper shield is used. The liquid nitrogen runs through a coiled pipe joint brazed to the shield.

The LNF mechanics and cryogenics groups have re-commissioned the cryostat and then using thermo-pumps reached a vacuum condition of about 10^{-4} mbar. During this operation they performed helium sniffing to find leaks in the many access flanges of the cryostat. The process of cooling to 77 K is driven by the maximum pressure of the dewar and the proximity to the nitrogen supply. For the initial cooling we expected that about 40 liters will be consumed in several hours. At the steady state about 20 liters per hour will be required.

The duration of the measurement depends on: the CCR time constant, usually taken to be of the order of 0.8 hr (3000 sec; uncertainty of 250% and the satellite revolution time of about 3.8 hr (13700 sec).

We present now the configuration of the inside of the cryostat with the basic components of the tests: the prototype (single CCR, CCR matrix or 30 cm sphere) the solar simulator and the infrared simulator.

3.4.1 The Sun simulator

The solar simulator is a 25 cm diameter device positioned in front of the prototype at a distance of 0.9 m; see fig. 3.4

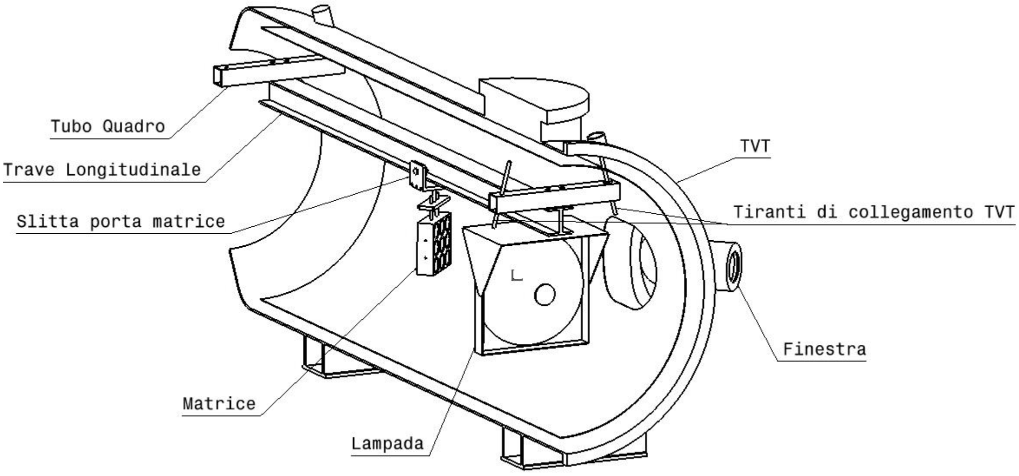

Figure 3.4: Solar simulator in the TVT chamber.

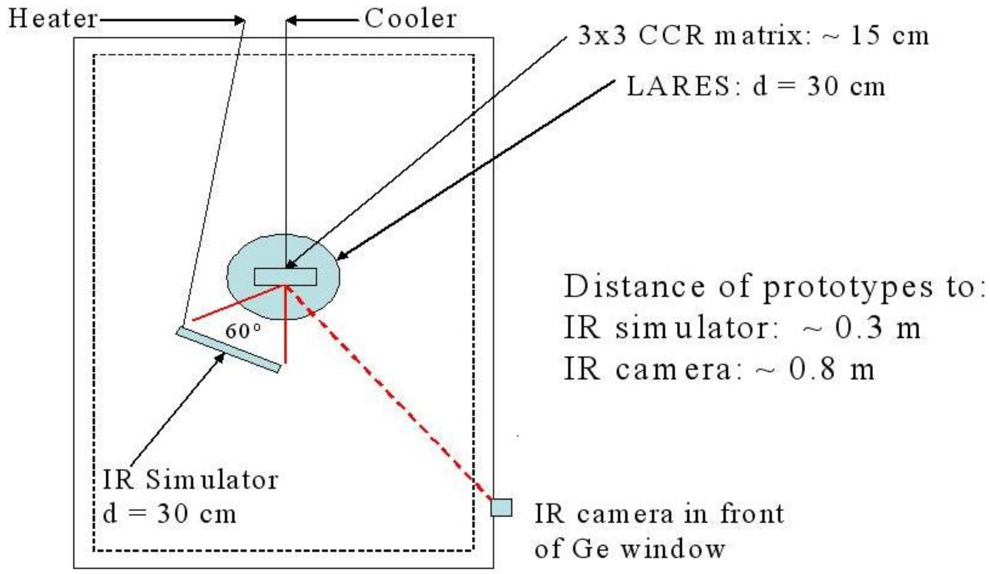

Figure 3.5: IR simulator in the TVT chamber.

3.4.2 The Earth simulator

The IR or Earth simulator is an aluminum disk, black painted and kept at 250 K. Its radius will be equal to its distance from the prototype in order to reproduce the 60^o viewing angle of Earth seen by LARES/LAGEOS; see Figure 3.5.

In a chamber at 77 K the simulator will cool down below the effective temperature of the Earth's upper atmosphere, 250 K. The black disk needs to be heated up by ~ 30 W, the amount of heat lost to the shield from initial 250 K. This can be carried out through a copper connection to AN outside temperature controlled heater or with a temperature controlled heater inside.

Like for the Sun simulator, the prototype working temperature will be controlled in order to perform the measurements around the target 300 K.

3.4.3 Thermometry and calibrations

Temperature measurements will be performed with an IR camera and with thermocouples. The IR camera, fig. 3.6, will be calibrated with a white "flat-field" device in the chamber and cross-checked by comparison with the thermocouples.

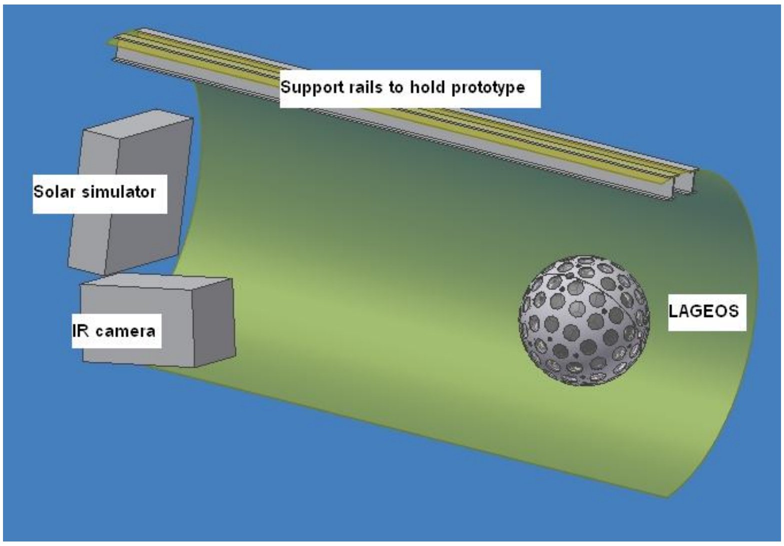

Figure 3.6: The TVT chamber. The solar simulator is inside the chamber while the IR camera is outside it.

The infrared camera will be located outside the cryostat. A germanium window is needed for the IR camera since other materials will absorb the wavelength of IR making the measurement not possible. The window will have a few cm diameter and 0.8 cm thickness. There are two possible positions for the camera, as shown in the picture. Probably, the side position will be chosen, while the other one will be equipped with a quartz window to allow visual inspection from the outside.

Thermography measurements require special training. A NEC TH7100 series IR camera (and the associated software) are owned by another LNF research group, which will kindly lend the equipment to our project. This camera has a good accuracy: 0.1 ^{o} C in the range [-20,+100]^o C. Personnel from our group has taken the class and the certification of “First Level Thermography Operator” in order to be able to operate the device and interpret the results.

The intensity of the chosen solar simulator beam has a relative uniformity of 10% over its area, which is not sufficent for the % level thermometry we are interested in. Therefore, we will map the beam intensity on a black-painted stainless steel disk using the IR camera. This disk represents a reference, "flat-field" black body. The collected map will then be input into the simulation software and taken into account in the analysis of the experimental data. The NEC camera has a good enough accuracy to provide the required % level relative calibration. This procedure will also provide the absolute temperature calibration and it will be cross-checked with the thermocouples.

3.5 The simulation software: Thermal Desktop and RadCad

Thermal Desktop is a program, produced by C&R (Cullimore and Ring), that allows the user to quickly build, analyze, and post process sophisticated thermal models taking advantage of abstract network, finite difference and finite element modeling methods. The Thermal Desktop offers the user full access to CAD-based geometry and CAD model building methods.This program can analyze thermal models consisting of 3D faces, regular MxN meshes, and arbitrary polyface meshes. These surfaces may be created directly, or by using various mesh generation commands such as surfaces of revolution, ruled surfaces, and edge defined patches. Thermal Desktop is not limited to just conic surfaces like many other thermal programs, it can also import, display, and analyze existing IGES, STEP and ANSYS models.

The main feature the user have to deal with are the nodes. Nodes represent a point at which energy is conserved. Each node has a single characteristic temperature T. Nodes may represent the temperature of a finite volume of material. They may be used more abstractly to represent boundary conditions, massless interfaces or edges, effective thermal radiation environments, etc. There are three types of nodes, classified by their capacitance or ability to transiently store or release thermal energy. Diffusion nodes have a finite capacitance C, usually equal to the product of mass and specific heat (mCp or VCp). Diffusion nodes may represent a finite cell within a meshed volume, or may represent a higher level component such as an electronics chip, a entire card, an entire chassis, a person, a vehicle, etc. Boundary nodes have an infinite capacitance, and hence usually represent sources or sinks, large masses, or ideally controlled temperature zones. Arithmetic nodes have zero capacitance: energy flowing into an arithmetic node must balance the energy flowing out at all times. Arithmetic nodes may be used to represent edges, interfaces, negligibly small masses (e.g., radiation shields or foils), and any other temperature to which no mass can or should be assigned.

Once defined the model, the user may direct the software to calculate the temperature with a steady state or a transient calculation. If both steady state and transient are selected, then the steady state is performed before transient is started. The transient run will begin with the temperatures computed from the steady state analysis [12]. Thermal Desktop will then give a plot to represent the temperature or the incident heat of each single element (node) and, for a transient solution, it is possible to obtain a graph of the behavior of a node through time.

3.6 Thermal simulation

3.6.1 The software package

Before starting to use the new software Thermal Desktop for the simulation of the satellite, we perform some simple calculation to getting use to it. The most interesting was to reproduce a calculation made with ANSYS to evaluate which is the most efficient heat transfer mode comparing radiation and radiation transferred by conduction between two plates. This will be used for the new solution proposed for the construction of LARES (see 2.5). Two square aluminum plates (50×50 mm^2)have been simulated at 150 mm distance, one at 301 K and the other at 300 K and an aluminum prism is placed in between facing the plates with 5 mm gap; we impose that the whole radiation exiting the two plates is absorbed by the prism.

The result of the steady state solution is illustrated in figure(3.7). The aluminum prism has now a temperature between 300 and 301 K and is hotter near the surface facing the 301 K plate.

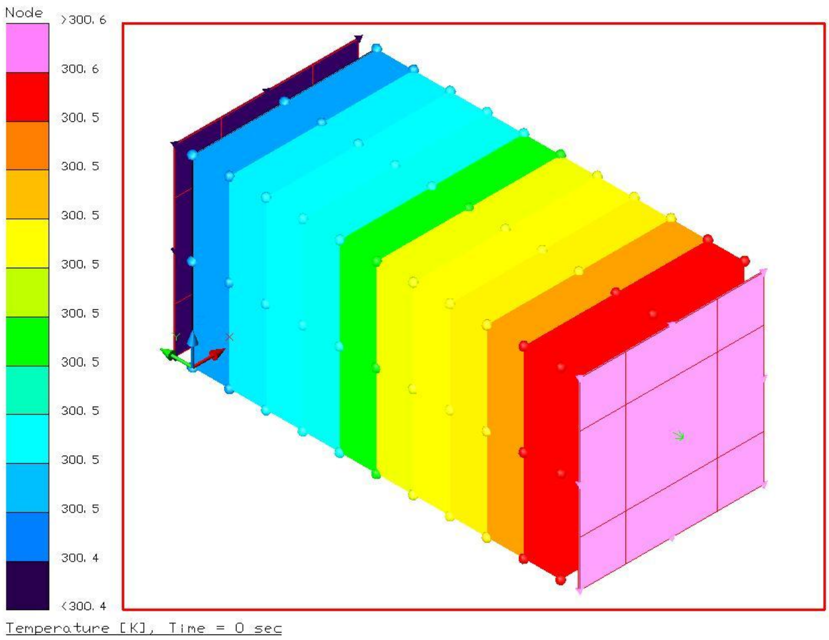

Figure 3.7: Aluminum prism exercise.

3.6.2 Building the software model of the matrix prototype

The model of the matrix was built using the following assumptions:

(i) We do not consider the conduction between the rings and the aluminum matrix;

(ii) We do not consider the conduction between the rings and the CCR;

For the optical properties of the different LARES components (see table 3.4) we referred to the parameters employed by Slabinski for his calculation on LAGEOS I [9].

Specific heat, density and conductivity of the material (see table 3.5) are also requested by Thermal Desktop in order to perform its analysis. We employed the specific heat of Slabinski's work [9] and we found the others properties on the website [13]

	solar spectrum			IR spectrum		
material	α	τ	**refr index**	ϵ	τ	**refr index**
Aluminum	0.42	0	1	0.2	0	1
Suprasil	0.15	0.85	1.46	0.81	0	1
KEL-F	1	0	0	0.93	0	1

Table 3.4: Optical properties.

material	**specific heat** $J/(kg\,K)$	**density** kg/m^3	**conductivity** $W/(m\,K)$
Aluminum	900	2702	167
Suprasil	753	2200	0.85
KEL-F	900	2130	0.2088

Table 3.5: Thermal properties.

In order to model the solar and the infrared simulator we used two surfaces, parallel to the external face of the matrix, shotting rays normal to their surface and so parallel one to the other. The solar simulator emits in the solar spectrum a flux of 1370 W/m^2. To calculate the emissive power of the Earth simulator we consider that the Earth emits 221.4 W/m^2 in proximity of the crust and that the the ray of the Earth is 6350 Km and the distance from the Earth surface to the satellite 6000 Km. The formula to obtain the flux results to be:

$$Q_{6000} = \frac{S_{Earth} * 221.4}{S_{12350}} = 58.5\ W/m^2 \tag{3.2}$$

Where Q are the watt pro squared meter received by a surface at 6000 km from the Earth, S_{Earth} is the surface of the Earth and S_{12350} the surface of a ball of 12350 km of ray.

3.6.3 CCR model: checks of the total internal reflection

As already said, CCRs have the typical property to reflect an incident beam (in the solar spectrum) back to its source. This is due to a total internal reflection on its 90° surfaces. Once we have built the model of the CCR we wanted to test this characteristic on it. First we put a solar lamp emitting normal from its surface in front of the external face of the reflector. The result of the test are in figure 3.8.

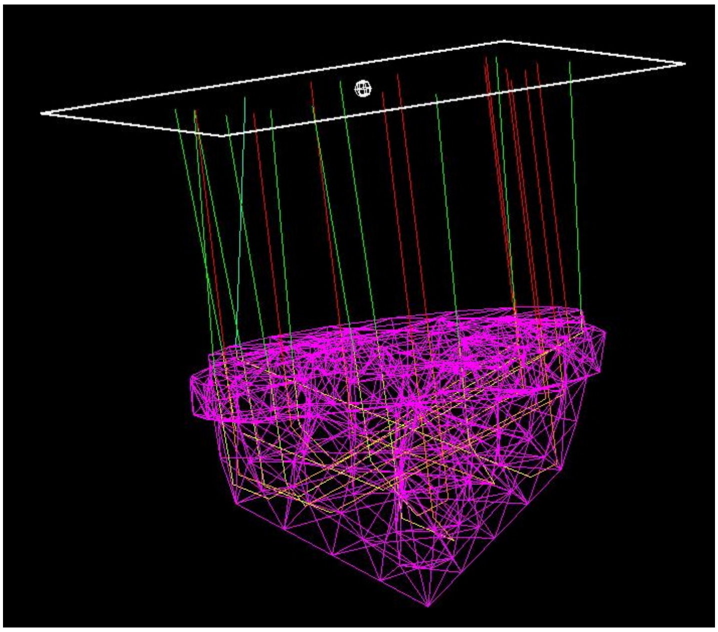

Figure 3.8: Total internal reflection.

The red incoming beams entering the surface, are partially absorbed by it and become yellow (the color, from red to dark blue, represent the intensity of the ray) then they have three complete reflection on the internal surface and exit the reflector perpendicular to the external face (a part from a little error due to the precision of the software), as they entered .

It is interesting to note that the an incident beam on the reflector not always comes back to its source. If the angle between the incoming ray and the normal to the surface is too large, (about 70°) the rays simply enter the CCR and exit from the first surface it find experiencing no reflection.

In the other case if the angle is between 70° and 0° there could be no complete internal reflection depending on the point the ray encounter the entering surface. Figure 3.9 shows a solar lamp placed 45° inclined. Only the rays entering the portion of CCR nearer to the source experience total

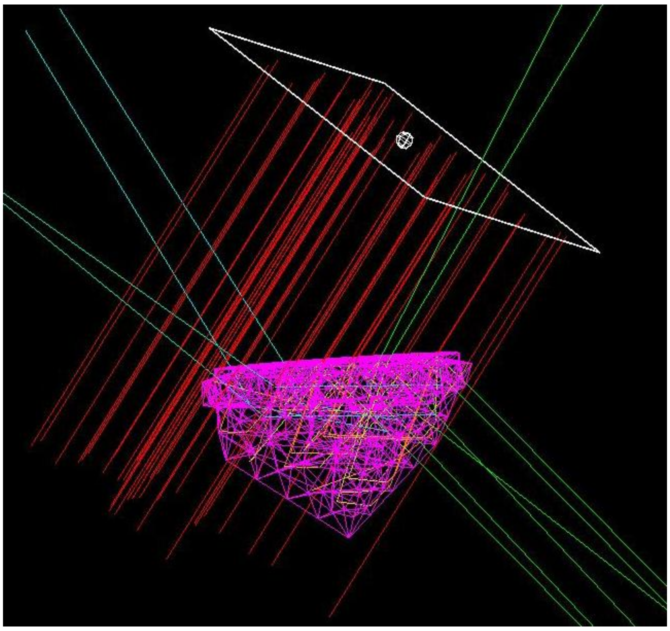

Figure 3.9: Reflection with inclined rays.

internal reflection and we can see green rays exiting from the top, that explain why the surface of the satellite is entirely covered by the CCRs so that we are sure that the ray send from the laser ranging stations comes back. Others rays simply exit the CCR from some lateral surface since during the reflection the incident angle grows and passes 70°.

3.7 Results of the simulation work

Before discussing the results we present a picture of the elements used for the simulation in Thermal Desktop (fig. 3.10). The complete 3×3 matrix, employed in the last simulations, was obtained by making an array of the previous piece and merging the coincident nodes.

The goal of this work is to perform a simulation of the thermal behavior of prototypes as described in section 3.2.

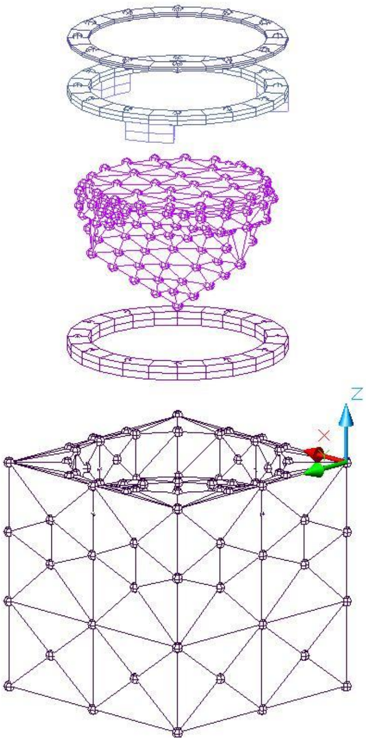

Figure 3.10: Model used for the simulation in Thermal Desktop. The CCR is modeled with 25o nodes.

3.7.1 Results from the single CCR model

We first study three different steady state solutions of one CCR and its aluminum cavity in a 3 K environment without the interaction of sun or IR radiation from Earth. We very the temperature of the aluminum (held fixed during the simulation) from 280 to 300 and 320 K and let the program find the asymptotic state for the CCRs. The pictures show the temperature distribution over the CCR in each of the different configurations.

Figure 3.11 represents the steady state condition when the temperature of the aluminum is fixed at 300 K, the expected average temperature of the LARES external aluminum surface in space.

Pictures 3.12 and 3.13 represent the solution for aluminum held first at a temperature of 280 K then at 320 K.

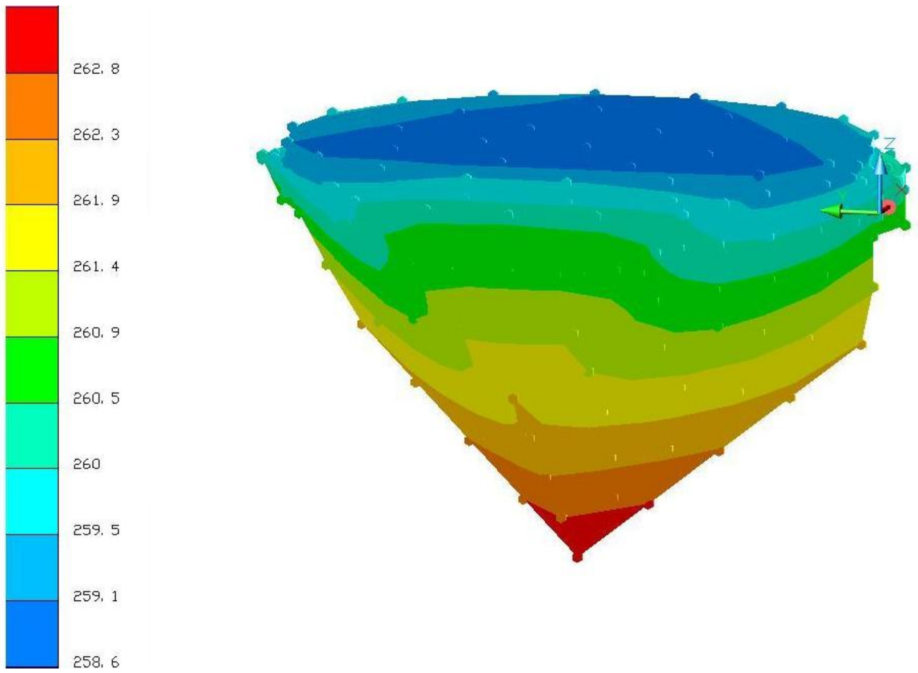

Figure 3.11: Steady state condition for 300 K aluminum.

From a comparison between the three pictures we note that the temperature distribution over the CCR is always the same and only the maximum and the minimum temperature change. It is interesting to underline that the internal gradient of the CCR increase with the growth of the aluminum temperature. In fact the temperature difference between the top and the bottom nodes is 3, 4 and 5 K when the aluminum is held at 280, 300 and 320 K, respectively.

We present now the transient analysis performed starting from different initial states and performed trying to reproduce the conditions the CCR will find in space and which can be tested most directly in the TVT and climatic chamber. For each simulation we report a graph that illustrates the evolution vs. time of the temperature of a node placed at the center of the superior surface of the CCR. A panel at the top right corner of the graph shows the results of an analytical fitting procedure based on the χ^2 method: the final temperature of the node (P1), τ_{CCR} (P3) and T(0)-T(∞) (P2). Next to each of these quantities the 1-standard deviation error (68% probability)

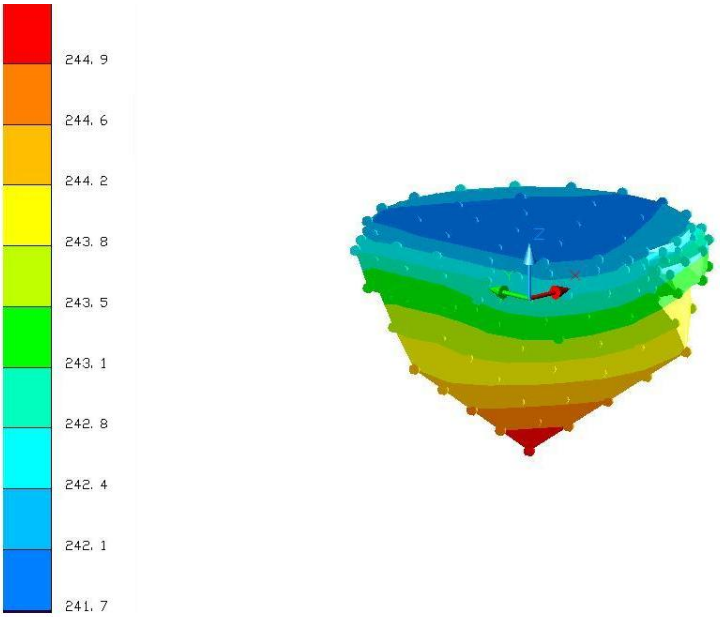

Figure 3.12: Steady state condition for 280 K aluminum.

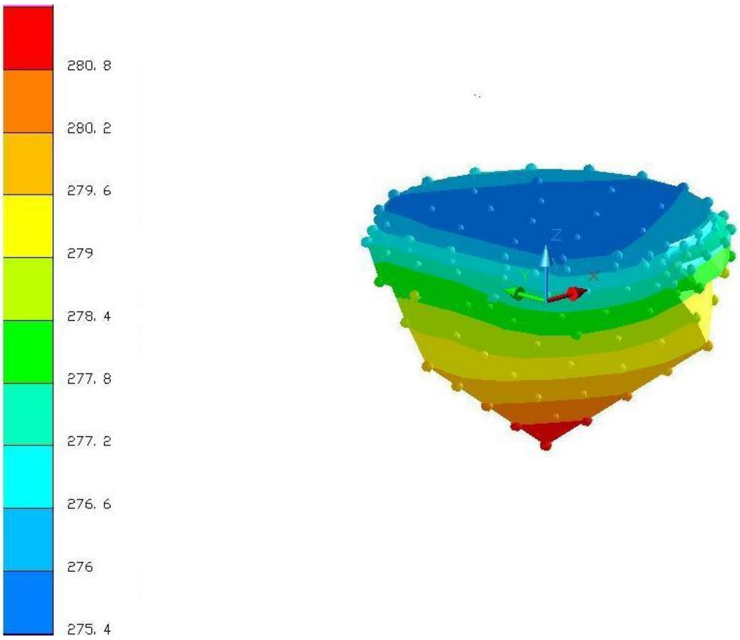

Figure 3.13: Steady state condition for 320 K aluminum.

on the fitted values is reported. All fits have been performed assuming an uncertainty of 0.5 K on the values of the simulated temperatures. This is a conservative assumption, since we foresee, ultimately, a better experimental accuracy For the first case only we also present a temperature plot of the final condition of the transient analysis and a graph reporting the temperature vs. time of four different nodes on the external surface of the CCR.

a. From sun and IR off to sun on and IR off

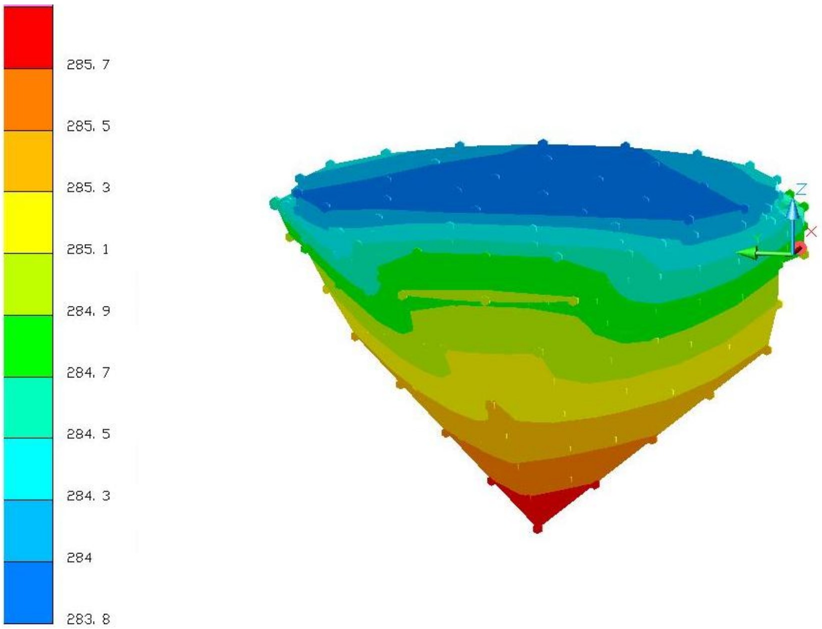

Figure 3.14: CCR temperature distribution at the end of a 12000 seconds transient analysis.

Picture 3.14 is the final state of the CCR after a transient analysis of 12000 seconds. At the beginning the sun and the IR lamps were turned off and a steady state solution have been calculated, then, starting from that condition, the solar lamp have been turned on.

The graph 3.15 is the evolution of the temperature of a node on the surface during the simulation while figure 3.16 shows a comparison between different nodes, the green line represent a node at the center of the top surface, the

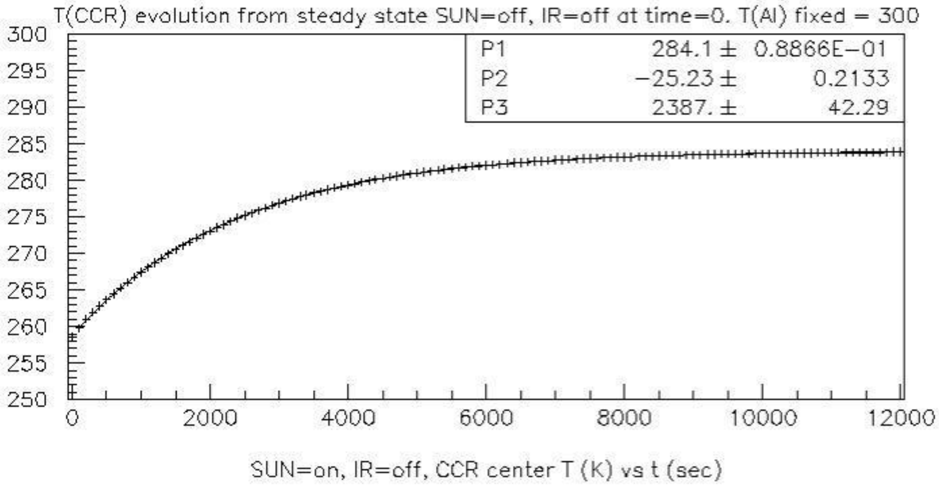

Figure 3.15: Temperature evolution vs. time.

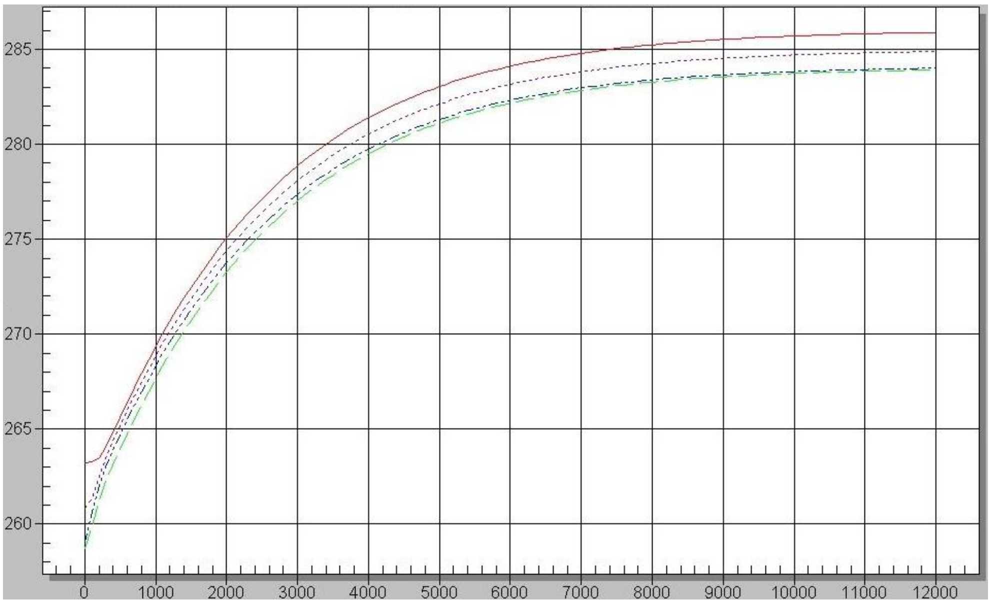

Figure 3.16: Temperature evolution for 4 different nodes.

red one is the node at the bottom of the CCR, the violet a node over a tab and the blue a node on the edge of the top surface.

The last picture of this section (fig. 3.17) shows the previous graph 3.15

with the value of the fit χ^2/ndf (ndf = number of degrees of freedom = number of measurements - number of fitted parameters - 1). Note that this and all other χ^2/ndf are much less than unity. This is because the simulated temperature values have not been smeared according to the 0.5 K accuracy assumed in the fitting procedure.

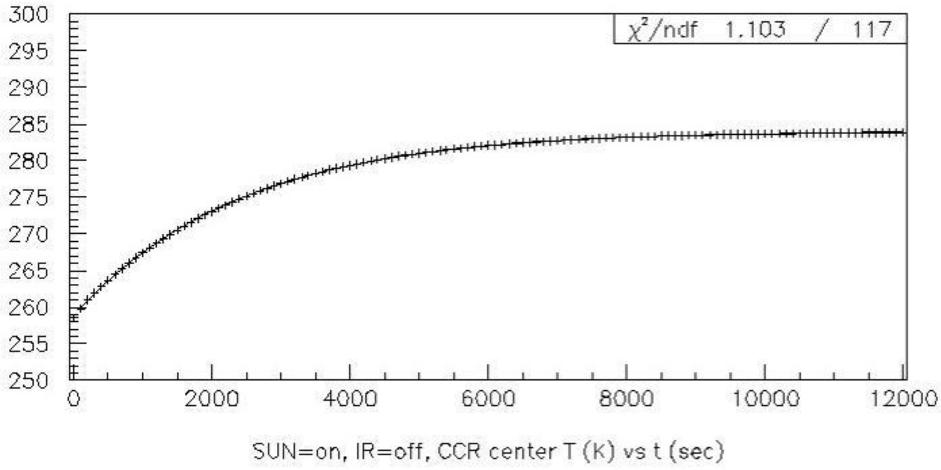

Figure 3.17: χ^2/ndf, which is a measure of the fit quality.

b. From sun and IR off to sun off and IR on

Picture 3.18 shows the temperature evolution vs. time of a node over the top surface. At the beginning the solar and IR lamps are turned off, then once reached the steady state solution the IR lamp is turned on and a transient analysis is performed for 12000 seconds.

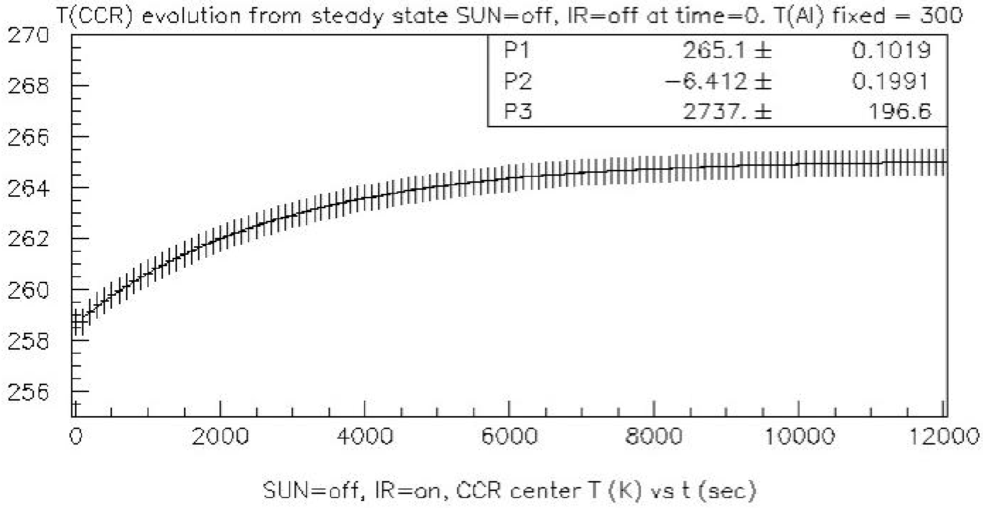

Figure 3.18: Temperature evolution vs. time.

c. From sun on and IR off to sun and IR on

Picture 3.19 shows the temperature evolution vs. time of a node over the top surface. At the beginning the solar lamp is on while the IR lamps is turned off, then once reached the steady state solution the IR lamp is turned on and a transient analysis is performed for 12000 seconds.

d. From sun off and IR on to sun and IR on

Picture 3.20 shows the temperature evolution vs. time of a node over the top surface. At the beginning the solar lamp is off while the IR lamp is turned on, then once reached the steady state solution the solar lamp is

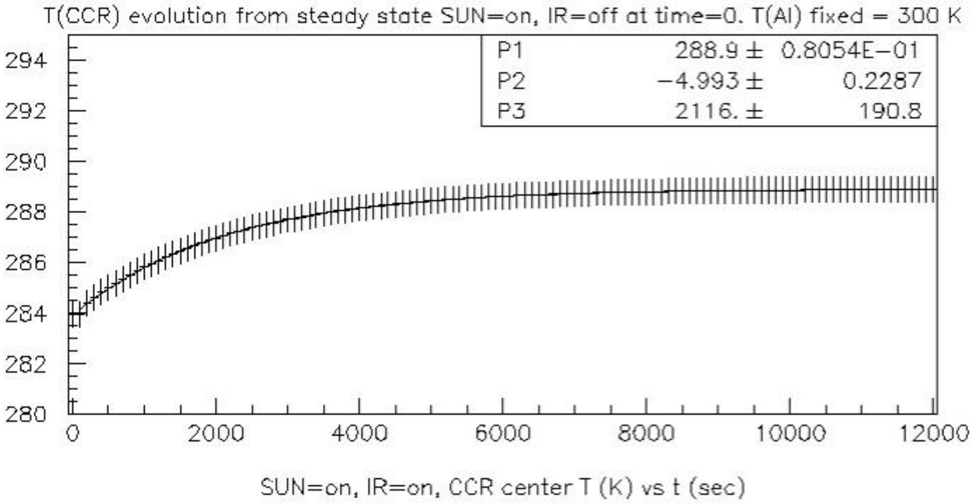

Figure 3.19: Temperature evolution vs. time.

turned on and a transient analysis is performed for 12000 seconds.

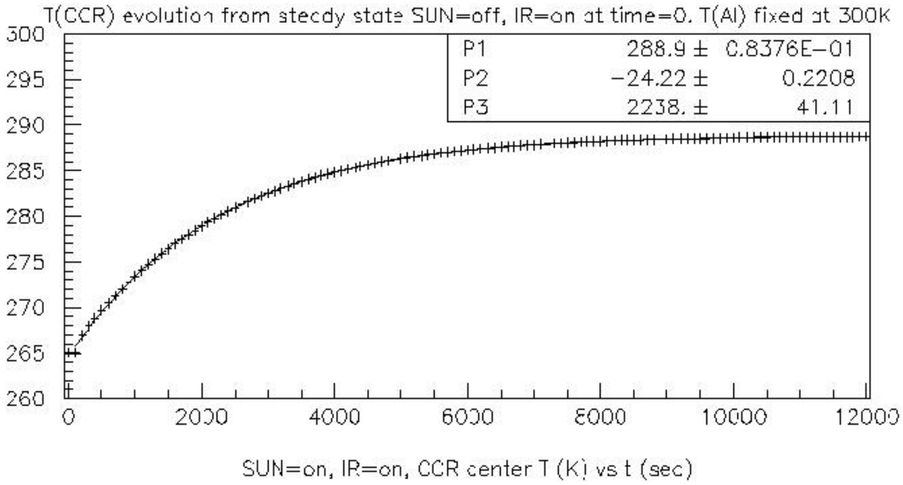

Figure 3.20: Temperature evolution vs. time.

e. From sun off IR off to sun and IR on

Picture 3.21 shows the temperature evolution vs. time of a node over the top surface. At the beginning the solar and the IR lamps are turned off, then once reached the steady state solution the solar and the IR lamps are turned on and a transient analysis is performed for 12000 seconds.

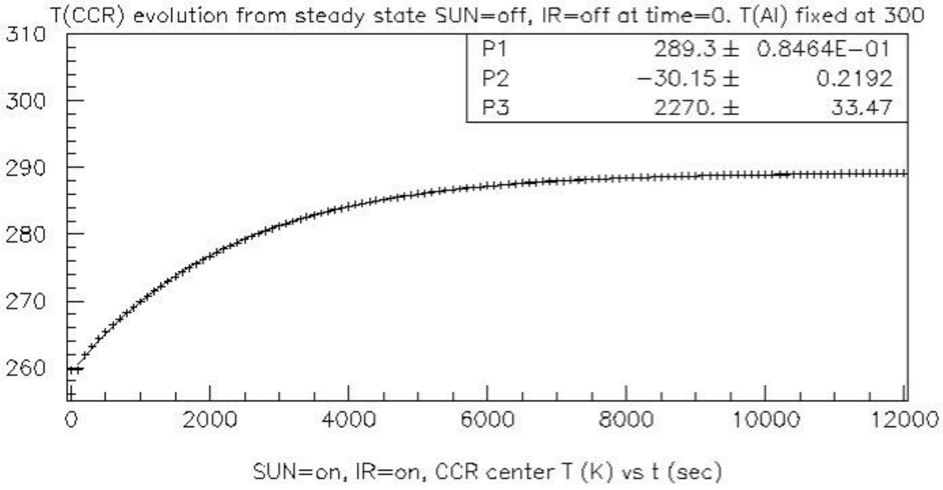

Figure 3.21: Temperature evolution vs. time.

f. From sun on IR off to sun and IR on (aluminum at 280 K)

Picture 3.22 shows the temperature evolution vs. time of a node over the top surface. At the beginning the solar lamp is on and the IR lamp is off, then once reached the steady state solution the solar and the IR lamps are turned on and a transient analysis is performed for 12000 seconds.

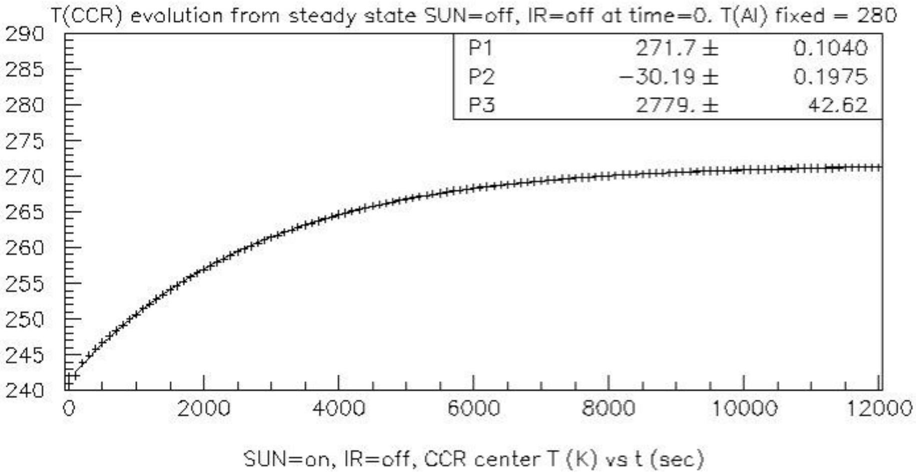

Figure 3.22: Temperature evolution vs. time.

We report now in table 3.6 the results of the simulation in terms of thermal relaxation time and error on it,

Case	τ_{CCR}	**error on** τ_{CCR}
a	2387	43
b	2737	200
c	2116	200
d	2238	41
e	2270	33
f	2779	43
g	2023	41
h	3321	216
i	2408	49

Table 3.6: Results

where the last cases are:

g. From Sun off IR off to Sun on IR off (aluminum at 320 K)

h. From Sun off IR off to Sun on IR on (aluminum at 280 K)

i. From Sun off IR off to Sun on IR off (Sun at 45^o)

3.7.2 Results from the 3×3 CCR matrix model

Due to the time needed to perform a complete transient simulation, two of the above configurations have been calculated for the whole matrix. We start from the steady state obtained when the matrix is in a 3 K environment, the aluminum is held at a temperature of 300 K and no solar or IR lamps are on (fig 3.23).

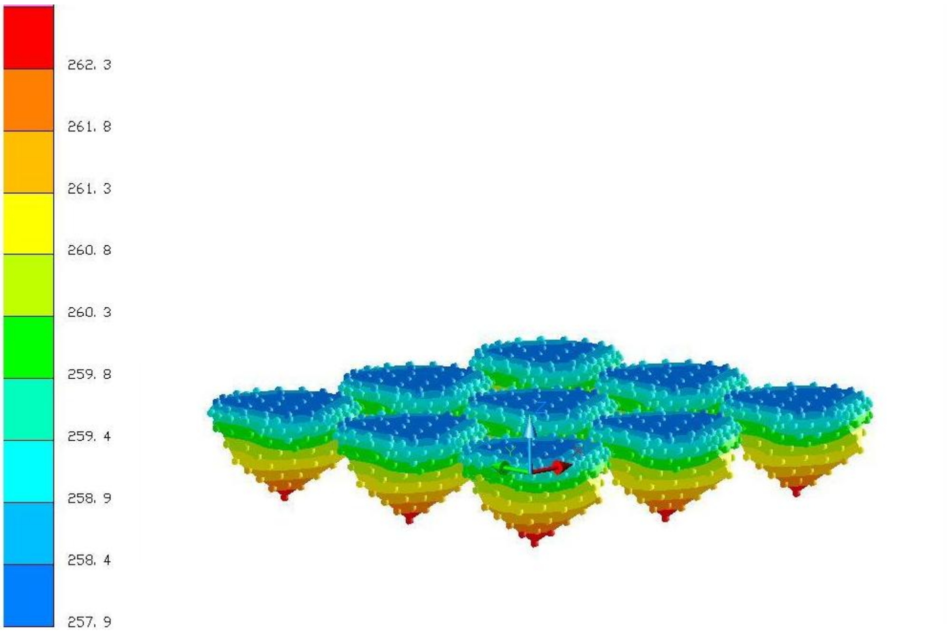

Figure 3.23: Matrix steady state solution for aluminum at 300 K.

We present now in table 3.7 the time constants for the whole matrix in cases:

1. From Sun off IR off to Sun on IR off
2. From Sun off IR off to Sun off IR on

Case	τ_{CCR}	**error on** τ_{CCR}
1.	2375	40
2.	2717	180

Table 3.7: Results for the matrix

3.7.3 Discussion of the results

The fits show that under Sun irradiation a temperature statistical accuracy of 0.5 K provides an uncertainty on τ_{CCR} of about 2% (40/2400). For Earth IR irradiation the uncertainty on τ_{CCR} is about 8 % (200/2400). In the experimental measurements we expect to reach an accuracy of 0.1-0.3 K and, therefore, to reduce the contribution of temperature errors below 5%, which is our ultimate goal.

Note that a reliable estimate of the systematic error on τ_{CCR} will only be possible using experimental data. However, to understand the size and the different sources of systematic error the simulation work will be very useful.

Assuming that both Sun and Earth IR irradiation are governed by a single thermal relaxation time, its central values from this simulation work is $\tau_{CCR} = 2400$ sec. The results are in good qualitative agreement with the Slabinski simulation for the LAGEOS satellites. The spread of the fit values of τ_{CCR} (about 2100 to 2700 sec) is larger that the statistical errors from each single configuration. This is due to the known variation of thermal relaxation times with $1/(T_r)^3$, where T_r is a typical average temperature value in the temperature range under consideration.

Without taking into account this explicit dependence of τ_{CCR} from temperature, and just as an exercise, we can quote:

$$\tau_{CCR} = 2400sec \pm 300sec, \tag{3.3}$$

where we take half of the spread of the fit values as error. This is an estimate of τ_{CCR} with a relative uncertainty of 12%, which is to be compared with the spread of 250 % among the computed values found in the literature. This 12% uncertainty would give a 0.1% contribution of thermal thrusts to the error budget on the measurement of the Lense-Thirring effect in General Relativity.

3.8 Conclusions

This simulation work has been very successful. A basic but complete modelization of the components which govern the thermal behavior of the past LAGEOS and future LARES satellites has been performed.

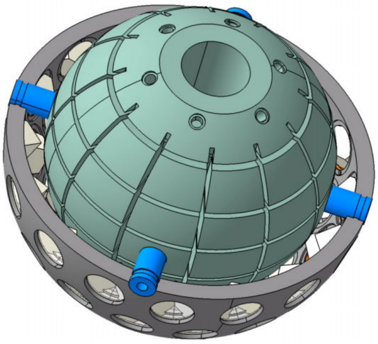

Figure 3.24: LARES satellite, new design.

The results obtained give a clear and very promising indication of the soundness of the experimental project of using a thermo-vacuum and climatic chamber to characterize the thermal properties of the satellites. They also show that the statistical power of the project satisfies the requirements imposed by the physics: the Lense-Thirring effect predicted by General Relativity can be measured with an accuracy of 1% or better only if the contribution of the thermal thrusts to the error budget is of the order of a few per 1000 or below. The simulation work started with this thesis, together with the experimental measurements appears well adequate to reach this goal.

An improved understanding of thermal thrusts will help the re-analysis of the LAGEOS and LAGEOS II data. It will also be the basis for an improved new design of the LARES structure, like shown in figures 3.24, 3.25.

Finally, controlling and reducing the effect of the thermal thrusts to unprecedented lower levels compared to the LAGEOS design, will make LARES a good approximation of the ideal point-like test particle in orbit around

Earth, subject only to the gravitational effects of the deviation of the geopotential from the pure 1/r behavior. Thus the LARES perigee could be used to search for additional precession due to new physics beyond General Relativity.

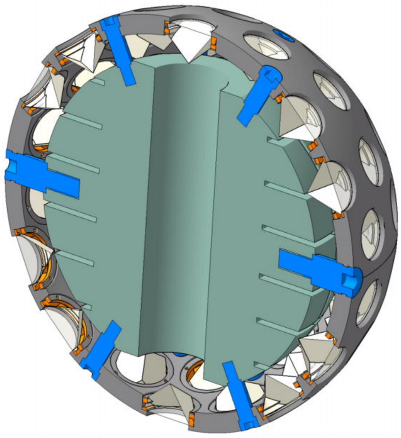

Figure 3.25: LARES satellite, new design.

Chapter 4

Appendix

GENERAL RELATIVITY[1]

The equations

$$R_{ab} = 8\pi(T_{ab} - \frac{1}{2}Tg_{ab}) + \Lambda g_{ab} \tag{4.1}$$

are called the Einstein's equations, often written in the equivalent form

$$(R_{ab} - \frac{1}{2}Rg_{ab}) + \Lambda g_{ab} = 8\pi T_{ab}. \tag{4.2}$$

Here R_{ab} denotes the Ricci tensor of the Lorentzian metric g_{ab} on the four-dimensional manifold M, R is the trace of R_{ab} (scalar curvature), T_{ab} is the energy-momentum tensor, T its trace, and $\Lambda \in \mathbb{R}$ is given. The constant 8π (in our units, otherwise $8\pi\frac{G}{c^4}$) is determined by requiring coincidence with the classical limit. Since both sides are symmetric, (4.1) forms a set of ten coupled second order partial differential equations in the unknowns (M, g_{ab}). The right hand side of (4.2) satisfies suitable compatibility conditions (in the form of conservation laws). In general the energy-momentum tensor depends on g_{ab}. System (4.1) must be coupled with suitable initial conditions (for instance, a three dimensional submanifold, a positive definite metric on it and a symmetric tensor of type $(0, 2)$). When $T_{ab} \equiv 0$ (4.1) are called vacuum Einstein's equations. Einstein's equations are invariant with respect to diffeomorphisms (coordinate transformations), namely if g solves (4.1) and

---

[1] This appendix has been written in collaboration with Giovanni Bellettini

$x'(x)$ is a diffeomorphism of M, then the transformed metric through x' still satifies (4.1).

Even if in general topological properties of M may be influenced by the metrics that one can assign on M (recall for instance the Gauss-Bonnet Theorem, or the Hamilton's program [18] and Perelman's further achievements toward the classification of three manifolds [23], [24], [25]) for simplicity here we will think of M to be fixed and given; we therefore disregard singularities where possible changes of topologies of M could be required (a singularity could appears when some geometric invariant, such as $R_{abcd}R^{abcd}$, blows up). Because of this assumption, we consider g_{ab} as the only unknown in (4.1) (up to diffeomorphisms of M). In this appendix we (very briefly) recall the origin of equations (4.1) and some basic facts of General Relativity.

Remark 4.0.1. In view of the experimentally observed deflection of light, it turns out that a conformally flat metric, i.e., a metric of the form $g_{\mu\nu}(x) = \lambda(x)\eta_{\mu\nu}$ (where $\eta_{\mu\nu}$ is the flat metric and $\lambda(x)$ is a positive factor) is not compatible with the presence of a gravitational field, since it defines the same light cones as $\eta_{\mu\nu}$, see [28].

Remark 4.0.2. In a neighbourhood of any point $x_0 \in M$, there exists a coordinate system (called inertial coordinate system) such that $g_{\mu\nu}(x_0) = \eta_{\mu\nu}$ and all the Christoffel symbols *evaluated at* x_0 are zero. The metric g describes the behaviour of clocks and measuring sticks in this local inertial system exactly as in special relativity. Hence, in this system, the usual laws of electrodynamics and mechanics in the special relativistic form are locally valid.

4.1 Preliminaries on differential geometry

We will mainly follow the notation and the statements in [30], to which we refer for all details. Except for Remark 4.2.4, we always will assume $\Lambda = 0$.

Unless otherwise specified, M denotes a four dimensional smooth Lorentzian time-oriented noncompact manifold (for instance $\mathbb{R} \times \mathbb{R}^3$). A Lorentzian metric g_{ab} on M (called also metric tensor, or metric for short, or also inner product) is a sufficiently smooth assignement of a non-degenerate quadratic form of index 1 (i.e., signature $- + ++$) in T_pM, where T_pM denotes the tangent space to M at p. Recall that $g_{ab} : T_pM \times T_pM \to \mathbb{R}$ is a symmetric tensor of type $(0, 2)$. We sometimes shorthand g_{ab} with g.

Recall also that a totally antisymmetric tensor field of type $(0, l)$ on M is a differential l-form, i.e., an element of $\Lambda^l TM$, where TM denotes the tangent bundle of M.

A hypersurface H is called space-like if at each $p \in H$ the induced metric $g_{|T_pH}$ is positive definite.

A curve is called time-like (resp. null) if the norm of its tangent vector is everywhere negative (resp. zero), $g_{ab}T^aT^b < 0$ (resp. $g_{ab}T^aT^b = 0$).

Remark 4.1.1. Vectors v^a (contravariant or controvariant) and covectors ω_a (dual vectors, covariant) must be kept distinct. However, recall that using the quadratic form g_{ab} we can define the duality mapping (in this case even a linear isomorphism $T_pM \to (T_pM)^*$ for any $p \in M$) $TM \to (TM)^*$ which allows to identify vectors and covectors based at p as follows. Given $v = v^a \in T_pM$ we can associate with v the element $v^* \in (T_pM)^*$ where $v^*(w) := g(v, w)$ for any $w \in T_pM$. Note that $v^* = g_{ab}v^b$, which is denoted usually by v_a (by raising in particular the * and using the lower roman index). Similarly, we can define the mapping $(T_pM)^* \to T_pM$ using the inverse g^{ab} of g_{ab}, i.e., by associating with ω_b the element $\omega^a \in T_pM$, where $\omega^a := g^{ab}\omega_b$.

Duality between covectors and vectors is sometimes denoted by $\langle \cdot, \cdot \rangle$.

Remark 4.1.2. More generally (see [2]) one could consider a sufficiently smooth function $\phi : TM \to [0, +\infty)$, which is positively one-homogeneous in v, i.e., such that $\phi(p, \lambda v) = \lambda \phi(p, v)$ for any $p \in M$, $\lambda \geq 0$, $v \in T_pM$ (a so-called Finsler norm), and define

$$g_{ab}(p, v) := \frac{1}{2}\partial^2_{v^a v^b}(\phi(p, v)^2). \tag{4.3}$$

Note that the duality mapping $T_pM \to (T_pM)^*$ acts as

$$v \mapsto \omega = \phi(p, v)\partial_v \phi(p, v) = g_{ab}(p, v)v^b, \tag{4.4}$$

in accordance with Remark 4.1.1. The pseudo-Riemannian (or Lorentzian) case considered in the present chapter is when g_{ab} does not depend on v, i.e.,

$g_{ab}(p,v) = g_{ab}(p)$. Equivalently, the Cartan tensor

$$C_{abc} = \frac{1}{4}\partial^3_{v^a v^b v^c}(\phi^2) = \frac{1}{2}\partial_{v^c} g_{ab}$$

is identically zero.

In the following ∇ denotes the Levi-Civita connection on M (or affine connection, or metric derivative, referred here as *the* covariant derivative) which, once g_{ab} is given, is the unique torsion-free derivative operator on M [30, pag. 31] compatible with the metric, namely such that

$$\nabla_a g_{bc} = 0, \tag{4.5}$$

which is equivalent to parallel transport, i.e., given vector fields v^a and w^b with $t^a \nabla_a v^b = 0 = t^a \nabla_a w^b$, t^a the tangent vector to a curve, then

$$t^a \nabla_a (g_{bc} v^b w^c) = 0 \tag{4.6}$$

(the inner product $g_{ab} v^a w^b$ remains unchanged if we parallel transport them along a curve).

Recall that, if f is a function defined on M, $\nabla_a f$ is a covector (hence $\nabla_a f$ is the generalization of the usual differential of f).

Recall that $\nabla_a v^b$ is a tensor of type $(1,1)$, that when contracted with a vector field w^c (i.e., $w^a \nabla_a v^b$) produces the vector field usually denoted by $\nabla_w v$, the derivative of v along w.

The covariant derivative is torsion free, i.e.,

$$\nabla_a \nabla_b f = \nabla_b \nabla_a f, \tag{4.7}$$

where f is a function defined on M.

Finally, recall that $\nabla_u g(v,w) = g(\nabla_u v, w) + g(v, \nabla_u w)$.

We set

$$\mathcal{G} = \det(g_{\mu\nu}). \tag{4.8}$$

We recall the expression of the connection coefficients (or Christoffel symbols, or Cartan connection coefficients) in terms of g_{ab},

$$\Gamma^c{}_{ab} = \frac{1}{2} g^{cd}\{\partial_a g_{bd} + \partial_b g_{ad} - \partial_d g_{ab}\} = \Gamma^c{}_{ba}, \tag{4.9}$$

where ∂_a is defined by the coordinate system (ordinary derivative). Therefore,

$$\Gamma^{\rho}{}_{\mu\nu} = \frac{1}{2} g^{\rho\sigma} \left\{ \frac{\partial g_{\nu\sigma}}{\partial x^{\mu}} + \frac{\partial g_{\mu\sigma}}{\partial x^{\nu}} - \frac{\partial g_{\mu\nu}}{\partial x^{\sigma}} \right\} =< \omega^{\rho}, \nabla_{\mathbf{e}_{\mu}} \mathbf{e}_{\nu} >, \tag{4.10}$$

where $\mathbf{e}^{\alpha}$ (resp. ω_{β}) is a basis of the vectors (resp. covectors) in a neighbourhood of p.

In particular

$$\Gamma^{a}{}_{a\mu} = \frac{\partial}{\partial x^{\mu}} \log(\sqrt{|\mathcal{G}|}),$$

It turns out that

$$\nabla_a t^b = \partial_a t^b + \Gamma^{b}{}_{ac} t^c, \tag{4.11}$$

$$\nabla_a \omega_b = \partial_a \omega_b - \Gamma^{c}{}_{ab} \omega_c, \tag{4.12}$$

and so on.

The tangential divergence of a vector field T^a can be written as

$$\nabla_a T^a = \partial_a T^a + \Gamma^{a}{}_{ab} T^b = \frac{1}{\sqrt{|\mathcal{G}|}} \frac{\partial}{\partial x^{\mu}} (\sqrt{|\mathcal{G}|} T^{\mu})$$

The tangential laplacian of a function f reads as

$$\Delta f = \frac{1}{\sqrt{|\mathcal{G}|}} \frac{\partial}{\partial x^{\mu}} (\sqrt{|\mathcal{G}|} g^{\mu\nu} \frac{\partial}{\partial x^{\nu}} f)$$

In the Riemannian case it is the Laplace-Beltrami operator with respect to the metric. In our (Lorentzian) case, it is the d'Alambertian with variable coefficients.

Recall that there are two other notions of derivative in M, namely the exterior derivative (denoted by d) and the Lie derivative (denoted by $\mathcal{L}$).

We recall that a vector field K is called a Killing vector field (see [30, pag. 439]) if it generates a group of isometries of M. The Lie derivative $\mathcal{L}_K g$ of the metric g with respect to K is identically zero, more precisely the following Killing's equation holds:

$$0 = \mathcal{L}_K g_{ab} = 2\nabla_{(b} K_{a)}. \tag{4.13}$$

It can be shown [19, pag. 43] that (4.13) characterizes Killing vector fields, i.e., a vector field K which satisfies (4.13) is a Killing vector field. The importance of Killing's vector fields is that they give raise to constants of the motion [30, pag. 442].

Remark 4.1.3. In a Riemannian manifold N, the metric tensor g_{ab} can be obtained from the metric, as follows: given $p \in N$, setting $\eta(q) := \mathrm{dist}(p,q)^2$, then η is smooth at $p = q$, the first differential of η vanishes as p, $\nabla\eta(p) = 0$, and the second differential $\nabla^2\eta(p)$ of η at p is a quadratic form on T_pN which coincides with g_{ab}. In view of the expressions (4.10), (4.24) it would be interesting to invert the expression of the Riemann tensor of N in terms of the derivatives of η up to order four. See also [26].

Given a subset $B \subseteq M$ covered by a single chart (or coordinate system) $\psi : M \to \mathbb{R}^4$, we define

$$\int_B d\mu_g = \int_{\psi(B)} \sqrt{|\mathcal{G}(x^1, \ldots, x^4)|}dx^1 \ldots dx^4,$$

where $dx_1 \ldots dx_4$ is the Lebesgue measure in $\mathbb{R}^4$, (see for instance [16, pag. 103]). μ_g is the natural volume element induced by a metric tensor which is obtained from g_{ab} by "reversing" the minus sign in g_{ab}.

Remark 4.1.4. When N is a Riemannian manifold and $B \subseteq N$, it turns out that $\int_B d\mu_g$ is the Hausdorff measure $\mathcal{H}_g(B)$ of B with respect to the distance induced on N by g. In addition, if g' is another Riemannian metric on N, then

$$\mathcal{H}_{g'}(B) = \int_B \frac{\mu(\{x \in T_pM : \phi_g(p,x) \leq 1\})}{\mu(\{x \in T_pM : \phi_{g'}(p,x) \leq 1\})}\, d\mathcal{H}_g(B)$$

where ϕ_g is the convex metric on the fiber bundle to M induced by g and μ is any translation invariant Radon measure on the tangent spaces.

The length $l_\phi(\gamma)$ of an absolutely continuous curve $\gamma : [0,1] \to N$ connecting two points $p, q \in N$, N a Riemannian manifold, is given by

$$l_\phi(\gamma) := \int_0^1 \phi(\gamma(t), \dot\gamma(t))\, dt,$$

and the distance between two points $p, q \in N$ is given by

$$d_\phi(p,q) = \inf l(\gamma), \tag{4.14}$$

among all absolutely continuous curves $\gamma : [0,1] \to N$ such that $\gamma(0) = p$ and $\gamma(1) = q$. The arc length parameter τ of the curve γ is given by $\tau(t) := \int_0^t \phi(\gamma(\sigma), \dot\gamma(\sigma))\, d\sigma$.

In the case of the Lorentzian manifold M, for a nonspacelike curve γ, $l(\gamma) := \int_0^1 \sqrt{-\dot{\gamma}_a(t)\dot{\gamma}^a(t)}\ dt$, and it is necessary to substitute the infimum with the supremum in (4.14). For instance, we can consider

$$d_g(p,q) = \sup \int_0^1 \sqrt{-\dot{\gamma}_a(t)\dot{\gamma}^a(t)}\ dt \tag{4.15}$$

where the supremum is taken among all nonspacelike curves connecting p and q. $\tau(t)$ is called proper time (ar affine parameter), and sometimes is denoted by $s(t)$.

Stationary points of the functional on the right hand side of (4.14) satisfy the geodesic equations (which is a way to introduce the Christoffel symbols) in the parameter t,

$$\frac{d^2\gamma^i}{dt^2} + \Gamma^i_{mn}(\gamma)\frac{d\gamma^m}{dt}\frac{d\gamma^n}{dt} - \frac{d\gamma^i}{dt}\frac{d\log(\phi(\gamma,\dot{\gamma}))}{dt} = 0. \tag{4.16}$$

The geodesics equivalently satisfy $\nabla_{t^a}t^a = 0$, and in the arc length parameter ($t^a = \frac{d\gamma}{ds}$) (4.16) becomes

$$\frac{d^2\gamma^i}{ds^2} + \Gamma^i_{mn}(\gamma)\frac{d\gamma^m}{ds}\frac{d\gamma^n}{ds} = 0. \tag{4.17}$$

4.1.1 The Riemann tensor

One of the possible ways to introduce the Riemann tensor is in terms of the failure of successive operations of differentiation to commute when applied to a dual vector field:

$$\nabla_a\nabla_b\omega_c - \nabla_b\nabla_a\omega_c = R_{abc}{}^d\omega_d. \tag{4.18}$$

Note that $(\nabla_a\nabla_b - \nabla_b\nabla_a)$ defines a linear map from dual vectors at a point p to tensors of type (0,3); i.e. its action is that of a tensor of type (1,3). In view of its antisymmetry (see (4.21)) we can think of the Riemann tensor also as a two-form, i.e., $R_{\mu\nu}$ is the two-form corresponding to $R_{ab\mu\nu}$.

From the definition it follows

$$R_{abc}{}^d = -R_{bac}{}^d \tag{4.19}$$

We also recall

$$R_{[abc]}{}^d = 0 \qquad \text{(first Bianchi's identity)} \tag{4.20}$$

the property

$$R_{abcd} = -R_{abdc} \tag{4.21}$$

and

$$\nabla_{[a} R_{bc]d}{}^{e} = 0 \qquad \text{(second Bianchi's identity).} \tag{4.22}$$

It follows from the above properties that

$$R_{adcd} = R_{cdab} \tag{4.23}$$

The expression of the Riemann tensor in a coordinate (holonomic) basis (which in general is not necessarily orthonormal) is given by

$$R_{\mu\nu\rho}{}^{\sigma} = \frac{\partial}{\partial x^{\nu}}\Gamma^{\sigma}{}_{\mu\rho} - \frac{\partial}{\partial x^{\mu}}\Gamma^{\sigma}{}_{\nu\rho} + \Gamma^{\alpha}{}_{\mu\rho}\Gamma^{\sigma}{}_{\alpha\nu} - \Gamma^{\alpha}{}_{\nu\rho}\Gamma^{\sigma}{}_{\alpha\mu}. \tag{4.24}$$

Therefore the Ricci tensor, defined as

$$R_{ac} = R_{abc}{}^{b}, \tag{4.25}$$

can be computed as

$$R_{\mu\rho} = \frac{\partial}{\partial x^{\nu}}\Gamma^{\nu}{}_{\mu\rho} - \frac{\partial}{\partial x^{\mu}}\Gamma^{\nu}{}_{\nu\rho} + \Gamma^{\alpha}{}_{\mu\rho}\Gamma^{\nu}{}_{\alpha\nu} - \Gamma^{\alpha}{}_{\nu\rho}\Gamma^{\nu}{}_{\alpha\mu}. \tag{4.26}$$

Recall that the scalar curvature R is given by

$$R = R_{a}{}^{a} = g^{ab}R_{ab}, \tag{4.27}$$

By equation 4.23, R_{ab} satisfies the symmetry property

$$R_{ac} = R_{ca} \tag{4.28}$$

The tensor

$$G_{ab} := R_{ab} - \frac{1}{2}Rg_{ab} \tag{4.29}$$

is called the Einstein's tensor. Such a tensor satisfies a conservation law.

Lemma 4.1.5. *We have*

$$\nabla_{a}G_{ab} = 0. \tag{4.30}$$

Proof. Contraction of the second Bianchi's identity (4.22) leads to

$$\nabla_a R_{bcd}{}^{a} + \nabla_b R_{cd} - \nabla_c R_{bd} = 0 \tag{4.31}$$

Rising the index d with the metric and contracting over b and d, we obtain

$$\nabla_a R_c{}^{a} + \nabla_b R_c{}^{b} - \nabla_c R = 0 \tag{4.32}$$

□

Remark 4.1.6. We remark that equation (4.29) is a geometric property, and does not depend on the validity on any type of partial differential equations involving fields and the metric tensor.

We finally recall that a space-time metric is called of constant curvature if $R_{abcd} = \frac{1}{12}R(g_{ac}g_{bd} - g_{ad}g_{bc})$, equivalently $R_{ab} = \frac{1}{4}Rg_{ab}$. It follows that R is constant. Note that $G_{ab} = R_{ab} - \frac{1}{2}Rg_{ab} = -\frac{1}{4}Rg_{ab}$, so that we can think that g solves Einstein equations in vacuo with $\Lambda = \frac{1}{4}R$.

Remark 4.1.7. Another way of introducing the Riemann tensor is to compute the expression of the second variation of arc length.

4.1.2 Connection one forms

Another way, beside (4.24), to compute the Riemann tensor is to use the tetrad method, namely using a noncoordinate *orthonormal* basis (also called nonholonomic basis) of smooth vector fields $(e_\mu)^a$, where orthonormality means $(e_\mu)^a(e_\nu)_a = \eta_{\mu\nu} := \mathrm{diag}(-1,1,1,1)$. One introduces a sort of analog of the Christoffel symbols (see (4.10)), called connection one-forms, $\omega_{a\mu\nu}$ (i.e., for any μ, ν, $\omega_{a\mu\nu}$ is a one-form), defined as

$$\omega_{a\mu\nu} = (e_\mu)^b \nabla_a (e_\nu)_b. \tag{4.33}$$

The components

$$\omega_{\lambda\mu\nu} = (e_\lambda)^a (e_\mu)^b \nabla_a (e_\nu)_b$$

are called Ricci rotation coefficients. The compatibility condition (4.5) between the metric and the derivative operator here is related to the ansisymmetry of Ricci rotation coefficients, i.e.,

$$\omega_{a\mu\nu} = -\omega_{a\nu\mu},$$

(see [30, pag. 50] for explanations) while the torsion free condition (4.7) is related to the commutation relation

$$\omega_{\mu\sigma\nu} - \omega_{\nu\sigma\mu} = (e_\sigma)_a [e_\mu, e_\nu]^a.$$

In addition it is possible to show (see [30, pag. 51]) that (note the operator ∂_a)

$$\partial_{[a}(e_\sigma)_{b]} = \eta^{\mu\nu}(e_\mu)_{[a}\omega_{b]\sigma\nu} \tag{4.34}$$

which in differential forms notation becomes

$$d\mathbf{e}_\sigma = \mathbf{e}_\mu \wedge \omega_\sigma{}^\mu. \tag{4.35}$$

Finally,

$$R_{\rho\sigma\mu\nu} = (e_\rho)^a (e_\sigma)^b \{\nabla_a \omega_{b\mu\nu} - \nabla_b \omega_{a\mu\nu} - \eta^{\alpha\beta}[\omega_{a\beta\mu}\omega_{b\alpha\nu} - \omega_{b\beta\mu}\omega_{a\alpha\nu}]\} \tag{4.36}$$

which in differential forms notation becomes

$$\mathbf{R}_\mu{}^\nu = d\omega_\mu{}^\nu + \omega_\mu{}^\alpha \wedge \omega_\alpha{}^\nu \tag{4.37}$$

(4.35) and (4.37) are called the structure equations.

Note the following advantage: the Ricci tensor can be computed via

$$R_{\rho\mu} = \eta^{\sigma\nu} R_{\rho\sigma\mu\nu}. \tag{4.38}$$

4.1.3 Some examples

It is often useful to think of immersed manifolds instead of abstract manifolds. In this respect we recall the following results.

Remark 4.1.8. If B denotes the second fundamental form of the immersed smooth Riemann hypersurface $N \subseteq \mathbb{R}^n$, then (see for instance [15, pag. 112]) we have the Gauss equations

$$R_{\alpha\beta\gamma\delta} = B_{\alpha\gamma}B_{\beta\delta} - B_{\alpha\delta}B_{\beta\gamma}, \tag{4.39}$$

which relate the intrinsic and the extrinsic curvatures. In this respect, note that in spite of the fact that for a manifold immersed in $\mathbb{R}^n$ the second fundamental form can be written in terms of the second derivatives of the immersion, the Riemann tensor involve the second derivatives of the metric tensor g (hence, were the manifold immersed, the third derivatives of the immersion).

Remark 4.1.9. If $N \subset M$ is a hypersurface, we also recall the equations of Codazzi-Mainardi (or Gauss-Codazzi):

$$\begin{aligned} {}^{(3)}R_{abc}{}^{d} &= h_{a}{}^{f} h_{b}{}^{g} h_{c}{}^{k} h^{d}{}_{j} R_{fgk}{}^{j} - B_{ac} B_{b}{}^{d} + B_{bc} B_{a}{}^{d}, \\ D_a B^{a}{}_{b} - D_b B^{a}{}_{a} &= R_{cd} n^{d} h_{c}{}^{b}, \end{aligned} \tag{4.40}$$

where h_{ab} is the induced metric on N, ${}^{(3)}R_{abcd}$ is the Riemann tensor of N, n^a is a unit normal vector field to N, B_{ab} is the second fundamental form of N, and D_a is the derivative operator on N induced by h.

On the basis of Gauss's equations we have the following examples.

Example 4.1.10. Let us consider the n-sphere of radius R embedded in $\mathbb{R}^{n+1}$ (with the induced metric). Then (see also [20, pag. 274])

$$R_{ijkl} = (g_{ik} g_{jl} - g_{il} g_{jk})/R^2,$$

and

$$R_{jl} = (n-1) g_{jl}/R^2, \qquad R = n(n-1)/R^2.$$

Example 4.1.11. Let M be a three-dimensional Riemannian manifold. Define $H_{ij} = 2R_{(i+1)(i+2)(j+1)(j+2)}$ (sum modulo 3). The operator H describes the Riemann operator. Assume that there is a basis for which both g_{ij} and the curvature operator are in diagonal form. Then

$$H_{ij} = \begin{pmatrix} \lambda & 0 & 0 \\ 0 & \mu & 0 \\ 0 & 0 & \nu \end{pmatrix}$$

where λ, μ, ν are twice the sectional curvatures, and

$$R_{ij} = \frac{1}{2} \begin{pmatrix} \mu + \nu & 0 & 0 \\ 0 & \lambda + \nu & 0 \\ 0 & 0 & \lambda + \mu \end{pmatrix} \qquad R = \lambda + \mu + \nu.$$

Example 4.1.12. Let M be a three-dimensional embedded manifold in $\mathbb{R}^4$, and let α, β, γ be the principal curvatures of M at a point $p \in M$. Define $H_{ij} = 2R_{(i+1)(i+2)(j+1)(j+2)}$ (sum modulo 3). Assume that there is a basis for which both g_{ij} and the second fundamental form are in diagonal form. Then

$$H_{ij} = \begin{pmatrix} 2\alpha\beta & 0 & 0 \\ 0 & 2\alpha\gamma & 0 \\ 0 & 0 & 2\beta\gamma \end{pmatrix}$$

and

$$R_{ij} = \frac{1}{2} \begin{pmatrix} \alpha(\beta+\gamma) & 0 & 0 \\ 0 & \beta(\alpha+\gamma) & 0 \\ 0 & 0 & \gamma(\alpha+\beta) \end{pmatrix} \qquad R = 2(\alpha\beta + \beta\gamma + \alpha\gamma)$$

Example 4.1.13. In the particular case of the three-sphere in $\mathbb{R}^4$ we have $H_{ij} = 2\mathrm{Id}$, $R_{ij} = 2\mathrm{Id}$. In the case of the cylinder $S^2 \times \mathbb{R}$,

$$H_{ij} = \begin{pmatrix} 2 & 0 & 0 \\ 0 & 0 & 0 \\ 0 & 0 & 0 \end{pmatrix} \qquad R_{ij} = \begin{pmatrix} 1 & 0 & 0 \\ 0 & 1 & 0 \\ 0 & 0 & 0 \end{pmatrix}$$

4.2 Derivation of Einstein's equations

Let us consider the functional (sometimes called Hilbert action)

$$S(g, \Omega) = \int_\Omega R d\mu_g \tag{4.41}$$

defined on smooth Lorentzian metrics g on an open subset Ω of M. The functional $S(\cdot, \Omega)$ has not good coerciveness properties (namely, is not bounded, see for instance [1]) which would guarantee the existence of minimizers in suitable spaces. However, we can look for stationary points of S. We now list two lemmas which can be used to prove Theorem 4.2.3.

Lemma 4.2.1. *Let $g(s)$ be a one-parameter family of metrics, and set $\mathcal{G}(s) = \mathrm{det} g_{ab}(s)$. Then $\frac{d\mathcal{G}}{ds} = \mathcal{G} g^{ab} \frac{\partial g_{ab}}{\partial s}$.*

Lemma 4.2.2. *Let $g(s)$ be a one-parameter family of metrics and set $v_{ij} = \frac{\partial}{\partial s} g_{ij}$. Then*

$$\frac{\partial}{\partial s} \Gamma^k_{ij} = \frac{1}{2} g^{kl} (\nabla_i v_{jl} + \nabla_j v_{il} - \nabla_l v_{ij}) \tag{4.42}$$

Theorem 4.2.3. *Let $\psi : \mathbb{R} \times M \to M$ be a smooth map, and set $\psi_\lambda(x) := \psi(\lambda, x)$. Given a metric tensor g, define $g_\lambda := g \circ \psi_\lambda$. Assume that $\psi_0 = \mathrm{id}$ and that $\psi_\lambda = \mathrm{id}$ in $M \setminus \Omega$. Then*

$$\frac{d}{d\lambda} S(g_\lambda)_{|\lambda=0} = \int_M (R_{ab} - \frac{1}{2} R g_{ab}) X^{ab} d\mu_g,$$

where $X^{ab} := \frac{\partial}{\partial \lambda} g_{\lambda}^{ab}{}_{\lambda=0}$.

Imposing stationarity of the action S with respect to all variations ψ_λ we obtain the vacuum Einstein's equations

$$G_{ab} := R_{ab} - \frac{1}{2} R g_{ab} = 0. \tag{4.43}$$

Remark 4.2.4. Let $\Lambda \in \mathbb{R}$; if we consider, instead of S, the functional

$$\int_\Omega R d\mu_g + \Lambda \int_\Omega d\mu_g \tag{4.44}$$

imposing stationarity as above yields the modified equations

$$R_{ab} - \frac{1}{2} R g_{ab} = \Lambda g_{ab}. \tag{4.45}$$

Remark 4.2.5. Einstein's equations are of second order in g_{ab} and not of fourth order, despite the fact that R contains also second derivatives of g_{ab}.

The vacuum Einstein's equations are a system of nonlinear partial differential equations. The initial data could be, for instance, the metric g_0 on a time-slice hypersurface Σ_0 together with the second fundamental form of Σ_0. The unknown is g_{ab} (see the initial discussion).

Remark 4.2.6. Taking the trace of vacuum Einstein's equations and recalling that the trace of g_{ab} equals 2 gives $R = 0$. Therefore if (4.43) are satisfied then

$$R_{ab} = 0. \tag{4.46}$$

Note carefully that this does not imply flatness of space, which is obtained by imposing that the whole Riemann tensor vanishes.

Remark 4.2.7. Other variations are possible concerning the action functional. For instance, the Palatini method consists in looking at the action as a functional of g and of the connection coefficients C^c_{ab} separately, and to perform variations also with respect to C^c_{ab}. See [30, Appendix E].

Remark 4.2.8. If in Theorem 4.2.3 we do not assume that ψ_λ is the identity on $M \setminus \Omega$, a boundary contribution appears in the computation of the first variation of the action.

We can add to the functional (4.44) a term depending on some field, and this is a way also to define the momentum-energy tensor, see [19]. More precisely, denote by L a Lagrangian density, $L = L(\Psi, \nabla\Psi)$, where Ψ is a (scalar or tensor) field Ψ, and consider the action

$$L_{\text{field}}(\Psi; \Omega) := \int_\Omega L(\Psi, \nabla\Psi)\ d\mu_g. \tag{4.47}$$

Definition 4.2.9. Assume that S_{field} is invariant under diffeomorphisms of M. We say that the symmetric tensor T_{ab} is the energy-momentum tensor (or the stress-energy-momentum tensor) of the system if

$$\frac{d}{d\lambda} S_{\text{field}}(\lambda)_{|\lambda=0} = \int_\Omega T_{ab} X^{ab}\ \mu_g, \tag{4.48}$$

where $S_{\text{field}}(\lambda)$ is the functional S_{field} considered as a function of $g(\lambda)$.

Definition 4.2.10. The fields equations are the equations for Ψ obtained by imposing stationarity of S_{field} in the sense of variations of Ψ, see [19, (3.4)].

Remark 4.2.11.

(i) Note that $T_{ab} = 0$ for the vacuum Einstein's equations.

(ii) It is possible to prove (see for instance [19]) that if Ψ solves the field equations then

$$\nabla_a T_{ab} = 0. \tag{4.49}$$

Remark 4.2.12. We will not discuss the issue of positivity properties of the energy-momentum tensor.

Example 4.2.13. We give the canonical example of a scalar field. Take

$$L_{\text{field}}(\psi, \nabla\psi) := -\nabla_a\psi\nabla_b\psi g^{ab} - \frac{m^2}{h^2}\psi^2, \tag{4.50}$$

where $m, h \in (0, +\infty)$. Then the field equations read as

$$\nabla^a\nabla_a\psi - \frac{m^2}{h^2}\psi = 0 \tag{4.51}$$

(relativistic Klein-Gordon equation) and the energy momentum tensor is given by

$$T_{ab} = \nabla_a\psi\nabla_b\psi - \frac{1}{2}g_{ab}(\nabla_c\psi\nabla^c\psi + \frac{m^2}{h^2}\psi^2). \tag{4.52}$$

Before passing to the next example, we briefly recall the relativistic form of Maxwell's equations [31]. Maxwell's equations classically read as

$$\begin{cases} \mathrm{div}E = 4\pi\rho, \\ \mathrm{rot}B = \dfrac{\partial E}{\partial t} + J, \\ \mathrm{div}B = 0, \\ \mathrm{rotE} = -\dfrac{\partial B}{\partial t}. \end{cases} \tag{4.53}$$

Let us introduce the tensor

$$(F^{\mu\nu}) = \begin{pmatrix} 0 & E_1 & E_2 & E_3 \\ -E_1 & 0 & B_3 & -B_2 \\ -E_2 & -B_3 & 0 & B_1 \\ -E_3 & B_2 & -B_1 & 0 \end{pmatrix} \tag{4.54}$$

Then the first and the second equations in (4.53) can be written (j^μ is the current 4-vector $j^\mu = (\rho, J)$) as

$$\nabla_\alpha F^{\alpha\beta} = -4\pi j^\beta. \tag{4.55}$$

while the third and the fourth equations in (4.53) can be written as

$$\nabla_\lambda F_{\mu\nu} + \nabla_\mu F_{\nu\lambda} + \nabla_\nu F_{\lambda\mu} = 0. \tag{4.56}$$

The electromagnetic force on a charged particle is

$$f^\alpha = eF^\alpha_{\ \gamma} \frac{dx^\gamma}{d\tau}$$

and the time derivative $\frac{dp}{dt}$ of the energy-momentum 4-vector is equal to f, so that

$$\frac{dp}{dt} = e(E + v \times B).$$

Thanks to the Poincaré Lemma and to (4.56), we can introduce locally the electromagnetic potential A_μ (vector potential) such that

$$F_{\gamma\delta} = \frac{\partial A_\delta}{\partial x^\gamma} - \frac{\partial A_\gamma}{\partial x^\delta}. \tag{4.57}$$

Recalling that F is defined up to a gradient, A_γ can be defined in such a way that $\partial^\alpha A_\alpha = 0$, and we obtain

$$\Box A_\alpha = -J_\alpha.$$

We also briefly recall the formulation of electrodynamics with differential forms. Let F be the two form defined as

$$F = \frac{1}{2} F_{\mu\nu} dx^\mu \wedge dx^\nu.$$

Then (4.57) reads as $F = dA$, where A is the one form $A = A_\mu dx^\mu$. Equation (4.56) reads as

$$dF = 0.$$

The current J is a one form defined as

$$J = j_\mu dx^\mu.$$

Example 4.2.14. We give the canonical example of the (source-free) electromagnetic field. Take

$$L(A) := -\frac{1}{8\pi} F_{ab} F^{ab} = -\frac{1}{2\pi} \nabla_{[a} A_{b]} \nabla^{[a} A^{b]}, \tag{4.58}$$

where the electromagnetic tensor field $F = 2dA$ (d the exterior differential of the one-form A, i.e., $F_{ab} = 2\nabla_{[a}A_{b]}$). Then the field equations are

$$\nabla^a F_{ab} = 0, \tag{4.59}$$

and the energy-momentum tensor is given by

$$T_{ab} = \frac{1}{4\pi}(F_{ac}F^c_b - \frac{1}{4}g_{ab}F_{de}F^{de}). \tag{4.60}$$

We recall once more that equation (4.59) together with $dF = 0$ (i.e., $\nabla_{[c}F_{ab]} = 0$) are the Maxwell equations for the source-free electromagnetic field.

Example 4.2.15. A perfect fluid in special relativity is described by a stress-energy tensor of the form

$$T_{ab} = \rho u_a u_b + P(\eta_{ab} + u_a u_b)$$

where u^a is a unit timelike vector field representing the 4-velocity of the fluid, ρ is the mass energy density and P the pressure of the fluid.

In General Relativity, the expression of the stress energy momentum tensor may be the sum of the tensors illustrated in Example (4.2.13), (4.2.14), (4.2.15).

Remark 4.2.16. It is possible to expand the action S around a background metric, see for instance [21].

Remark 4.2.17. We recall the following result, which is (roughly) called Noether's theorem. If the action is invariant under a continuous group of transformations, then the solutions (i.e., solutions of the corresponding Euler-Lagrange equations) satisfy conservation laws determined by these invariances.

4.3 The linearized theory of gravity

By means of a *formal* (i.e., *non rigorous*) asymptotic expansion, in this section we show how Einstein's equations reduce to Newton's equations in the weak gravity regime and for small velocities. These two assumptions allow two different expansions, one is the linearization around the flat metric, the other is an expansion essentially in powers of $1/c$. The first one (weak-field approximation) treats the field (i.e., the metric) in a lower order approximation, but does not necessarily assume that the matter moves nonrelativistically (hence it is suitable for gravitational waves). The second one treats a system of slowly varying moving particles under the gravitational force (such as the solar system).

In this section we perform both the expansions at the same time to first order. We assume that g is static, namely that g admits a timelike Killing vector field K which is orthogonal to a family of spacelike surfaces (that may be regarded as surfaces of constant time and may be labelled by the parameter t). In particular, M admits a global inertial system of coordinates.

We recall that Einstein's equations are gauge invariant, i.e., they are invariant under coordinate transformations.

Let us assume that in a sufficiently large region we have

$$g_{ab} = \eta_{ab} + \gamma_{ab} + o(\gamma_{ab}), \qquad |\gamma_{ab}| << 1, \tag{4.61}$$

$\eta_{ab} = \mathrm{diag}(-1, 1, 1, 1)$ the Minkowski metric, and γ_{ab} the deviation from flatness (sometimes denoted also by h_{ab}). We do not assume that the derivatives of γ_{ab} are small. Note carefully that we are not performing an expansion in terms of powers of $\frac{1}{c}$ (in the present discussion we set $c = 1$).

We adopt the following notation: ∂_a is the derivative operator associated with η_{ab}; g^{ab} is, as usual, the inverse of g_{ab}. Note that

$$g^{ab} = \eta^{ab} - \gamma^{ab} + o(\gamma_{ab}). \tag{4.62}$$

We raise and lower tensor indices with η_{ab} and η^{ab} and *not* with g_{ab} and g^{ab}. We define

$$\overline{\gamma}_{ab} := \gamma_{ab} - \frac{1}{2}\eta_{ab}\gamma, \tag{4.63}$$

where

$$\gamma := \gamma_c{}^c = \eta^{ab}\gamma_{ab}. \tag{4.64}$$

Note that

$$\gamma_{ab} = \overline{\gamma}_{ab} - \frac{1}{2}\eta_{ab}\overline{\gamma}, \tag{4.65}$$

where $\overline{\gamma} := \eta^{ab}\overline{\gamma}_{ab}$.

Theorem 4.3.1. *We have*

$$\partial^b \overline{\gamma}_{ab} = 0 \tag{4.66}$$

and

$$\partial^c \partial_c \overline{\gamma}_{ab} = -16\pi T_{ab}, \tag{4.67}$$

where we recall that $\partial^c \partial_c$ *is (if we assume* M *to be* $\mathbb{R} \times \mathbb{R}^3$*) the usual d'Alembertian operator (also denoted by* $\Box$*).*

Proof. We want to substitute (4.61) into (4.2) and retain only the linear terms in γ_{ab} (linearized theory). Recalling that $\partial_a \eta = 0$ and (4.9), we find

$$\Gamma^c{}_{ab}(g) = \frac{1}{2}\eta^{cd}\{\partial_a \gamma_{bd} + \partial_b \gamma_{ad} - \partial_d \gamma_{ab}\} + o(\gamma_{ab}), \tag{4.68}$$

where we have neglected the terms $\gamma_{ab}\partial_c \gamma_{de}$. From (4.26) we can neglect the products between two Christoffel coefficients, hence

$$R_{ab}(g) = \partial_c \Gamma^c{}_{ab} + \partial_a \Gamma^c{}_{cb} + o(\gamma_{ab}). \tag{4.69}$$

Recall that $\partial_{(b}\gamma_{a)_c} = \frac{1}{2}(\partial_b \gamma_{ac} + \partial_a \gamma_{bc})$, so that $\partial^c \partial_{(b}\gamma_{a)_c} = \frac{1}{2}(\partial^c \partial_b \gamma_{ac} + \partial^c \partial_a \gamma_{bc})$. Observing that $\eta^{cd}\partial_c \partial_a \gamma_{bd} = \partial^d \partial_a \gamma_{bd}$, using (4.68) it follows

$$\partial_c \Gamma^c{}_{ab} = \partial^c \partial_{(b}\gamma_{a)_c} - \frac{1}{2}\eta^{cd}\partial_c \partial_d \gamma_{ab} = \partial^c \partial_{(b}\gamma_{a)_c} - \frac{1}{2}\partial^c \partial_c \gamma_{ab}. \tag{4.70}$$

Note now that

$$\partial_a \Gamma^c{}_{cb} = \frac{1}{2}\partial_a \partial_b \gamma. \tag{4.71}$$

Indeed using (4.68) and rearranging terms

$$\partial_a \Gamma^c{}_{cb}(g) = \frac{1}{2}\eta^{cd}\partial_a \partial_b \gamma_{cd} + \frac{1}{2}\eta^{cd}\{\partial_a \partial_c \gamma_{bd} - \partial_a \partial_d \gamma_{cb}\}. \tag{4.72}$$

Since $\gamma = \eta^{cd}\gamma_{cd}$ and $\partial_a \partial_c \gamma_{bd} = \partial_a \partial_d \gamma_{cb}$, (4.71) follows from (4.72).

From (4.69), (4.70) and (4.71) it follows

$$R_{ab}(g) = \partial^c \partial_{(b}\gamma_{a)_c} - \frac{1}{2}\partial^c \partial_c \gamma_{ab} - \frac{1}{2}\partial_a \partial_b \gamma + o(\gamma_{ab}). \tag{4.73}$$

We also observe that

$$R = \partial^c \partial^d \gamma_{cd} - \partial^c \partial_c \gamma + o(\gamma_{ab}). \tag{4.74}$$

Indeed, from (4.73) it follows

$$R = \eta^{ab}\partial^c\partial_{(b}\gamma_{a)_c} - \frac{1}{2}\eta^{ab}\partial^c\partial_c\gamma_{ab} - \eta^{ab}\frac{1}{2}\partial_a\partial_b\gamma + o(\gamma_{ab}). \tag{4.75}$$

Since $\partial^c\partial_c\gamma = \eta^{ab}\partial^c\partial_c\gamma_{ab}$, using (4.75) it follows that to prove (4.74) it is enough to show

$$\eta^{ab}\partial^c\partial_{(b}\gamma_{a)_c} + \frac{1}{2}\eta^{ab}\partial_a\partial_b\gamma = \partial^c\partial^d\gamma_{cd} - \frac{1}{2}\partial^c\partial_c\gamma. \tag{4.76}$$

Recalling the expression $\partial^c\partial_{(b}\gamma_{a)_c} = \frac{1}{2}(\partial^c\partial_b\gamma_{a_c}\partial^c\partial_a\gamma_{b_c})$ and observing that $\eta^{ab}\partial_a\partial_b\gamma = \partial^c\partial_c\gamma$, (4.76) reduces to $\frac{1}{2}\eta^{ab}\partial^c\partial_b\gamma_{ab} + \frac{1}{2}\eta^{ab}\partial^c\partial_a\gamma_{bc} = \partial^c\partial^d\gamma_{cd}$, which is an identity since $\eta^{ab} = \eta_{ab}$. Then (4.74) is proved. From (4.73) and (4.74) and recalling the definition (4.29) of the Einstein tensor G_{ab}, we deduce

$$G_{ab} = \partial^c\partial_{(b}\gamma_{a)_c} - \frac{1}{2}\partial^c\partial_c\gamma_{ab} - \frac{1}{2}\partial_a\partial_b\gamma - \frac{1}{2}\eta_{ab}(\partial^c\partial^d\gamma_{cd} - \partial^c\partial_c\gamma) + o(\gamma_{ab}). \tag{4.77}$$

In terms of (4.63), we obtain

$$G_{ab} = -\frac{1}{2}\partial^c\partial_c\overline{\gamma}_{ab} + \partial^c\partial_{(b}\overline{\gamma}_{a)_c} - \frac{1}{2}\eta_{ab}\partial^c\partial^d\overline{\gamma}_{cd} + o(\gamma_{ab}). \tag{4.78}$$

Therefore, the linearized Einstein equations read as

$$-\frac{1}{2}\partial^c\partial_c\overline{\gamma}_{ab} + \partial^c\partial_{(b}\overline{\gamma}_{a)_c} - \frac{1}{2}\eta_{ab}\partial^c\partial^d\overline{\gamma}_{cd} = 8\pi T_{ab} \tag{4.79}$$

Let us show how to obtain the Lorentz gauge (4.66), see also [21]. Note that

$$\partial^b\overline{\gamma}_{ab} = \partial^b\gamma_{ab} - \frac{1}{2}\eta_{ab}\partial^b\gamma = \partial^b\gamma_{ab} - \frac{1}{2}\partial_a\gamma. \tag{4.80}$$

In place of γ_{ab} let us consider $\gamma_{ab} + \partial_a\xi_b + \partial_b\xi_a$, for a suitable vector field to be selected later (see (4.82)). Then

$$\partial^b\overline{\gamma}_{ab} = \partial^b(\gamma_{ab} + \partial_a\xi_b + \partial_b\xi_a) - \frac{1}{2}\partial_a(\gamma + 2\partial^b\xi_b). \tag{4.81}$$

If we assume that ξ_a satisfies

$$\partial^b\partial_b\xi_a = -\partial^b\overline{\gamma}_{ab}, \tag{4.82}$$

using $\partial_a\partial_b = \partial_b\partial_a$ and (4.81), formula (4.66) follows. As explained in [30, pag. 75] (see also [22, Chapter 18]), the modification of γ_{ab} into $\gamma_{ab} + \partial_a\xi_b + \partial_b\xi_a$ does not affect, to first order, the result. Therefore,taking into account (4.66), we have that (4.79) takes the form (4.67). □

Remark 4.3.2. Without assuming $c = 1$ and $G = 1$, (4.67) reads as

$$\partial^c \partial_c \overline{\gamma}_{ab} = -\frac{16\pi G}{c^4} T_{ab}. \tag{4.83}$$

Remark 4.3.3. As a consequence of (4.66) and (4.67) it follows $\partial^a T_{ab} = 0$ (note the presence of the ordinary derivative).

Remark 4.3.4. For a more general expansion of a metric around *any* fixed metric we refer to [30] and [21].

4.3.1 The Newtonian limit

We assume in this section that in a suitable coordinate system

(i)
$$T_{ab} \simeq \rho t_a t_b, \qquad t_a = (\frac{\partial}{\partial x^0})^a. \tag{4.84}$$
We therefore neglect time-space components ("small" velocities) and space-space components ("small" stresses) of the energy momentum tensor.

(ii)
$$\frac{\partial}{\partial x^0} \overline{\gamma}_{ab} = 0. \tag{4.85}$$

(iii) if τ denotes the proper time then $\tau \simeq t$ (t the coordinate time), and $\frac{dx^\alpha}{d\tau} \simeq (1, 0, 0, 0)$.

From (4.67) and the above assumptions we deduce

$$\Delta \overline{\gamma}_{\mu\nu} = 0, \qquad (\mu, \nu) \in \{0, 1, 2, 3\}^2 \setminus \{(0, 0)\}, \tag{4.86}$$

$$\Delta \overline{\gamma}_{00} = -16\pi\rho. \tag{4.87}$$

We then get (using reasonable growth assumptions on $\overline{\gamma}_{\mu\nu}$ at infinity)

$$\overline{\gamma}_{\mu\nu} = 0, \qquad (\mu, \nu) \in \{0, 1, 2, 3\}^2 \setminus \{(0, 0)\}. \tag{4.88}$$

Set

$$\phi := -\frac{1}{4} \overline{\gamma}_{00},$$

in such a way that

$$\Delta\phi = 4\pi\rho. \tag{4.89}$$

Recalling (4.65) we also have

$$\gamma_{ab} = -4(t_a t_b + 2\eta_{ab})\phi. \tag{4.90}$$

The equation (4.17) then becomes

$$\frac{d^2x^\mu}{dt^2} = -\Gamma^\mu{}_{00}. \tag{4.91}$$

Neglecting the time derivative of ϕ, from (4.90) we get for $\mu = 1, 2, 3$,

$$\Gamma^\mu{}_{00} = -\frac{1}{2}\frac{\partial\gamma_{00}}{\partial x^\mu} = \frac{\partial\phi}{\partial x^\mu}. \tag{4.92}$$

Thus the motion of test bodies is governed by the equation

$$\frac{d^2x}{dt^2} = -\nabla\phi(x). \tag{4.93}$$

Equations (4.89) and (4.93) are the equations of Newtonian mechanics.

Remark 4.3.5. There is an equivalent way to end up with equations (4.89) and (4.93) starting from the geodesic equation, see for instance [31, pag. 77]. Let us consider a particle moving slowly in a weak stationary gravitational field. We consequently assume

(i) $\frac{dx}{d\tau}$ is negligible with respect to $\frac{dt}{d\tau}$ (slow motion);

(ii) all time derivatives of $g_{\mu\nu}$ vanish (stationary field);

(iii) the expansion (4.61) holds (weak field assumption).

Form (i) and (4.17) we get

$$\frac{d^2x^\mu}{d\tau^2} + \Gamma^\mu{}_{00}\left(\frac{dt}{d\tau}\right)^2 = 0. \tag{4.94}$$

From (ii) and (4.10) we have

$$\Gamma^\mu{}_{00} = \frac{1}{2}g^{\mu\sigma}\left\{\frac{\partial g_{0\sigma}}{\partial x^0} + \frac{\partial g_{0\sigma}}{\partial x^0} - \frac{\partial g_{00}}{\partial x^\sigma}\right\} = -\frac{1}{2}g^{\mu\sigma}\frac{\partial g_{00}}{\partial x^\sigma}. \tag{4.95}$$

Using (iii), from (4.95) we may write

$$\Gamma^{\mu}{}_{00} = -\frac{1}{2}\eta^{\mu\sigma}\frac{\partial\gamma_{00}}{\partial x^{\sigma}}. \tag{4.96}$$

Inserting (4.96) into (4.94) gives

$$\frac{d^2x}{d\tau^2} = \frac{1}{2}\left(\frac{dt}{d\tau}\right)^2 \nabla\gamma_{\ 00}, \tag{4.97}$$

and finally

$$\frac{d^2x}{dt^2} = \frac{1}{2}\nabla\gamma_{00}, \tag{4.98}$$

in accordance with (4.93) if we choose

$$\gamma_{00} = -2\phi \tag{4.99}$$

so that

$$g_{00} = -(1+2\phi). \tag{4.100}$$

4.3.2 Gravitational waves

Following [21], we briefly recall some facts on gravitational waves. Gravitational waves arise as solutions of a wave equation, using a first order expansion of the background metric g_{ab}. Indeed, we recall (see (4.83)) that, in a suitable reference frame, we have that the expansion of g_{ab} to first order in $|\gamma_{ab}|$ around the flat metric η_{ab} gives (in vacuum)

$$\Box\overline{\gamma}_{ab} = 0. \tag{4.101}$$

As explained in [21], it is possible to find a coordinate system (the so-called transverse traceless gauge) where the metric in (4.101) takes a particular simple form:

$$\overline{\gamma}_{ab} = \gamma_{ab},$$

and

$$\gamma^{0\mu} = 0, \qquad \gamma^{\lambda}{}_{\lambda} = 0, \qquad \partial^{\nu}\gamma_{\lambda\nu} = 0, \qquad \mu,\nu \in \{0,\ldots,3\}. \tag{4.102}$$

Essentially, the nonzero space-components (orthogonal to the direction $n = e_3$ of the wave) reduce to

$$\gamma_{ab}^{TT}(t,z) = \begin{pmatrix} h_+ & h_\times \\ h_\times & -h_+ \end{pmatrix}_{ab} \cos(\omega(t - z/c)) \tag{4.103}$$

a, b indices in the (x, y)-plane, $k = (\omega, \mathbf{k})$, $\mathbf{k}$ the wave vector, $\omega = c|\mathbf{k}|$. The expression of the corresponding metric can be found in [21, formula (1.36)], to which we also refer for what concerns a discussion on the physical meaning of the transverse traceless reference frame. In these notes we do not discuss the expansion of a metric around a given fixed (non necessarily flat) metric; we just recall [21] that this is an issue related to fluctuation problems, and that expansions around η_{ab} seems to be too restrictive. In addition, computations and various averaging procedures show that interactions between the various terms in the formal asymptotic expansion around a nonflat metric lead to a new phenomenon: the effect of gravitational waves on the background curvature, which can be identified with the presence of a new energy-momentum tensor (denoted by $t_{\mu\nu}$). Such an energy-momentum tensor can therefore be associated with gravitational waves.

Remark 4.3.6. Also in this case it appears that there could be some relations between the averaging procedures described in [21] concerning gravitational waves and the theory of homogenization.

4.4 Exact solutions

When one is faced with a differential equation, it is always important to find special solutions (for instance, solutions with suitable symmetries). We refer to [27] for informations on exact solutions to Einstein's equations. It is clear that the Minkowski metric is a trivial solution to vacuum Einstein equations, see [19, Section 5.1] for a complete description of such a metric.

4.4.1 The Robertson-Walker solution

Let $\mathbb{S}^3$ (resp. $\mathbb{H}^3$) be the three dimensional sphere (resp. the three dimensional hyperbolic space). We recall the classifications of three dimensional manifolds of constant curvature: $\mathbb{R}^3$ in case of zero curvature, $\mathbb{S}^3$ in case of positive curvature, $\mathbb{H}^3$ in case of negative curvature. We assume

(1) $M = \mathbb{R} \times \mathbb{R}^3$ (resp. $M = \mathbb{R} \times \mathbb{S}^3$, $M = \mathbb{R} \times \mathbb{H}^3$)

(2) $ds^2 = -d\tau^2 + a^2(\tau)(dx^2 + dy^2 + dz^2)$ (resp. $ds^2 = -d\tau^2 + a^2(\tau)(d\psi^2 + \sin^2\psi(d\theta^2 + \sin^2\theta d\phi^2))$, $ds^2 = -d\tau^2 + a^2(\tau)(d\psi^2 + \sinh^2\psi(d\theta^2 + \sin^2\theta d\phi^2))$).

(3) $T_{ab} = \rho u_a u_b + P(g_{ab} + u_a u_b)$.

ρ, P are assigned at time zero, as well as g_{ab} with its time derivative. We look for ρ, P and g_{ab} at subsequent times. A computation starting from (4.2) and (4.9) (see for instance [30, Section 5.2]) yields, under the further assumption $\Lambda = 0$,

$$\begin{cases} \dfrac{3\dot{a}^2}{a^2} = 8\pi\rho - \dfrac{3k}{a^2} \\ \\ \dfrac{3\ddot{a}}{a} = -4\pi(\rho + 3P), \end{cases} \tag{4.104}$$

where $k = 0$ (resp. $k = 1$, $k = -1$); additionally, from (4.49)

$$\dot{\rho} + 3(\rho + P)\frac{\dot{a}}{a} = 0. \tag{4.105}$$

Expanding (resp. contracting, static) universe means $\dot{a} > 0$ (resp. $\dot{a} < 0$, $\dot{a} = 0$). The function $H(\tau) := \frac{\dot{a}(\tau)}{a(\tau)}$ is called Hubble's "constant".

Remark 4.4.1. The space $\mathbb{R} \times \mathbb{S}^3$ with the Robertson-Walker metric

$$ds^2 = -d\tau^2 + a^2(\tau)(d\psi^2 + \sin^2\psi(d\theta^2 + \sin^2\theta d\phi^2)),$$

can be isometrically embedded in $(\mathbb{R}^5, \mathrm{diag}(+ + + + -))$ [27, pag. 584] via

$$\begin{cases} x_1(\tau, \psi, \theta, \phi) = a(\tau)\cos\psi, \\ x_2(\tau, \psi, \theta, \phi)a(\tau)\sin\psi\cos\theta, \\ x_3(\tau, \psi, \theta, \phi) + ix_4(\tau, \psi, \theta, \phi) = a(\tau)\sin\psi\sin\theta e^{i\phi}, \\ x_5(\tau, \psi, \theta, \phi) = \displaystyle\int \sqrt{1 + a'(\tau)^2}d\tau \end{cases}$$

Remark 4.4.2. It would be interesting to see whether it is possible to use homogenization theory in connection to the above described model. In this respect we recall that the one-dimensional wave equation can be obtained as the homogenized equation of a first order PDE with discontinuous coefficients.

4.4.2 The Schwarzschild solution

In this section we look for solutions to the Einstein's equations (4.46) in vacuum of the form

$$ds^2 = -f(r)dt^2 + h(r)dr^2 + r^2(d\theta^2 + \sin^2\theta d\phi^2), \tag{4.106}$$

(we normalize units in such a way that $c = 1$); see the discussion [30, p. 119-120] for the geometrical meaning of such a choice of the metric tensor. Here we only recall that M is foliated in three-dimensional spacelike surfaces Σ_t, each Σ_t being the image through an isometry of a given spacelike surface Σ, and t (the "time" component) labels Σ_t. We also recall that we assume the existence of a vector field ξ^a orthogonal to each Σ_t. Each Σ_t is, in turn, supposed to be foliated in two-spheres, which are parameterized through the parameter r; the meaning of r is $r^2 = \frac{A}{4\pi}$, where A is the area of the unit two-sphere. On the other hand, the induced metric on each r-two-sphere takes the form $r^2(d\theta^2 + \sin^2\theta d\phi^2)$, where (θ, ϕ) are spherical coordinates on Σ. In (4.106) the unknown $f(r)$ equals $-\xi_a\xi^a$. The coordinate system (t, r, θ, ϕ) is not well defined at the north and the south poles of the spheres, at those points where $\xi^a = 0$, at those points where $\nabla_a r = 0$, and more generally at those points where ξ^a and $\nabla_a r$ become collinear. See the discussion in [30, Chapter 6] for the interesting meaning of this kind of singularities, as well as for the possibility of continuing the solution beyond singularities.

Summarizing, we assume

(1) $M = \mathbb{R} \times (\mathbb{R}^3 \setminus \{0\})$;

(2) the metric is as in (4.106)

(3) $T_{ab} = 0$.

Theorem 4.4.3. *Under the above assumptions we have*

$$g = -\left(1 - \frac{2M}{r}\right) dt^2 + \left(1 - \frac{2M}{r}\right)^{-1} dr^2 + r^2(d\theta^2 + \sin^2\theta d\phi^2).$$

$r = 2M$ *is called the Schwarzschild radius.*

Proof. In order to write the Einstein's equations, we use the tetrad method. A orthonormal basis of dual vectors for the metric is

$$(e_0)_a = f^{1/2}(dt)_a, \quad (e_1)_a = h^{1/2}(dr)_a, \quad (e_2)_a = r(d\theta)_a, \quad (e_3)_a = r\sin\theta(d\phi)_a$$

Orthonormality can be sees as follows: $(e_0)_a(e_0)^a = g_{ab}(e_0)^b(e_0)^a = -ff^{-1} = -1$, the other computations being similar. We compute, recalling that ∂_a reduces to compute the differential,

$$\partial_a(e_0)_b = \partial_a(f^{1/2}(dt)_b) = \frac{1}{2}f^{-1/2}f'(dr)_a(dt)_b, \tag{4.107}$$

so that

$$\partial_{[a}(e_0)_{b]} = \frac{1}{2}f^{-1/2}f'(dr)_{[a}(dt)_{b]}. \tag{4.108}$$

Moreover, since $h = h(r)$,

$$\partial_{[a}(e_1)_{b]} = 0. \tag{4.109}$$

Also

$$\partial_{[a}(e_2)_{b]} = (dr)_{[a}(d\theta)_{b]},$$

and

$$\partial_{[a}(e_3)_{b]} = \sin\theta(dr)_{[a}(d\phi)_{b]} + r\cos\theta_{[a}(d\phi)_{b]}.$$

Step 1. Computations of the connection one forms. We have

$$\begin{aligned}
\omega_{b01} &= \frac{f'}{2(fh)^{1/2}}(dt)_b, \\
\omega_{b02} &= 0, \\
\omega_{b03} &= 0, \\
\omega_{b12} &= -(h)^{-1/2}(d\theta)_b, \\
\omega_{b13} &= -(h)^{-1/2}\sin\theta(d\phi)_b, \\
\omega_{b23} &= -\cos\theta(d\phi)_b.
\end{aligned} \tag{4.110}$$

Observe that $\partial_a(e_0)_b$ contains a dt-term, see (4.107), so that ω_{a00} contains a dt-term (see (4.33)) so that $(e_0)_a\omega_{b00} = 0$. From this observation, (4.34) and (4.108) we deduce

$$\begin{aligned}\partial_{[a}(e_0)_{b]} &= \frac{1}{2}f^{-1/2}f'(dr)_{[a}(dt)_{b]} = \sum_{\mu=\nu=0}^{3}\eta^{\mu\nu}(e_\mu)_{[a}\omega_{b]_{0\nu}} = \sum_{\mu=\nu=1}^{3}\eta^{\mu\nu}(e_\mu)_{[a}\omega_{b]_{0\nu}} \\ &= h^{1/2}(dr)_{[a}\omega_{b]_{01}} + r(d\theta)_{[a}\omega_{b]_{02}} + r\sin\theta(d\phi)_{[a}\omega_{b]_{03}}.\end{aligned} \tag{4.111}$$

Similarly, using (4.109), (4.34) and the observation that $\partial_a(e_1)_b$ contains a dr-term,

$$\begin{aligned}0 = \partial_{[a}(e_1)_{b]} &= \sum_{\mu=\nu=0}^{3}\eta^{\mu\nu}(e_\mu)_{[a}\omega_{b]_{1\nu}} = \sum_{\mu=\nu\in\{0,2,3\}}\eta^{\mu\nu}(e_\mu)_{[a}\omega_{b]_{1\nu}} \\ &= f^{1/2}(dt)_{[a}\omega_{b]_{10}} + r(d\theta)_{[a}\omega_{b]_{12}} + r\sin\theta(d\phi)_{[a}\omega_{b]_{13}}.\end{aligned} \tag{4.112}$$

Moreover

$$\begin{aligned}\partial_{[a}(e_2)_{b]} &= (dr)_{[a}(d\theta)_{b]} = \sum_{\mu=\nu=0}^{3}\eta^{\mu\nu}(e_\mu)_{[a}\omega_{b]_{2\nu}} = \sum_{\mu=\nu\in\{0,1,3\}}\eta^{\mu\nu}(e_\mu)_{[a}\omega_{b]_{2\nu}} \\ &= -f^{1/2}(dt)_{[a}\omega_{b]_{20}} + h^{1/2}(dr)_{[a}\omega_{b]_{21}} + r\sin\theta(d\phi)_{[a}\omega_{b]_{23}},\end{aligned} \tag{4.113}$$

$$\begin{aligned}\partial_{[a}(e_3)_{b]} &= \sin\theta(dr)_{[a}(d\phi)_{b]} + r\cos\theta(d\theta)_{[a}(d\phi)_{b]} = \sum_{\mu=\nu=0}^{3}\eta^{\mu\nu}(e_\mu)_{[a}\omega_{b]_{3\nu}} \\ &= \sum_{\mu=\nu\in\{0,1,2\}}\eta^{\mu\nu}(e_\mu)_{[a}\omega_{b]_{2\nu}} \\ &= -f^{1/2}(dt)_{[a}\omega_{b]_{30}} + h^{1/2}(dr)_{[a}\omega_{b]_{31}} + r(d\theta)_{[a}\omega_{b]_{32}}.\end{aligned} \tag{4.114}$$

Equations (4.111), (4.112), (4.113), (4.114) together with some further computations (see [30, pag. 122]) lead to (4.110).

Step 2. We have

$$\begin{aligned}
R_{ab01} &= \frac{d}{dr}\left(\frac{f'}{(fh)^{1/2}}\right)(dr)_{[a}(dt)_{b]} \\
R_{ab02} &= f^{-1/2}h^{-1}f'(d\theta)_{[a}(dt)_{b]}, \\
R_{ab03} &= f^{-1/2}h^{-1}f'\sin\theta(d\phi)_{[a}(dt)_{b]}, \\
R_{ab12} &= h^{-3/2}h'(dr)_{[a}(d\theta)_{b]}. \\
R_{ab13} &= \sin\theta h^{-3/2}h'(dr)_{[a}(d\phi)_{b]}. \\
R_{ab23} &= 2(1-h^{-1})\sin\theta(d\theta)_{[a}(d\phi)_{b]}
\end{aligned} \tag{4.115}$$

Since from (4.110) we have $\omega_{c\beta 0} = -\omega_{c0\beta} = 0$ unless $\beta = 1$, so that $\eta^{\alpha\beta}\omega_{c\beta 0}\omega_{d\alpha 1} = \eta^{\alpha 1}\omega_{c10}\omega_{d\alpha 1} = \eta^{11}\omega_{c10}\omega_{d11} = 0$, using (4.21) and (4.36) we deduce

$$\begin{aligned}
R_{ab01} = -R_{ab10} &= (e_a)^c(e_b)^d\{\partial_c\omega_{d01} - \partial_d\omega_{c01} - \eta^{\alpha\beta}[\omega_{c\beta 0}\omega_{d\alpha 1} - \omega_{d\beta 0}\omega_{c\alpha 1}]\} \\
&= (e_a)^c(e_b)^d\{\partial_c\omega_{d01} - \partial_d\omega_{c01}\}.
\end{aligned} \tag{4.116}$$

We now compute from (4.110)

$$\begin{aligned}
\partial_c\omega_{d01} &= \frac{d}{dr}\left(\frac{f'}{2(fh)^{1/2}}\right)(dr)_c(dt)_d, \\
\partial_d\omega_{c01} &= \frac{d}{dr}\left(\frac{f'}{2(fh)^{1/2}}\right)(dr)_d(dt)_c.
\end{aligned} \tag{4.117}$$

Therefore, from (4.116) and the relations $(e_a)^c(dr)_c = (dr)_a$, $(e_b)^d(dt)_d = (dt)_b$, we get

$$R_{ab01} = \frac{d}{dr}\left(\frac{f'}{(fh)^{1/2}}\right)(dr)_{[a}(dt)_{b]}$$

(note that the factor 1/2 is not explicitly written since it appears in the antisymmetrization of the indices $[\cdot]$). Moreover

$$\begin{aligned}
R_{ab02} = -R_{ab20} &= (e_a)^c(e_b)^d\{\partial_c\omega_{d02} - \partial_d\omega_{c02} - \eta^{\alpha\beta}[\omega_{c\beta 0}\omega_{d\alpha 2} - \omega_{d\beta 0}\omega_{c\alpha 2}]\} \\
&= -(e_a)^c(e_b)^d\{\eta^{\alpha\beta}[\omega_{c\beta 0}\omega_{d\alpha 2} - \omega_{d\beta 0}\omega_{c\alpha 2}]\} \\
&= -(e_a)^c(e_b)^d\{\eta^{11}[\omega_{c10}\omega_{d12} - \omega_{d10}\omega_{c12}]\} \\
&= -(e_a)^c(e_b)^d[\omega_{c10}\omega_{d12} - \omega_{d10}\omega_{c12}] = f^{-1/2}h^{-1}f'(d\theta)_{[a}(dt)_{b]}.
\end{aligned} \tag{4.118}$$

The remaining relations in (4.115) can be proved in a similar way. The proof of *step 2* is concluded.

We now recall (see (4.46)) the Einstein equations in vacuum can be equivalently written as

$$0 = R_{00} = R_{11} = R_{22} = R_{33}. \tag{4.119}$$

From (4.119), (4.115), (4.38) and $R_{\mu\nu} = R_{ab}(e_\mu)^a(e_\nu)^b$ we deduce

$$\begin{aligned} 0 = R_{00} &= R^1_{010} + R^2_{020} + R^3_{030} \\ &= \frac{1}{2}(fh)^{-1/2}\frac{d}{dr}[(fh)^{-1/2}f'] + (rfh)^{-1}f', \\ 0 = R_{11} &= -\frac{1}{2}(fh)^{-1/2}\frac{d}{dr}[(fh)^{-1/2}f'] + (rh^2)^{-1}f', \\ 0 = R_{22} = R_{33} &= -\frac{1}{2}(rfh)^{-1} + \frac{1}{2}(rh^2)^{-1}\text{‘}h' + r^{-2}(1-h^{-1}), \end{aligned} \tag{4.120}$$

and (fortunately)

$$0 = R_{\mu\nu}, \quad \mu \neq \nu.$$

Adding the first two equations in (4.120) yields

$$\frac{f'}{f} + \frac{h'}{h} = 0,$$

hence

$$f = Kh^{-1}, \tag{4.121}$$

$K \in \mathbb{R}$. Possibly rescaling time we can assume $K = 1$. The third equation in (4.120) then becomes

$$-f' + \frac{1-f}{r} = 0,$$

i.e., $\frac{d}{dr}(rf) = 1$, so that

$$f = 1 + \frac{C}{r}. \tag{4.122}$$

(4.121) and (4.122) solve completely the Einstein equation under the above mentioned hypotheses. We refer to [30] for the physical implications of this special solutions to Einstein's equations. The Schwarzschild metric is sometimes written as

$$g = -(1 - \frac{r_0}{r})dt^2 + (1 - \frac{r_0}{r})^{-1}dr^2 + r^2(d\theta^2 + \sin^2\theta d\phi^2),$$

□

4.4.3 Interior Schwarzschild solutions ($r \geq 2m(r)$)

We now recall what is the interior Schwarzschild solution: assume that we are in presence of a perfect fluid stress-energy tensor (for instance, inside a star) of the form

$$T_{ab} = \rho u_a u_b + P(g_{ab} + u_a u_b), \tag{4.123}$$

where $u^a = -f^{1/2}(dt)^a$. Recall that T_{ab} satisfies a conservation law. Assume that $P = \rho = 0$ outside the star, namely for $r \geq R$, for some $R > 0$. The idea is to find a solution of Einstein's equations for $r \leq R$, and then match (since $P = \rho = 0$ for $r > R$) such a solution with the previously obtained solution (in vacuum) for $r > R$, where we have set

$$M := 4\pi \int_0^R \rho(r) r^2 \, dr.$$

From (4.2) (with $\Lambda = 0$), (4.123), (4.106) and (4.27) we find

$$\begin{aligned} 8\pi T_{00} = 8\pi\rho &= R_{00} - \frac{1}{2}R\eta_{00} = R_{00} + \frac{1}{2}R \\ &= R_{00} + \frac{1}{2}(-R_{00} + R_{11} + R_{22} + R_{33}) = R_{00} + \frac{1}{2}(-R_{00} + R_{11} + 2R_{22}) \\ &= \frac{1}{2}(R_{00} + R_{11} + 2R_{22}) = (rh^2)^{-1}h' + r^{-2}(1 - h^{-1}), \end{aligned} \tag{4.124}$$

where the last equality follows from the expressions in (4.120). In a similar way (recall $\eta_{11} = \eta_{22} = 1$) we find

$$\begin{aligned} &8\pi T_{11} = 8\pi P = (rfh)^{-1}f' - r^{-2}(1 - h^{-1}), \\ &8\pi T_{22} = 8\pi P = \frac{1}{2}(fh)^{-1/2}\frac{d}{dr}((fh)^{-1/2}f') + \frac{1}{2}(rfh)^{-1}f' - \frac{1}{2}(rh^2)^{-1}h'. \end{aligned} \tag{4.125}$$

From (4.124) it follows,

$$h(r) = (1 - \frac{2m(r)}{r})^{-1}, \qquad m(r) := \int_0^r \rho(r')r'^2 dr', \tag{4.126}$$

valid for $r \geq 2m(r)$. From the first equality in (4.125) it is possible to prove [30, pag. 127] that

$$f = e^{2\phi}, \qquad \frac{d\phi}{dr} = \frac{m(r) + 4\pi R^3 P}{r(r - 2m(r))}. \tag{4.127}$$

Finally, the last equation in (4.125) gives a compatiblity condition for P (recall that the energy-momentum tensor satisfies a conservation law), i.e.,

$$\frac{dP}{dr} = -(P+\rho)\frac{m(r)+4\pi r^3 P}{r(r-2m(r))}. \tag{4.128}$$

Remark 4.4.4. The maximal analytic extension of the Schwarzschild solution was found via an embedding into a higher dimensional flat space [27, pag. 581].

4.5 Post-Newtonian approximation

As already mentioned in Section 4.3, the post-Newtonian approximation is concerned with a system of slowly moving particles bound together by gravitational forces. In this section we will closely follow [31, Chapter 9]; in particular $\eta = \operatorname{diag}(-1,1,1,1)$ (and in our units $c=1$). Let us denote by $\overline{M}$, $\overline{r}$, $\overline{v}$ the typical values of masses, separations and velocities of the particles. We are looking for a formal asymptotic expansion in terms of

$$\overline{v}^2 \simeq G\overline{M}/\overline{r}, \tag{4.129}$$

(or, if we restore c, in terms of $\overline{v}/c$). We will also expand the metric g around the flat metric η, as done in Section 4.3. However, the order of expansions will be more accurate. We shall see that the computations, even if formal, are rather involved; it is useful to note that they will lead to phenomena such as precessions of perihelia, in agreement (and even more precisely) with the prediction given by Schwarzschild solution (see Section 4.5.1 below).

The real validity and the domain of applicability of such formal expansions should be carefully discussed; we refer to [17] and to the references in [3]. In this section we denote by $i, j, k, \dots$ (latin) indices running from 1 to 3; greek indices $\mu, \nu, \lambda \dots$ run from 0 to 4.

Since the scale of distance is of order $O(\overline{r})$, we have that

$$\partial/\partial x^i \text{ is of order } 1/\overline{r}; \tag{4.130}$$

moreover, since the scale of times is of order $\overline{r}/\overline{v}$, we have that

$$\partial/\partial t \text{ is of order } \overline{v}/\overline{r}. \tag{4.131}$$

Step 1. We have

$$\begin{aligned}\frac{d^2x^i}{dt^2} = &-\left(\Gamma^i{}_{00} + 2\Gamma^i{}_{0j}\frac{dx^j}{dt} + \Gamma^i{}_{jk}\frac{dx^j}{dt}\frac{dx^k}{dt}\right) \\ &+\left(\Gamma^0_{00} + 2\Gamma^0{}_{0j}\frac{dx^j}{dt} + \Gamma^0{}_{jk}\frac{dx^j}{dt}\frac{dx^k}{dt}\right)\frac{dx^i}{dt}.\end{aligned} \tag{4.132}$$

Arguing as in Remark 4.3.5, we begin by expanding (in (4.17)) $\frac{d^2x^i}{dt^2}$, and it will be necessary to go to the order $\overline{v}^4/\overline{r}$ (instead that to the order $\overline{v}^2/\overline{r}$, as in Section 4.3). We have, using the rule $\frac{d}{dt} = \frac{d}{d\tau}\frac{d\tau}{dt}$, and for $i \in \{1, 2, 3\}$,

$$\begin{aligned}\frac{d^2x^i}{dt^2} &= \frac{d}{d\tau}\left(\frac{dx^i}{d\tau}\frac{d\tau}{dt}\right)\frac{d\tau}{dt} = \left(\frac{dt}{d\tau}\right)^{-1}\frac{d}{d\tau}\left(\frac{dx^i}{d\tau}\left(\frac{dt}{d\tau}\right)^{-1}\right) \\ &= \left(\frac{dt}{d\tau}\right)^{-2}\frac{d^2x^i}{d\tau^2} - \left(\frac{dt}{d\tau}\right)^{-3}\frac{d^2t}{d\tau^2}\frac{dx^i}{d\tau}.\end{aligned} \tag{4.133}$$

Using (4.17) we have

$$\begin{cases}\left(\frac{dt}{d\tau}\right)^{-2}\frac{d^2x^i}{d\tau^2} = -\left(\frac{dt}{d\tau}\right)^{-2}\Gamma^i{}_{\nu\lambda}\frac{dx^\nu}{d\tau}\frac{dx^\lambda}{d\tau} = -\Gamma^i{}_{\nu\lambda}\frac{dx^\nu}{dt}\frac{dx^\lambda}{dt}, \\ \\ \frac{d^2t}{d\tau^2} = \frac{d^2x^0}{d\tau^2} = -\Gamma^0{}_{\nu\lambda}\frac{dx^\nu}{d\tau}\frac{dx^\lambda}{d\tau} = -\Gamma^0{}_{\nu\lambda}\frac{dx^\nu}{dt}\frac{dx^\lambda}{dt}\left(\frac{dt}{d\tau}\right)^2.\end{cases} \tag{4.134}$$

Multipyling the second equality in (4.134) by $dx^i/d\tau$ implies

$$-\left(\frac{dt}{d\tau}\right)^{-3}\frac{d^2t}{d\tau^2}\frac{dx^i}{d\tau} = \Gamma^0{}_{\nu\lambda}\frac{dx^\nu}{dt}\frac{dx^\lambda}{dt}\frac{dx^i}{dt}. \tag{4.135}$$

Inserting the first equality of (4.134) and (4.135) in (4.133) we conclude

$$\frac{d^2x^i}{dt^2} = -\Gamma^i{}_{\nu\lambda}\frac{dx^\nu}{dt}\frac{dx^\lambda}{dt} + \Gamma^0{}_{\nu\lambda}\frac{dx^\nu}{dt}\frac{dx^\lambda}{dt}\frac{dx^i}{dt}. \tag{4.136}$$

Using $j, k \in \{1, 2, 3\}$, $t = x^0$ and the symmetry property of the Christoffel symbols, (4.136) can be rewritten separating the indices, and gives (4.132).

Remark 4.5.1. The arguments of Remark 4.3.5 were concerned with only the first addendum on the right hand side of (4.132), using also ${\Gamma^i}_{00} \simeq -\frac{1}{2}\frac{\partial g_{00}}{\partial x^i}$. Since from (4.100) we see that $g_{00}+1$ is of order $G\overline{M}/\overline{r}$, it follows that $\frac{\partial g_{00}}{\partial x^i}$ is of order $G\overline{M}/(\overline{r}^2)$ (hence, thanks to (4.129), of order $\overline{v}^2/\overline{r}$). In the following we will go beyond such an order of expansion, namely to the order $\overline{v}^4/\overline{r}$.

Thanks to Remark 4.5.1, looking at the expression in (4.132), and recalling that dx^j/dt is of order $\overline{v}$, we need

(i) ${\Gamma^i}_{00}$ to order $\overline{v}^4/\overline{r}$;

(ii) ${\Gamma^i}_{0j}$ to order $\overline{v}^3/\overline{r}$;

(iii) ${\Gamma^i}_{jk}$ to order $\overline{v}^2/\overline{r}$;

(iv) ${\Gamma^0}_{00}$ to order $\overline{v}^3/\overline{r}$;

(v) ${\Gamma^0}_{0j}$ to order $\overline{v}^2/\overline{r}$;

(iv) ${\Gamma^0}_{jk}$ to order $\overline{v}/\overline{r}$.

We expand locally the metric g around the flat metric η in powers of $\overline{v}^2$. Using the fact that the transformation $t \to -t$ does not change (resp. change sign to) g_{00} and g_{ij} (resp. g_{0i}), we write, neglecting higher order terms,

$$\begin{cases} g_{00} = -1 + \overset{2}{g}_{00} + \overset{4}{g}_{00} + \ldots, \\ g_{ij} = \delta_{ij} + \overset{2}{g}_{ij} + \overset{4}{g}_{ij} + \ldots, \\ g_{i0} = \overset{3}{g}_{i0} + \overset{5}{g}_{i0} + \ldots, \end{cases} \tag{4.137}$$

where the higher number n refers to the order in the corresponding power of $\overline{v}^n$ (compare (4.151) below for the conclusions).

Step 2. We have

$$\begin{cases} \overset{2}{R}_{00} = \frac{1}{2}\Delta \overset{2}{g}_{00} + \ldots, \\ \overset{4}{R}_{00} = \frac{1}{2}\Delta \overset{4}{g}_{00} - \frac{1}{2}\frac{\partial^2 \overset{2}{g}_{00}}{\partial t^2} - \frac{1}{2}\overset{2}{g}_{ij}\frac{\partial^2 \overset{2}{g}_{00}}{\partial x^i \partial x^j} + \frac{1}{2}(\Delta \overset{2}{g}_{00})^2 + \ldots, \\ \overset{3}{R}_{0i} = \frac{1}{2}\Delta \overset{3}{g}_{i0} + \ldots, \\ \overset{3}{R}_{ij} = \frac{1}{2}\Delta \overset{3}{g}_{ij} + \ldots. \end{cases} \tag{4.138}$$

From (4.137) we have

$$\begin{cases} g^{00} = -1 + g^{\overset{2}{00}} + g^{\overset{4}{00}} = -1 - \overset{2}{g}_{00} + \overset{4}{g}_{00} + \dots, \\ g^{ij} = \delta_{ij} + g^{\overset{2}{ij}} + g^{\overset{4}{ij}} = \delta_{ij} - \overset{2}{g}_{ij} + \overset{4}{g}_{ij} + \dots, \\ g^{i0} = g^{\overset{3}{i0}} + g^{\overset{5}{i0}} = \overset{3}{g}_{i0} + \overset{5}{g}_{i0} + \dots. \end{cases} \tag{4.139}$$

Using (4.10), (4.139), (4.140), it is possible to check that the required expansion of the connection coefficients are as follows: $\Gamma^{i}{}_{00}, \Gamma^{i}{}_{jk}, \Gamma^{0}{}_{0i}$ do not have odd exponents in powers of $\overline{v}$, while $\Gamma^{i}{}_{0j}, \Gamma^{0}{}_{00}, \Gamma^{0}{}_{ij}$ do not have even exponets in powers of $\overline{v}$, precisely

$$\begin{cases} \Gamma^{\mu}{}_{\nu\lambda} = \Gamma^{\mu}{}_{\overset{2}{\nu\lambda}} + \Gamma^{\mu}{}_{\overset{4}{\nu\lambda}} + \dots \qquad \text{for } \Gamma^{i}{}_{00}, \Gamma^{i}{}_{jk}, \Gamma^{0}{}_{0i}, \\ \\ \Gamma^{\mu}{}_{\nu\lambda} = \Gamma^{\mu}{}_{\overset{3}{\nu\lambda}} + \Gamma^{\mu}{}_{\overset{5}{\nu\lambda}} + \dots \qquad \text{for } \Gamma^{i}{}_{0j}, \Gamma^{0}{}_{00}, \Gamma^{0}{}_{ij}, \end{cases} \tag{4.140}$$

where the higher number n refers to the order in the corresponding power of $\overline{v}^n/\overline{r}$. Hence we observe that

$$\begin{aligned} \Gamma^{i}{}_{\overset{2}{00}} &= -\frac{1}{2}\frac{\partial \overset{2}{g}_{00}}{\partial x^i} \\ \Gamma^{i}{}_{\overset{4}{00}} &= -\frac{1}{2}\frac{\partial \overset{4}{g}_{00}}{\partial x^i} + \frac{\partial \overset{3}{g}_{00}}{\partial t} + \frac{1}{2}\overset{2}{g}_{ij}\frac{\partial \overset{2}{g}_{00}}{\partial x^j}, \\ \Gamma^{i}{}_{\overset{3}{0j}} &= -\frac{1}{2}\left(\frac{\partial \overset{3}{g}_{i0}}{\partial x^j} + \frac{\partial \overset{2}{g}_{ij}}{\partial t} - \frac{\partial \overset{3}{g}_{j0}}{\partial x^i}\right), \\ \Gamma^{i}{}_{\overset{2}{jk}} &= -\frac{1}{2}\left(\frac{\partial \overset{2}{g}_{ij}}{\partial x^k} + \frac{\partial \overset{2}{g}_{ik}}{\partial x^j} - \frac{\partial \overset{2}{g}_{jk}}{\partial x^i}\right), \\ \Gamma^{0}{}_{\overset{3}{00}} &= -\frac{1}{2}\frac{\partial \overset{2}{g}_{00}}{\partial t} \\ \Gamma^{0}{}_{\overset{2}{0i}} &= -\frac{1}{2}\frac{\partial \overset{2}{g}_{00}}{\partial x^i} \\ \Gamma^{0}{}_{\overset{1}{ij}} &= 0 \end{aligned} \tag{4.141}$$

Recalling (i), in view of (4.141) it follows that we need

(v) g_{ij} to order $\overline{v}^2$,

(vi) g_{i0} to order $\overline{v}^3$,

(vii) g_{00} to order $\overline{v}^4$.

Using (4.26), (4.141), it follows

$$\begin{cases} R_{00} = \overset{2}{R}_{00} + \overset{4}{R}_{00} + \ldots, \\ R_{i0} = \overset{3}{R}_{i0} + \overset{5}{R}_{i0} + \ldots, \\ R_{ij} = \overset{2}{R}_{ij} + \overset{4}{R}_{ij} + \ldots, \end{cases} \tag{4.142}$$

where the higher number n refers to the order in the corresponding power of $\overline{v}^n/\overline{r}^2$.

Using the above expansions and normal coordinates around a fixed point [31, pag. 216], it is possible to check that the Ricci tensor satisfies (4.138). This concludes *step 2*.

Expanding

$$\begin{cases} T^{00} = T^{0\overset{0}{0}} + T^{0\overset{2}{0}} + \ldots, \\ T^{i0} = T^{i\overset{1}{0}} + T^{i\overset{3}{0}} + \ldots, \\ T^{ij} = T^{i\overset{2}{j}} + T^{i\overset{4}{j}} + \ldots, \end{cases} \tag{4.143}$$

where the higher number n refers to the order in the corresponding power of $(\overline{M}/\overline{r}^3)\overline{v}^n$, using (4.1) one finally gets [31, pag. 218]

$$\begin{cases} \Delta \overset{2}{g}_{00} = -8\pi G \overset{0}{T}{}^{00} \\ \\ \Delta \overset{4}{g}_{00} = \dfrac{\partial^2 \overset{2}{g}_{00}}{\partial t^2} + \overset{2}{g}_{ij} \dfrac{\partial^2 \overset{2}{g}_{00}}{\partial x^i \partial x^j} - \left(\dfrac{\partial \overset{2}{g}_{00}}{\partial x^i} \right) \left(\dfrac{\partial \overset{2}{g}_{00}}{\partial x^i} \right) - 8\pi G [T^{0\overset{2}{0}} - 2\overset{2}{g}_{00} T^{0\overset{0}{0}} + T^{i\overset{2}{j}}], \\ \\ \Delta \overset{3}{g}_{i0} = 16\pi G T^{i\overset{1}{0}} \\ \\ \Delta \overset{2}{g}_{ij} = -8\pi G \delta_{ij} T^{0\overset{0}{0}}. \end{cases} \tag{4.144}$$

We deduce (see (4.100)) that

$$\begin{cases} \overset{2}{g}_{00} = -2\phi, \\ \overset{2}{g}_{ij} = -2\delta_{ij}\phi, \end{cases} \tag{4.145}$$

ϕ the solution of the Poisson equation

$$\Delta\phi = 4\pi G T^{0\overset{0}{0}}, \tag{4.146}$$

vanishing at infinity, and therefore

$$\phi(x,t) = -G\int_{\mathbb{R}^3} \frac{T^{00}(x',\overset{0}{t})}{|x-x'|}\,dx'. \tag{4.147}$$

In general, $T^{00}(x',\overset{0}{t})$ is not given, and must determined implicitely using an iterative procedure, as explained below and in [31, pag. 225]. Moreover

$$\overset{3}{g}_{i0} = \zeta_i, \tag{4.148}$$

$$\zeta_i(x,t) = -4G\int_{\mathbb{R}^3} \frac{T^{i0}(x',\overset{1}{t})}{|x-x'|}\,dx'. \tag{4.149}$$

Furthermore (see [31]) the second equality in (4.144) can be transformed into

$$\overset{4}{g}_{00} = -2\phi^2 - 2\psi,$$

where

$$\Delta\psi = \frac{\partial^2\phi}{\partial t^2} + 4\pi G(T^{0\overset{2}{0}} + T^{i\overset{2}{j}}),$$

hence

$$\psi(x,t) = -\int_{\mathbb{R}^3}\left[\frac{1}{4\pi|x-x'|}\frac{\partial^2\phi(x',t)}{\partial t^2} + GT^{00}(x',\overset{2}{t}) + GT^{ij}(x',\overset{2}{t})\right]\,dx'. \tag{4.150}$$

We conclude that

$$\begin{cases} g_{00} = -1 - 2\phi + (-2\phi^2 - 2\psi) + \dots \\ g_{ij} = \delta_{ij} - 2\delta_{ij}\phi + \dots, \\ g_{i0} = \zeta_i + \dots \end{cases} \tag{4.151}$$

where ϕ, ψ, ζ_i have the expression in (4.147), (4.149), (4.150) respectively, and, because of the use of normal coordinates,

$$4\frac{\partial\phi}{\partial t} + \mathrm{div}\zeta = 0.$$

Inserting the above expressions in (4.141) yields

$$\begin{aligned}
\Gamma^{i}{}^{2}_{00} &= \frac{\partial \phi}{\partial x^i}, \\
\Gamma^{i}{}^{4}_{00} &= \frac{\partial}{\partial x^i}\left(2\phi^2 + \psi\right) + \frac{\partial \zeta_i}{\partial t}, \\
\Gamma^{i}{}^{3}_{0j} &= \frac{1}{2}\left(\frac{\partial \zeta_i}{\partial x^j} - \frac{\partial \zeta_j}{\partial x^i}\right) - \delta_{ij}\frac{\partial \phi}{\partial t}, \\
\Gamma^{i}{}^{2}_{jk} &= -\delta_{ij}\frac{\partial \phi}{\partial x^k} - \delta_{ik}\frac{\partial \phi}{\partial x^j} + \delta_{jk}\frac{\partial \phi}{\partial x^i} \\
\Gamma^{0}{}^{3}_{00} &= \frac{\partial \phi}{\partial t}, \\
\Gamma^{0}{}^{2}_{0i} &= \frac{\partial \phi}{\partial x^i}.
\end{aligned} \tag{4.152}$$

Finally, the conservation law (4.49) reads (to the required order) [31, pag. 222]

$$\begin{aligned}
&\frac{\partial T^{0\overset{0}{0}}}{\partial t} + \frac{\partial T^{i\overset{1}{0}}}{\partial x^i} = 0, \qquad &&\text{(conservation of mass)} \\
&\frac{\partial T^{0\overset{1}{i}}}{\partial t} + \frac{\partial T^{i\overset{2}{j}}}{\partial x^j} = -\frac{\partial \phi}{\partial x^i} T^{0\overset{0}{0}} \qquad &&\text{(conservation of momentum)}
\end{aligned} \tag{4.153}$$

The following result is a consequence of the computations in (4.5).

Corollary 4.5.2. *The dynamics of a freely falling particle, to the order* $\overline{v}^4/\overline{r}$, *is governed by a Lagrangian*

$$L = \frac{1}{2}v^2 - \phi - \frac{1}{2}\phi^2 - \frac{3}{2}\phi v^2 + \frac{1}{8}(v^2)^2 - \psi + \zeta \cdot v,$$

i.e.,

$$\frac{d}{dt}\frac{\partial L}{\partial v^i} = \frac{\partial L}{\partial x^i}. \tag{4.154}$$

Proof. Inserting in (4.132) the expressions (4.152) implies

$$\begin{aligned}
\frac{dv}{dt} =& - \nabla(\phi + 2\phi^2 + \psi) - \frac{\partial \zeta}{\partial t} + v \times \mathrm{rot}\zeta \\
&+ 3v\frac{\partial \phi}{\partial t} + 4v(v \cdot \nabla)\phi - v^2 \nabla \phi,
\end{aligned} \tag{4.155}$$

which is equivalent to (4.154). □

Remark 4.5.3. The procedure to use the post-Newtonian approximation, for instance in the case of a system $\{x_n\}$ of particles, is the following. The first step consists in solving (if possible!) the Newton equations

$$\begin{aligned} \frac{dv_n}{dt} &= -\nabla\phi(x_n) \\ \Delta\phi &= 4\pi G T^{0\overset{0}{0}}, \end{aligned} \tag{4.156}$$

in the unknowns ϕ, x_n (at this level $T^{0\overset{0}{0}}$ is not yet known). The second step consists in using the first step and the expressions of $T^{0\overset{0}{0}}$, $T^{0\overset{2}{0}}$, $T^{i\overset{1}{0}}$, $T^{i\overset{2}{j}}$ for the particular problem at hand to solve for $T^{0\overset{0}{0}}$, $T^{0\overset{2}{0}}$, $T^{i\overset{1}{0}}$, $T^{i\overset{2}{j}}$; for instance, it may happen that $T^{0\overset{0}{0}}$ depends only on x_n, so that using the first step one can solve for $T^{0\overset{0}{0}}$, and so on. The third step consists in using the first two steps to solve (4.149) and (4.150) in the unknowns ζ and ψ. At this point one corrects the trajectories x_n using (4.155). The procedure then restarts and so on.

4.5.1 Agreement with the Schwarzschild solution

Let us consider a distribution of energy $T^{\mu\nu}$ which vanishes for $r := |x| > R$. Expanding

$$\frac{1}{|x-x'|} = \frac{1}{r} + \frac{x \cdot x'}{r^3} + \cdots$$

in (4.147), (4.149), (4.150) gives

$$\begin{cases} \phi = -\dfrac{G\overset{0}{M}}{r} - \dfrac{Gx \cdot \overset{0}{D}}{r^3} + \cdots \\[2em] \overset{0}{M} = \displaystyle\int_{\mathbb{R}^3} T^{0\overset{0}{0}}\, dx, \qquad \overset{0}{D} = \int_{\mathbb{R}^3} x T^{0\overset{0}{0}}\, dx, \end{cases} \tag{4.157}$$

$$\begin{cases} \zeta_i = -\dfrac{4G\overset{1}{P}_i}{r} - \dfrac{2Gx^j \overset{1}{J}_{ji}}{r^3} + \cdots \\[2em] \overset{1}{P}_i = \displaystyle\int_{\mathbb{R}^3} T^{i\overset{1}{0}}\, dx, \qquad \overset{1}{J}_{ij} = 2\int_{\mathbb{R}^3} x^i T^{j\overset{1}{0}}\, dx, \end{cases} \tag{4.158}$$

$$\begin{cases} \psi = -\dfrac{G\overset{2}{M}}{r} - \dfrac{Gx \cdot \overset{2}{D}}{r^3} + \cdots \\ \\ \overset{2}{M} = \displaystyle\int_{\mathbb{R}^3} \left(T^{0\overset{2}{0}} + T^{\overset{2}{ii}} \right) \, dx, \qquad \overset{2}{D} = \displaystyle\int_{\mathbb{R}^3} x \left(T^{0\overset{2}{0}} + T^{\overset{2}{ii}} + \dfrac{1}{4\pi G} \dfrac{\partial^2 \phi}{\partial t^2} \right) \, dx. \end{cases} \tag{4.159}$$

Replacing ϕ by $\phi + \psi$ (see [31, pag. 226]) it follows that

$$\begin{cases} \phi + \psi = -\dfrac{GM}{|x - D/M|} + \cdots , \\ \\ \qquad M := \overset{0}{M} + \overset{2}{M}, \qquad D = \overset{0}{D} + \overset{2}{D}. \end{cases} \tag{4.160}$$

Suppose

(i) the energy-momentum tensor does not depend on time.

Then [31, pag. 227] using (4.153) it follows

$$\overset{1}{P^i} = 0,$$

so that ζ in (4.158) becomes, out of the gravitating mass,

$$\begin{cases} \zeta = \dfrac{2G}{r^3}(x \times J) + \cdots \\ \\ \overset{1}{J}_k = \dfrac{1}{2} \displaystyle\int_{\mathbb{R}^3} \epsilon_{ijk} x^i T^{j\overset{1}{0}}. \end{cases} \tag{4.161}$$

If we suppose

(ii)

$$T^{\mu\nu}(x,t) = T^{\mu\nu}(|x|,t),$$

then $|x - x'|^{-1}$ can be replaced by its mean value $1/r$ on the two-sphere, and it turns out that

$$\begin{cases} \phi = -\dfrac{GM}{r}, \\ \zeta = -4G\dfrac{\overset{1}{P}}{r}, \\ \psi = -\dfrac{G\overset{2}{M}}{r}. \end{cases} \tag{4.162}$$

If we further assume

(iii) the sphere at rest

then $\overset{1}{P} = 0$, and we finally obtain

$$\begin{aligned} g_{00} &= -1 + \frac{2MG}{r} - \frac{2M^2G^2}{r^2}, \\ g_{i0} &= 0, \\ g_{ij} &= \delta_{ij} + 2\delta_{ij}\frac{MG}{r}, \end{aligned} \tag{4.163}$$

in agreement with the Schwarzschild solution.

Let us now consider the sphere at rest, but rotating with angular frequency $\omega(r)$. In this case, using (4.149), it is possible to prove that

$$\zeta(x) = \begin{cases} \dfrac{2G}{r^3}(x \times J) & \text{inside the sphere} \\ x \times \Omega & \text{outside the sphere,} \end{cases} \tag{4.164}$$

where

$$\Omega = \frac{16\pi G}{3}\int_0^\infty \omega(r')T^{0\overset{0}{0}}(r')r'\,dr',$$

compare also (4.161).

The above computations allow to compute the precessions of planetary orbits in the solar system, due to the presence of other planets, to the rotation of the sun and so on. Let us denote by M_s the mass of the sun. The main contribution to $\phi + \psi$ in (4.160) is due to the sun, and we consequently write

$$\phi + \psi = -\frac{GM_s}{r} + \epsilon(x,t), \tag{4.165}$$

so that (4.155) becomes

$$\frac{dv}{dt} = -\frac{GM_s x}{r} + \eta + \cdots, \tag{4.166}$$

where

$$\eta = -\nabla(\epsilon + 2\phi^2) - \frac{\partial\zeta}{\partial t} + v \times \mathrm{rot}\zeta + 3v\frac{\partial\phi}{\partial t} + 4v(v\cdot\nabla)\phi - v^2\nabla\phi. \tag{4.167}$$

Set

$$A := -M_s G\frac{x}{r} + (v \times h), \qquad h := x \times v. \tag{4.168}$$

From (4.166) (see [31, Section 9.5]) it turns out that the rate of precession of perihelia is caused by

$$\frac{dA}{dt} = \eta \times h + v \times (x \times \eta), \tag{4.169}$$

where η is essentially given by

$$\eta = -2\nabla\phi_s^2 + 4v(v \cdot \nabla)\phi_s - v^2\nabla\phi_s, \qquad \phi_s := -\frac{GM_s}{r} \quad (\text{and } \zeta_s = 0).$$

Acknowledgments

Farò i ringraziamenti in italiano perchè tanto quelli che li devono leggere sono tutti italiani.

Grazie a Giovanni D. per avermi sopportato per sei mesi nell' ufficio, per la fiducia, per i consigli e la pazienza, per i biscotti e il cioccolato, per avermi fatto nutrire il gatto, per le risate e i pranzi con Ivan.

Grazie a Giovanni B. per avermi proposto questa tesi, per avermi fatto avvicinare alla Relatività Generale senza spaventarmi troppo, per essere stato il miglior professore di questo triennio, per la fiducia nelle mie possibilità e per la passione per il lavoro.

Grazie a Simone per l'entusiasmo verso il lavoro, per gli aiuti al computer, per avermi fatto visitare l'acceleratore, per le spiegazioni di fisica e per tutte le volte che ha ricorretto la tesi.

Grazie ai miei genitori e a mia sorella per il supporto morale e per essersi sorbiti le spiegazioni su LARES fin troppe volte.

Grazie ai miei amici a Roma (alla Cupola!), a Alba e al mio ragazzo per avermi aiutato con latex, per avermi incoraggiata e per tutti gli aiuti offerti.

Bibliography

[1] M.T. Anderson *Extrema of curvature functionals on the space of metrics on* 3*-manifolds* Calc. Var. Partial Differential Equations **5**, 199-269 (1997).

[2] G.S. Asanov *Finsler Geometry, Relativity and Gauge Theories.* D. Reidel Publishing Company, Dordrecht, Holland 1985.

[3] L. Bariotti *Teorie scalar tensoriali e formalismo Post-Newtoniano.* Tesi di Laurea in Fisica, 1999/2000, Univ. di Torino

[4] Christodoulou . Lectures at ETH, Zurich, 2003.

[5] I.Ciufolini, E.Pavlis, F.Chieppa, E.Fernandes-Vieira, J.Perez-Mercader *Science*,(March 1998)

[6] NASA facts *Gravity Probe-B*,(Feb 2005)

[7] I.Ciufolini and E.C.Pavlis *Nature*,(Oct 2004)

[8] http://www.wintcrop.com/contents/prism/corner.html

[9] V.J.Slabinski *A numerical solution for LAGEOS thermal thrust: the rapid-spin case*, (1996)

[10] *Proposal to INFN*, (2004)

[11] G.Delle Monache *LARES satellite thermal design: Proposal for the limitation of the themal thrusts*

[12] *www.crtech.com*

[13] www.boedeker.com

[14] G.Delle Monache *Interfaces thermal contact resistance of the CCR LAGEOS-LARES assembly*

[15] K. Ecker *Regularity Theory for Mean Curvature Flow.* Birkhäuser, 2004.

[16] L.C. Evans, R.F. Gariepy, *Measure Theory and Fine Properties of Functions.* CRC Press, 1992.

[17] R. Geroch, L. Lindbolm *Is perturbation theory misleading in general relativity?* J. Math. Phys. **26**, 2581–2588, 1985.

[18] R.S. Hamilton, *Three manifolds with positive Ricci curvature* J. Differ. Geom. **17**, 255-306 (1982).

[19] S. Hawking, G.F.R. Ellis *The large scale structure of space-time.* Cambridge Univ. Press, 1973.

[20] L. Hörmander *Lectures on Nonlinear Hyperbolic equations.* Mathématiques & Applications 26, Spinger-Verlag, 1997.

[21] M. Maggiore *Gravitational Waves*, book in preparation.

[22] C.W. Misner, K.S. Thorne, J.A. Wheeler *Gravitation.* W.H. Freeman and Company, New York 1973.

[23] G. Perelman, http://www.arxiv/org, 3.math.DG/0307245

[24] G. Perelman, http://www.arxiv/org, 4.math.DG/0303109

[25] G. Perelman, http://www.arxiv/org, 5.math.DG/0211159

[26] P. Petersen, *Riemannian Geometry.* Springer-Verlag, Berlin 1998.

[27] H. Stephani, D. Kramer, M. Maccallum, C. Hoenselaers, E. Herlt *Exact Solutions of Einstein's Field Equations.* Cambridge Univ. Press, 2003.

[28] N. Straumann *General Relativity and Relativistic Astrophysics.* Springer-Verlag, 1991.

[29] W. Thirring *Classical Mathematical Physics. Dynamical Systems and Field Theory*. Springer, 1992.

[30] R.M. Wald *General Relativity*. The University of Chicago Press, Chicago, 1984.

[31] S. Weinberg *Gravitation and Cosmology: Principles and Applications of the General Theory of Relativity*. John Wiley & Sons, New York, 1972.